

Development of a Jumping Robot using Soft Pneumatic Actuators

Diploma Thesis
of

Daniel Enrique Rojas

At the Faculty of Informatics
Institute for Anthropomatics and Robotics (IAR)
High Performance Humanoid Technologies Lab (H²T)

and the

Hong Kong University of Science and Technology
Department of Mechanical and Aerospace Engineering

First reviewer: Prof. Dr.-Ing. habil. Georg Breithauer
Second reviewer: Prof. Dr.-Ing. Tamim Asfour
Advisors: Prof. Lilong Cai, Ph.D.
Prof. Dr.-Ing. Tamim Asfour
Mr. Feng Ni, M.Sc.

Duration: March 1, 2014 – August 30, 2014

I declare that I have developed and written the enclosed Diploma Thesis completely by myself, and have not used sources or means without declaration in the text.
Karlsruhe, August 30, 2014

Abstract

Soft robotics is an emerging field of novel mechanical designs that create compliant and tolerant structures out of flexible materials, attempting to reduce the complexity of both their hardware and software to compensate for or eliminate some of the constraints set by traditional 'hard' robots such as low adaptability or high complexity. At the same time, jumping is a very interesting method of locomotion, with the animal kingdom providing myriads of very diverse and successful examples. The study of jumping or hopping robots could prove extremely useful in situations such as rough terrain, high obstacles and other complex environments.

The goal of this project is to develop a mobile robot platform capable of jumping locomotion using soft, silicone elastomer based pneumatic actuators as legs that accelerate the platform upwards by expanding rapidly upon applying internal air pressure. The robot is able to control the direction of the jump by altering the timing patterns in which the individual legs are activated. It is equipped with on-board electronics that allow controlling and logging the jumping performance.

After providing an overview on the existing research on jumping robots, fluidic actuation and soft robotics, the actuators themselves are designed, tested and their static and dynamic behavior characterized. Then, the robot platform is developed, including the structural design, the pneumatic system, the electronics and the control software. A protocol is implemented to allow wireless communication between the robot and a PC. A tetherless version with on-board electrical and pneumatic supply is also presented. Afterwards, several experiments are conducted to evaluate and improve the jumping performance with regards to height, distance and direction, and the insights gained are compiled to gauge the usefulness of such robotic systems. Furthermore, challenges encountered and pointers for further research are outlined.

Extended Abstract (Deutsch)

Soft Robotics ist eine Branche der Robotik, die sich mit flexiblen und nachgiebigen Strukturen und Materialien befasst, um neuartige Geräte zu entwickeln. Im Gegensatz zur traditionellen, 'harten' Robotik wird hierbei auf starre Elemente und fest definierte Gelenke verzichtet, und stattdessen auf frei verformbare, weiche Kontinua gesetzt. Oftmals kommt pneumatischer Druck als Energiequelle zum Einsatz, der je nach Morphologie des Aktors vielfältige Bewegungsarten ermöglicht. Vorteile von Soft Robotics sind unter anderem eine geringere Komplexität, hohe Robustheit, hohe Anpassungsfähigkeit an unbekannte Bedingungen und die sichere Interaktion mit Menschen.

Auf dem Gebiet der Fortbewegungstechniken ist Springen mittlerweile von vielen Forschergruppen untersucht worden. Insbesondere ungleichmäßige Untergründe und hohe Hindernisse können von Robotern durch Sprünge überwunden werden. Oftmals sind hierbei die besten Vorbilder in der Natur zu finden, wo sich vielfältige Sprungtechniken entwickelt haben.

Bisher gibt es noch wenig Forschung, die sich mit der Verschmelzung beider Gebiete beschäftigt. Die Zielsetzung dieser Arbeit ist es, eine mobile Roboterplattform zu entwickeln, die in der Lage ist, sich mithilfe von weichen Elastomer-basierten Pneumatikaktoren sprungartig fortzubewegen. Hierbei liefert die schnelle Ausdehnung der Aktoren unter Druckluftzugabe die Energie für den Sprung. Der Roboter sollte in der Lage sein, die Höhe und die Richtung des Sprungs zu steuern, indem die einzelnen Füße zeitlich versetzt feuern. Die Bordelektronik übernimmt hierbei sowohl die Steuerung des pneumatischen Systems als auch die Aufzeichnung der Sensordaten während des Sprungs, um weitere Analysen zu ermöglichen.

Nach einem kurzen Überblick über den Stand der Forschung auf den Gebieten der springenden Roboter und Soft Robotics, wird zunächst der zu verwendende Pneumatikaktor vorgestellt. Es handelt sich hierbei um eine Eigenentwicklung: Der flache, kreisförmige Aktor wird in zwei Hälften gegossen und anschließend so zusammengefügt, dass sich im Inneren eine Aussparung ergibt. Wird anschließend Luftdruck über die Zuleitung eingeführt, dehnt sich der Aktor entlang seiner Achse aus und übt eine Kraft aus. Es wird sowohl das statische Verhalten des Aktors unter verschiedenen Innendrücken und Ausdehnungszuständen (über einen Kraftmessdosen-Aufbau), als auch das dynamische Verhalten unter einem kurzen, starken Druckimpuls und unterschiedlichen Lasten mithilfe einer Hochgeschwindigkeitskamera untersucht, um seine Leistung im angestrebten Anwendungsfäll zu ermitteln. Neben einem einfachen Aktor wird auch eine Aneinanderreihung von vier baugleichen Segmenten untersucht, wegen der Schwierigkeiten bei der Herstellung und des unberechenbaren Verhaltens im Test ohne Verbesserung der Sprungleistung allerdings wieder verworfen.

Anschließend wird die Roboterplattform in CAD modelliert und gefertigt. Sie besteht aus einer kreuzförmigen Acrylplatte, an dessen Unterseite insgesamt vier Pneumatikaktoren als Füße befestigt sind. Auf der Oberseite befinden sich die Ventile zur Ansteuerung, das Druckluft-Verteilersystem und die notwendige Elektronik (Mikrocontroller, Sensorik, Bluetooth-Modul). Der benötigte Luftdruck kann entweder extern zugeführt werden oder aus einer eingebauten CO₂-Kartusche kommen. Auch der Strom kann von den LiPo-Akkus an Bord geliefert werden. Neben dem mechanischen Aufbau werden ebenfalls alle benötigten Platinen entworfen, die Mikrocontroller-Firmware geschrieben und ein einfaches Protokoll entwickelt, um die Kommunikation zwischen dem Roboter und einem PC zu ermöglichen. Es ist hiermit möglich, einen Sprung auszulösen und die zeitliche Abfolge der einzelnen Ventile zu konfigurieren. Gleichzeitig können Sensordaten während des Ablaufs angefragt und aufgezeichnet werden, um den Sprung zu analysieren.

Bei den Versuchen zum vertikalen Sprung können die Ergebnisse aus der Aktoranalyse bestätigt werden, wenngleich die Leistung nicht ausreicht ist, um typische Hindernisse wie beispielsweise Treppen zu überwinden. Ursache ist vermutlich der begrenzte Luftstrom im System bedingt durch die einzelnen Komponenten, welcher eine stärkere Beschleunigung verhindert. Um den Sprung in eine bestimmte Richtung zu erreichen, werden zunächst die zwei Aktoren auf einer Seite des Roboters gefeuert, wodurch sich ein Kippen der Plattform in Sprungrichtung ergibt. Nach einer kurzen Zeitspanne bewirkt die Ausdehnung der anderen beiden Aktoren eine Linearbeschleunigung, schräg nach oben und nach vorne. Es werden unterschiedliche Aktivierungsfolgen und Richtungen untersucht und die Ergebnisse visualisiert; es ist ersichtlich, dass sich durch die Gewichtsverteilung und die leicht unterschiedlichen Eigenschaften der einzelnen Aktoren je nach Richtung eine optimale Steuerstrategie finden lässt, bei der die zurückgelegte Strecke maximiert wird.

Zur Korrektur von Abweichungen von der gewünschten Richtung wird ein simpler Lernalgorithmus entwickelt, der anhand des Richtungsfehlers nach einem Sprung die Timingfolge der einzelnen Aktoren leicht verändert, um den Effekten der Gewichtsverteilung und eventuell der schwächeren Aktoren entgegenzuwirken. Der Betrieb mit CO₂-Kartusche stellt sich als problematisch dar, da der zusätzliche Aufbau das Gewicht der Plattform signifikant erhöht, die Gewichtsverteilung verändert und nicht den gleichen Luftstrom wie eine externe Druckluftquelle bereitstellen kann.

Auch wenn nicht alle Probleme gelöst und aufgrund der vielen unbekannten Einflussfaktoren kein umfassendes Modell des Sprungvorgangs erstellt werden kann, bietet diese Arbeit einen Einblick in den Kontaktspunkt zwischen Soft Robotics und springenden Robotern.

Acknowledgements

Foremost, I would like to express my sincere gratitude to Prof. Lilong Cai at the Hong Kong University of Science and Technology (HKUST) for allowing me to pursue my Diploma Thesis under his guidance. My gratitude also goes to Prof. Kai Tang at HKUST for the technical advice as well as the financial support for realizing this project.

I would like to sincerely thank Prof. Georg Bretthauer at the Karlsruhe Institute of Technology (KIT) for agreeing to supervise and grade my thesis, as well as Prof. Tamim Asfour at KIT for providing constant support and feedback despite the geographical distance.

My sincere thanks goes to Mr. Feng Ni for being not only a great supervisor, but a good friend. Thanks also goes to my labmates Jie *Jack* Cao, Kin Chan, Long Kan, Mauricio Kendel, Kwun Pang *Nick* Law, Jun *Robin* Tao, Hon Chung *Tony* Wong and Man Tai Wu, thank you for the great teamwork and for making my stay at HKUST special.

Thanks also to the technical staff at HKUST, Mr. Ervine C.T. Lim (electronics, PCB etching), Mr. Thomas Chau (parts procurement), Mr. Roy K.M. Ho (high speed camera), Mr. Chi-Keung Kam and Mr. Chi-Shing Seto (machine workshop), without whom the making of the physical robot would never have been possible.

I thank Ms. Margit Rödder and Ms. Patricia Lichtblau from the InterACT office at KIT for enabling my exchange to HKUST.

Last but not least, I would like to thank my parents and my grandparents for their continuing support, not only for the duration of this thesis, but throughout my life.

Contents

1	Introduction	13
1.1	Motivation	13
1.2	Goal statement and scope	13
1.3	Thesis structure	13
2	State of the Art	15
2.1	Jumping robots	15
2.2	Soft robotics	16
3	The Soft Actuator	19
3.1	Basic design	19
3.2	Material selection	20
3.3	Mold design and casting process	20
3.4	Experiment: Static behavior of the actuator	22
3.4.1	Experimental setup	23
3.4.2	Hardware description	23
3.4.3	Test series I: Low pressure static test	24
3.4.4	Analysis and model creation	24
3.4.5	Test series II: High pressure static test	25
3.4.6	Model verification and conclusion	25
3.5	Experiment: Dynamic behavior of the actuator	27
3.5.1	Experimental setup	27
3.5.2	Hardware description	27
3.5.3	Test series III: Single actuator dynamic test	29
3.5.4	Test series IV: Multi-segment actuator dynamic test	32
3.6	Summary	35
4	The Jumping Robot Platform	37
4.1	Hardware description	37
4.2	Pneumatic system	42
4.2.1	Overview	42
4.2.2	Exhaust port	42
4.2.3	On-board pressure supply	44
4.3	Electronic system	44
4.3.1	Microcontroller board	44
4.3.2	Communications	47
4.3.3	Inertial Measurement Unit	47
4.3.4	Solenoid drivers	47
4.3.5	Power supply	47
4.4	Communication protocol	48
5	Experimental Evaluation	51
5.1	Vertical jumping	51
5.2	Directional jumping	52
5.2.1	Experiment description	52

5.2.2	Higher pressure and exhaust tests	53
5.2.3	Results	54
5.2.4	Sensor data	56
5.2.5	Heading control	58
5.3	Wireless/pipelineless operation	58
6	Summary and Outlook	61
6.1	Summary	61
6.2	Challenges	61
6.3	Further ideas	61
7	Appendix	63

1 Introduction

1.1 Motivation

Locomotion is one of the main research areas in robotics. Traditional terrestrial locomotion techniques such as wheeled locomotion and many legged designs are rather slow and not truly dynamic processes. Jumping, however, is an inherently dynamic, relying primarily on the agent's own velocity and inertia and Earth's gravity to generate a trajectory through the air. Ground-based mobile robots often struggle with challenges such as uneven terrain and high obstacles: situations that can be overcome by jumping.

Another emerging field is soft robotics, relying on elastic, compliant and deformable materials to achieve the desired functionality. Many traditional mechanisms require complicated mechanical structures to function; in soft robotics, complex movements often emerge from the characteristics of the material itself, combined with a specialized morphology, reducing the number of individual parts and increasing robustness. A lot of the research deals with developing systems for grasping objects, often mimicking nature. Another common theme is robot-human interaction, since soft and compliant materials are often safer for direct contact with people than hard and rigid structures. On the other hand, the usually broad topic of locomotion occupies a significantly smaller fraction of the literature in the niche of soft robotics.

1.2 Goal statement and scope

So far, little has been done in attempting to merge the two fields of jumping locomotion and soft robotics. This thesis thus attempts to bridge that gap, describing the development and construction of a robotic platform capable of jumping locomotion by employing soft pneumatic actuators to generate the propulsion force for the jump. To this end, the actuators themselves have to be developed and their performance measured. Afterwards, the robot itself is designed and assembled. A series of tests are performed to gauge the effectiveness and usefulness of this kind of locomotion.

The robot described here is a hard/soft hybrid. The jumping motion is enabled by soft, silicone elastomer pneumatic actuators, yet the supporting platform consists of a rather rigid structure. It is designed to be a proof-of-concept device to study the behavior of such a setup without delving into a detailed examination of the continuum mechanics of the soft material or a full mathematical model of the jumping process. Nevertheless, it should allow a basic understanding of the actuators' behavior and of the underlying mechanics. Ultimately, it should pave the way for further investigation at the junction between soft robotics and jumping locomotion.

1.3 Thesis structure

First, a brief overview of the two major subjects to be merged (jumping locomotion, soft robotics) is given in Chapter 2, listing some examples of the existing literature in each research area.

Chapter 3 details the development of the silicone actuator to be used. It gives a detailed description of the material, the manufacturing process and the characteristics of the resulting part, by analyzing its behavior with both static and dynamic pneumatic pressure applied to the actuator.

Chapter 4 then deals with the design of the robot platform onto which the actuators are attached. This includes the mechanical construction, the pneumatic system and the on-board electronics, exploring each subassembly in detail.

Once the robot is built, a number of experiments are conducted in Chapter 5. Its performance in both vertical jumping and directional locomotion is measured and visualized. An error correction algorithm used to compensate for deviations from the platform's intended trajectory is implemented and evaluated. The operation of the robot with on-board electrical and pneumatic power supplies is also described.

Finally, Chapter 6 summarizes the findings from the tests, enumerates a number of challenges encountered and gives an outlook on further research ideas to continue developing soft jumping robots.

2 State of the Art

2.1 Jumping robots

In the history of robotics, many terrestrial locomotion techniques for mobile robots have been developed, ranging from the rather obvious choice of wheeled mobility [1] all the way to the very complicated field of human-inspired bipedal locomotion. There are countless designs for legged robots [2], with one [3], two [4], three [5], four [6], six [7] [8] and more legs, a comprehensive compilation of which would be outside the scope of this text. Limbless locomotion techniques are often inspired by nature, such as a crawling caterpillars [9] or snakes [10]. Some robots even employ their entire body as a rolling surface [11] or use amoeba-like cytomastic streaming within a soft body to propel themselves forward [5].

A very promising approach for robot locomotion is jumping, as it can be very useful to overcome obstacles (oftentimes multiple times higher than the robot itself). Also, it is a very interesting research fields as it is by definition a dynamic process, using a rapid energy release and the jumper's own inertia to function.

A broad overview on the topic is provided by Armour et al. [12], while Dufresne et al. [13] cover the basic physics of jumping. As always, nature often serves as the best inspiration for robotic designs: be it frogs [14], fleas [15] or kangaroos [16], the animal kingdom provides a plethora of mechanisms and strategies. Interestingly, gears (which were believed to be a uniquely man-made invention) have been found to have evolved in animals as well, allowing the planthopper *Issus* to synchronize the motions of its hind legs increasing the precision of its jump [17] [18].

Some developments combine jumping abilities with more traditional wheeled [19] [20] or walking modes [21] [22]. Here, the robot's capabilities are extended by the jumping mode with regards to traversing rough terrain and overcoming obstacles, while others rely on jumping as the sole strategy for locomotion.

Many jumping robot designs use an electric motor to store energy in a spring or similar device which is then locked in place by a ratchet-like mechanism [23] or an eccentric cam [24] [15] [25]. After releasing the lock, the energy is explosively released, expanding the leg and propelling the robot upwards/forwards. Since the flight of these very light robots is often unstable, self-recovery capabilities have been used in many cases, either by the inherent mass distribution [26] or by encasing the robot in a small sphere made out of carbon fiber and shifting its center of gravity after the jump to orient itself [27] [28]. Some designs possess the ability to enter a gliding mode once in the air by extending airfoils, greatly extending their range [29]. Applications in space exploration have been proposed by Burdick and Fiorini [30]; jumping could play a major role in environments where the constraints set by gravitation are less pronounced than on Earth.

Miniature jumping robots in the range of a few mm using microfabrication techniques are also under investigation [31], at scales where aerodynamic drag during the airborne phase becomes a significant factor in the jumping performance, unlike larger robots where the device's own inertia outweighs these effects by far.

While most robots possess legs of some kind that exert force on the ground to accelerate upwards, there are some notable exceptions. Kim et al. [32] employ a jet of air escaping a reservoir for upwards propulsion of their wheeled robot to overcome steps. Yamada et al. [33] present an approach based on "closed elastica", using the energy liberated upon the buckling of a deformed elastic strip as it returns to an equilibrium state. Similar approaches by deforming an elastic ring into a shape with high potential energy and releasing it are presented by Sugiyama and Hirai [34].

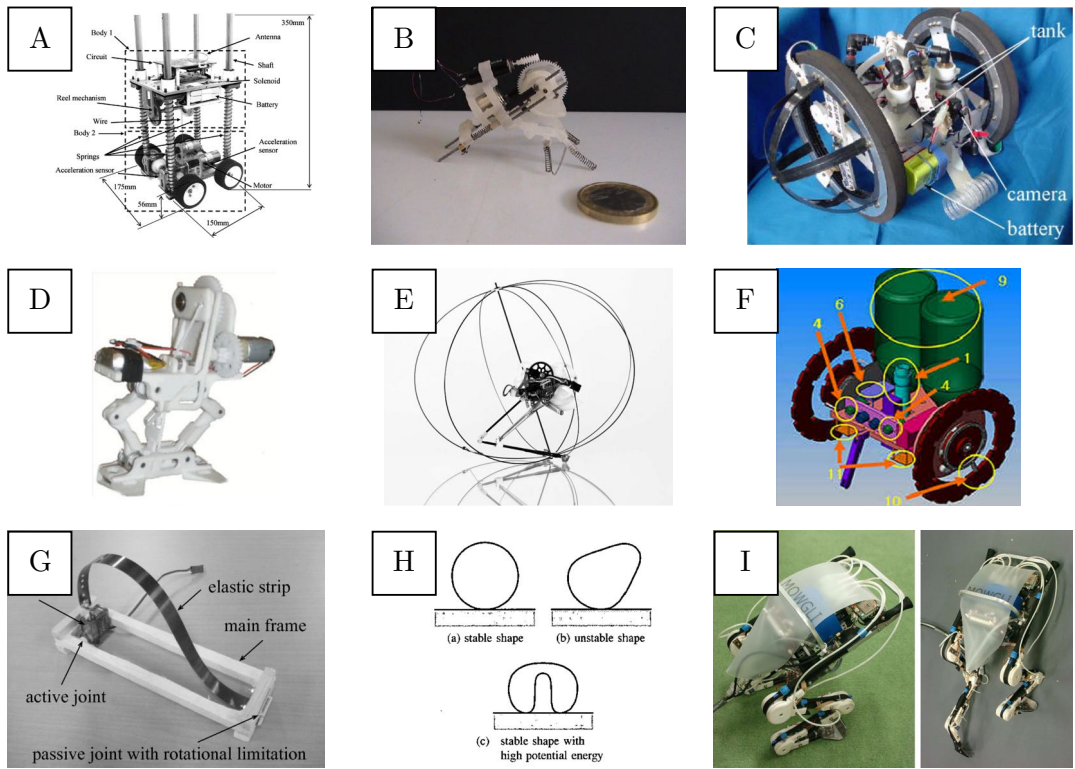


Figure 2.1: Jumping robots; A:[20] B:[15] C:[19] D:[23] E:[27] F:[32] G:[33] H:[34] I:[35]

2.2 Soft robotics

As opposed to traditional 'hard' robotic systems made of rigid parts and precisely defined joints, soft robotics is a research area that focuses on systems that are inherently compliant due to their design and material properties [36]. Often, cast silicone rubber or other elastomers are used to make up the shape of the robot, be it only the hinges (resulting in a hard/soft hybrid) or the entire body structure. Kim et al. [37] provide a good overview on the current state of soft robotics, while Majidi [38] outlines some potential applications in health care, human assistance and wearable devices, among others. Especially when interacting with humans, soft robots are often safer and more intuitive for users than their 'hard' counterparts. In many cases, an intelligently designed body structure can take over some of the functionality of a robot's controller (e.g. for a walker's stability) by what is known as *morphological computation* [39], thus greatly reducing overall design complexity.

As always, nature yields numerous examples of soft bodied animals that have been adapted into a robotic form, as animals often display abilities unimaginable for more rigid artificial systems. Notable examples include adaptations of the the dexterous manipulation abilities of octopus tentacles [40] and elephant trunks [41] or the elegant undulating movements of a manta ray [42]. The GoQbot caterpillar [43] uses a sudden burst of air pressure inside its actuators to curl up into a ball and roll away from danger just like its natural role model.

The most common types of fluidic actuators used in soft robotics include McKibben type pneumatic artificial muscles (PAMs) and bellows-like actuators. McKibben PAMs [44] are sometimes used in combination with classic springs as antagonists to return the muscle to its initial position after removing internal air pressure [45]. Hosoda et al. [46] and Niiyama et al. [35] have employed them in their jumper designs.

Bellows-like actuators consists of one or generally many segments joined along a common axis, that

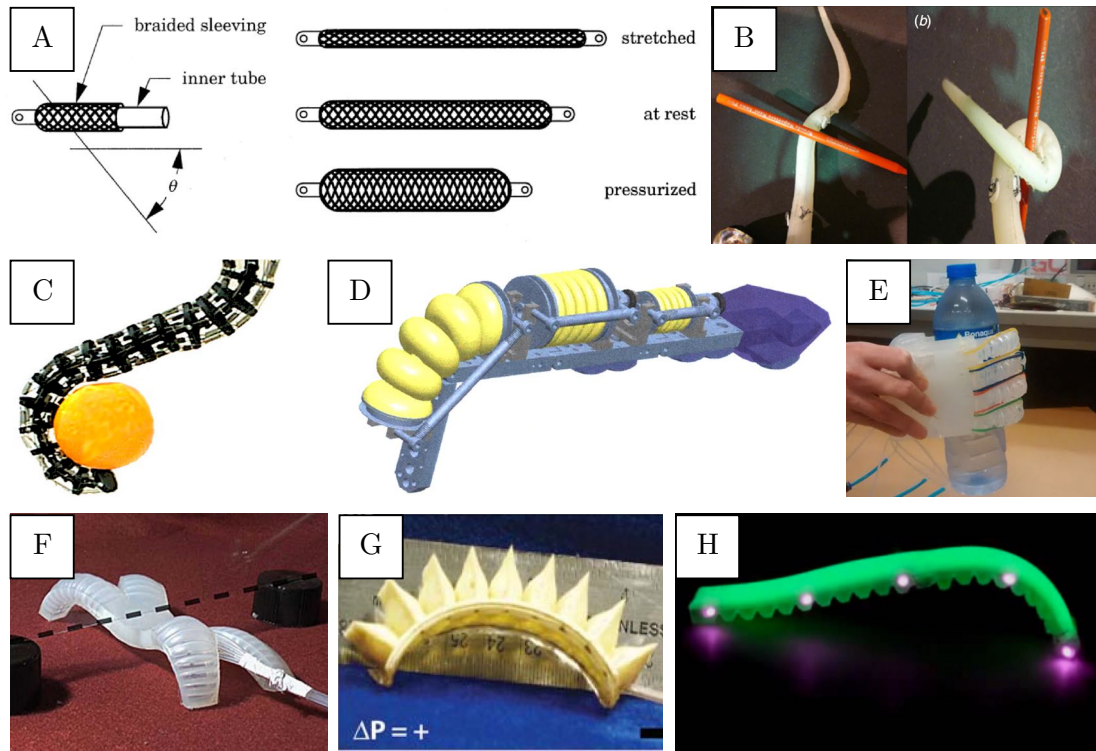


Figure 2.2: Soft robots; A:[44] B:[40] C:[41] D:[47] E:[51] F:[52] G:[53] H:[43]

expand axially under pneumatic pressure, and are used for both linear and bending motions in robotics. A marvelous example of dexterity is the human hand and as such, it has been mimicked in robotics many times. An example of a hybrid hard/soft structure is the hand of the humanoid robot ARMAR III [47], using the bellows actuators presented in [48]. Fully soft hands have also been presented: Deimel and Brock [49] employ a single long actuator for each finger; Noritsugu [50] uses a comparable approach in a power-assisted glove for rehabilitation purposes. Law et al. [51] at the Hong Kong University of Science and Technology use three discrete joints per finger, each actuated with its own bellows. Their know-how in handling and casting silicon rubber was of key importance for the work presented here.

The Whitesides Research Group has demonstrated the feasibility of a fully soft walker using air pressure [52]. By varying the material thickness on different sides of the structure, different deformations result when injecting pressurized air. The same group has also conducted research on puncture resistant silicone structures for increased longevity of soft robots [53].

3 The Soft Actuator

3.1 Basic design

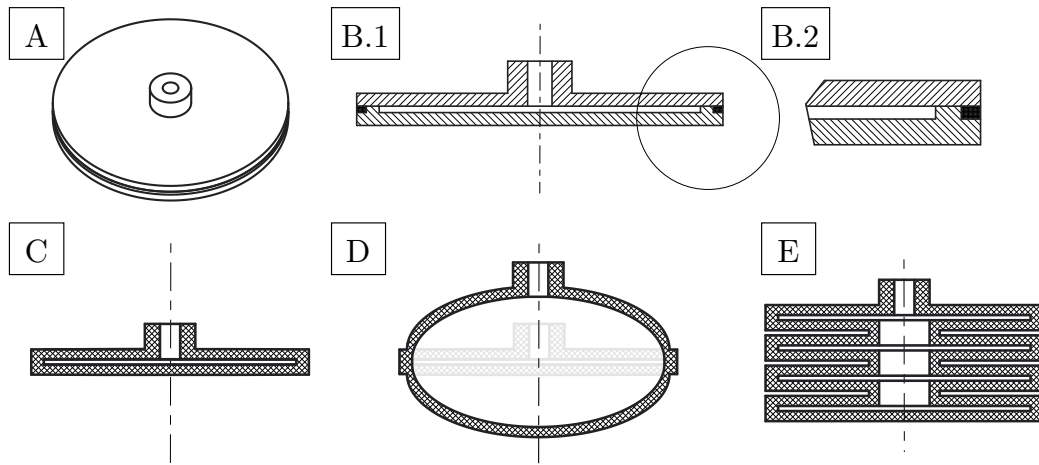


Figure 3.1: The soft pneumatic actuator - overview

The overall shape of the pneumatic actuators used as the robotic platform's legs is shown in Figure 3.1A. It is based mostly on the design developed by Law et al. [51], and bears a resemblance to the actuators used for bending joints in other robots such as ARMAR III's palm and finger joints [47], with the difference that it is used here for linear actuation as opposed to bending. A flexible silicone polymer was used as the material (see 3.2).

The cross section (shown in Figure 3.1B.1) reveals the structure of the actuator. It starts with a neck that allows for easy mounting onto a platform or testing jig. By inserting it into a hole with a slightly smaller diameter than the neck itself, a tight fit is ensured and then further reinforced by the insertion of the air supply pipe. The friction creates a seal that withstands the full range of operating pressures (up to 0.15 MPa static and 0.6 MPa in bursts of up to 50 ms) without leakage. Below the neck, the actual body of the actuator is comprised of two circular discs joined at the outer perimeter (see closeup in Figure 3.1B.2), thus creating the air chamber, with the inlet on the top. When no internal pressure is applied, the actuator lies flat (Figure 3.1C); an increase in pressure causes it to expand outwards (Figure 3.1D). The effective diameter of the inner chamber is 50 mm, which was found to be a good compromise between easy manufactureability (tests with smaller diameters often resulted in failed parts) and reasonable internal volume, as larger actuators would require a much higher flowrate to achieve the same rate of expansion, possibly exceeding the capabilities of the other elements in the pneumatic system.

A multi-segment actuator (Figure 3.1E) was also developed for some of the tests (see 3.5.4). Following the same basic structure, the individual segments were joined by smaller rings. The modular design allows for stacks of arbitrary numbers of segments.

3.2 Material selection

During the early stages of development, three different types of silicone were considered as candidates for the casting of the pneumatic actuators. Table 3.2 lists the material properties of each material.

		EcoFlex 00-30	ShinEtsu KE-1310ST	Sylgard 184
Density	kg/dm ³	1.07	1.08	1.04
Hardness	Shore A	30	40	44
Tensile strength	MPa	1.4	5.5	7.1
Elongation	%	900	350	120
Tear strength	kN/m	5.3	25	0.8
Linear shrinkage	%	0.1	0.1	

Table 3.1: Material comparison - physical properties

First tests in casting actuators with these three materials allowed developing a more tangible feeling for their properties and their behavior during casting and during use. The main findings are listed in Table 3.2.

	EcoFlex 00-30	ShinEtsu KE-1310ST	Sylgard 184
Pressure resistance	-	++	+
Tearing resistance	+	+	-
Low bubble formation	-	0	+
Availability	+	++	+

Table 3.2: Material comparison - key parameter rating

The highly elastic EcoFlex 00-30 was unable to withstand air pressures over 0.05 MPa and was deemed too sticky to be useful. It absorbed dirt very quickly, had heavy bubble formation inside the cast part and a lot more material would have been needed to create a stable structure. Sylgard 184 displayed almost no bubble problems and was able to resist higher pressures, but was very sensitive to imperfections within the material and displayed a tendency to tear at sharp edges, which are inevitable in laser-cut acrylic molds. Finally, ShinEtsu KE-1310ST was chosen for its good material properties, for being able to withstand a wider range of pressures and for its ease of use.

3.3 Mold design and casting process

For reasons of cost, easy availability and low lead time due to in-house manufacturing, laser cut PMMA¹ (acrylic) sheets were used to make up the pieces of the mold. Sheets of different diameters were separately laser-cut and later assembled using M4 screws through dedicated alignment holes to ensure a perfectly concentric placement. Special acrylic glue is used to keep the assembly together. To achieve the inner chamber, every actuator (or module of a multi-segment actuator) is cast in two parts and then glued together. Figure 3.2 shows the arrangement of mold layers required to cast a single actuator. In the top mold, the port for the supply pipe is kept free by use of an additional M4 screw driven through the center of the mold. The bottom mold only uses the center screw as a centering aid for the inner disc (which creates the inner chamber). Once glued in place, the screw is removed and its hole covered with adhesive tape to prevent leakage of the uncured silicone (as in Figure 3.3B).

The assembled molds can be seen in Figure 3.3A and 3.3B. Once the silicon has been carefully poured into the mold taking care to avoid excessive bubble formation, remaining visible bubbles are manually

¹PMMA: Poly(methyl methacrylate)

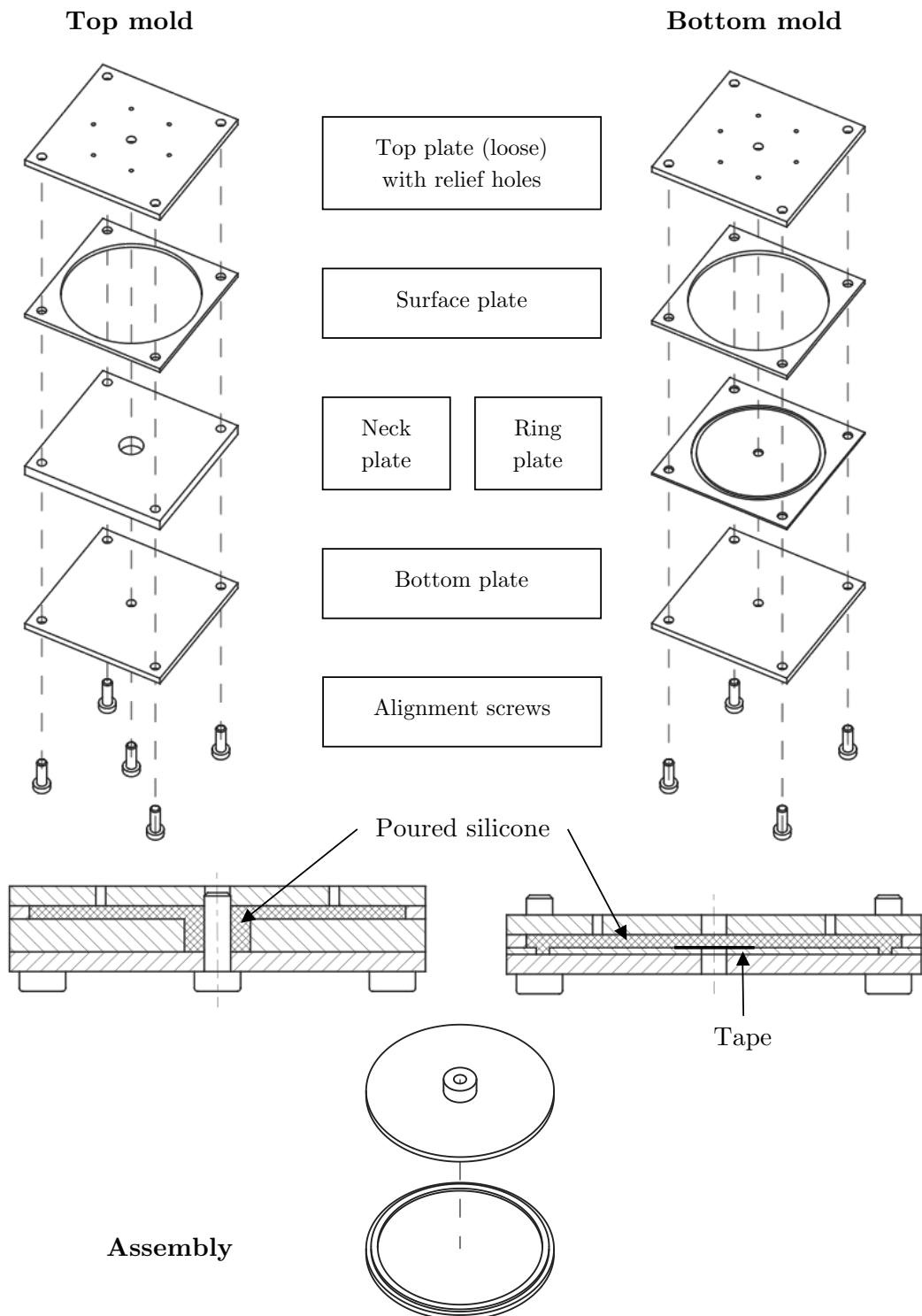


Figure 3.2: Silicone actuator molds (exploded view)

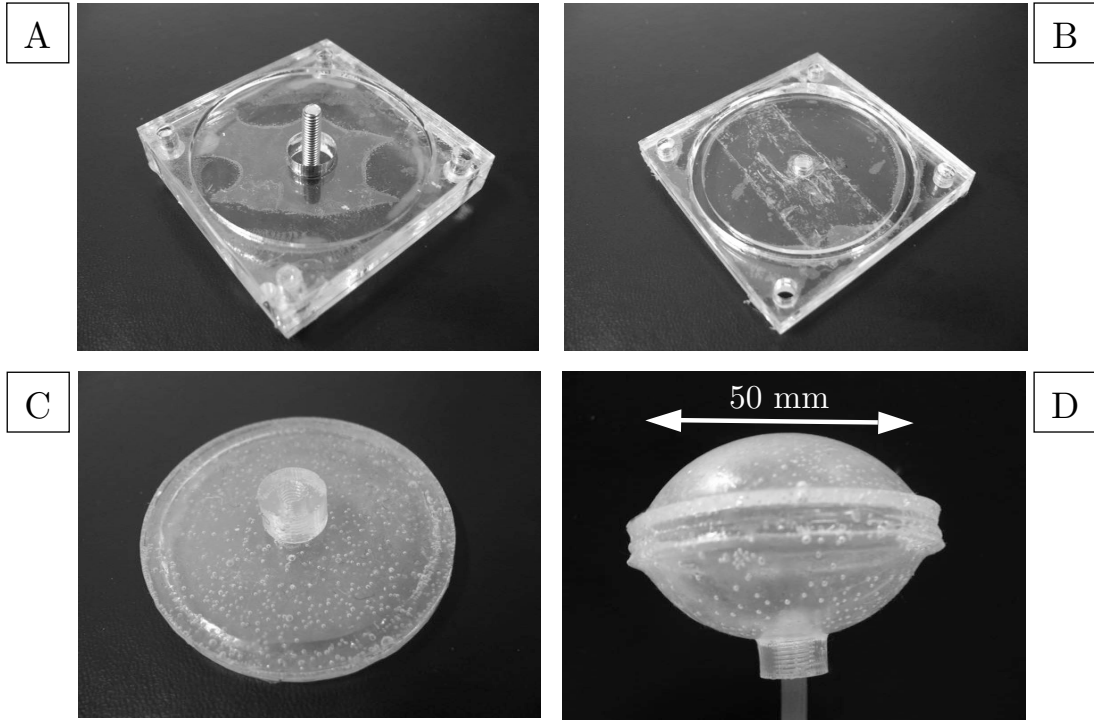


Figure 3.3: The soft pneumatic actuator - photos

sucked out using a syringe in order to prevent weak points in the material. When the silicone is clear of major defects, a final cover piece is placed onto the mold assembly to generate a smooth surface on all sides of the part. Small relief holes in the top cover plate allow excess silicone to escape as it is pressed down.

In accordance to the ShinEtsu datasheet, the molds are placed in an oven at 95 °C for approximately 25 minutes to speed up the curing process. After curing and cooldown to room temperature (passive air cooling), the pieces are demolded, excesss material cut away and a circle of freshly mixed silicone carefully added around the ridge of the bottom half as represented by the black square in the cross-section of Figure 3.1B.2. The two halves are carefully aligned, pressed together manually and placed to cure again. After a second cooldown phase, the actuator is ready for use (Figure 3.3C) and pressurized air can be injected (Figure 3.3D). During testing, the remaining bubbles posed no problem during use and were never a failure point of the actuator; all ruptures recorded occurred at the seam between the top and bottom halves.

3.4 Experiment: Static behavior of the actuator

The first step to characterizing the behavior of the pneumatic actuators was to determine the force F exerted by the actuator at different degrees of inflation/expansion s under a constant internal air pressure p . To this end, a jig was designed and various tests carried out to generate a model of the actuator's behavior, $F = f(s, p)$.

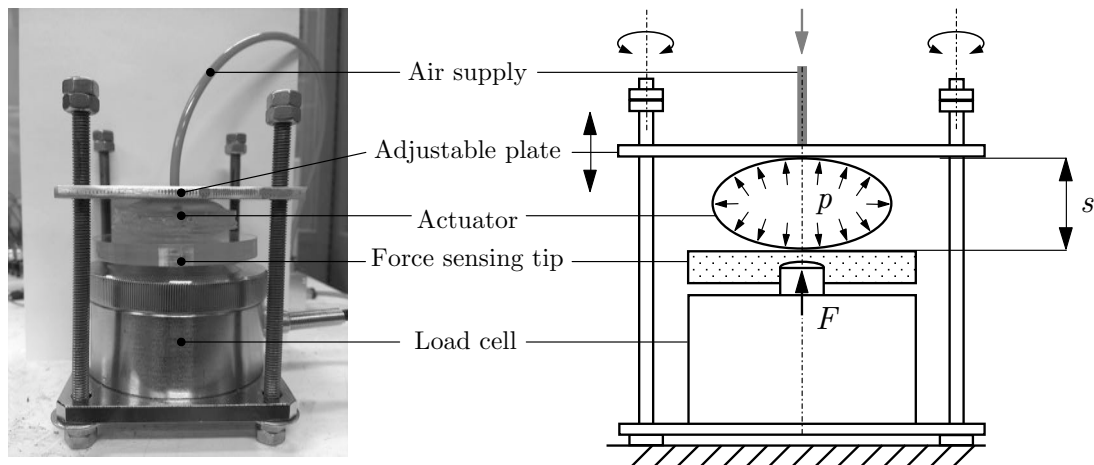


Figure 3.4: Static testing - experimental setup

3.4.1 Experimental setup

The testing platform (as pictured in Figure 3.4) is comprised of a load cell and a mounting plate, with the actuator to be tested placed in between. By design, the force-sensing tip of the load cell is a small shaft with a rounded top, unsuitable to directly detect the force of the actuator, since it would simply wrap around the tip and cause an erroneous measurement. A thick acrylic sheet with a 10 mm blind hole was placed on the tip to absorb the complete force of the actuator and concentrate it on the sensor tip. It is held in place by a press fit around the sensor shaft. The square-shaped mounting plate holds the actuator above the load cell in its central hole using a tight friction fit around its inlet port. It is linked to the load cell by way of four M6 threaded rods, one on each corner. These allow the relative distance of the mounting plate to the load cell by adjusting the respective M6 nuts, therefore allowing the actuator to expand to a controlled size along its axis and to press against the load cell's sensor tip through the acrylic sheet. The 1 mm pitch of the M6 rods proved especially convenient for keeping track of the current position by measuring the number of turns (i.e. one turn = 1 mm) as no absolute scale was used for design simplicity.

3.4.2 Hardware description

Initially, a load cell capable of measuring weights of up to 3 kg was used (see appendix for the full datasheet). Later, a second load cell of identical outer dimensions with a rated load of 20 kg became available for experiments under higher applied pressures. The displacement of the sensor itself under pressure is negligible, as it is based on a strain gauge attached to a rigid metal bar.

Since the load cell is based on a Wheatstone bridge, a simple amplifier circuit was constructed around the INA114 Precision Instrumentation Amplifier IC in accordance with the datasheet (see Figure 3.5). Output values were measured by a 10-bit A/D-converter on an ATmega328P microcontroller running the Arduino firmware and displayed on screen for logging.

Applying a voltage of ± 6 VDC to the load cell and using a gain of 152.5 (using a gain resistor of 330Ω) yielded an output of ± 5.25 VDC on the μ C input pin which. The microcontroller has a specified tolerance of -0.5 to 5.5 VDC on its input pin when running on 5 VDC, which did not pose a problem as negative voltages only occur when the load cell is under *tension*, which does not occur in this setup.

To gain the exact factor to convert the raw sensor readings into force measurements, compensate for any inaccuracies in the mechanical setup and confirm the linearity of the system, a calibration step was performed before making the measurements by placing known calibration weights on the sensor and logging the corresponding output values. After offsetting the values by the value measured without any

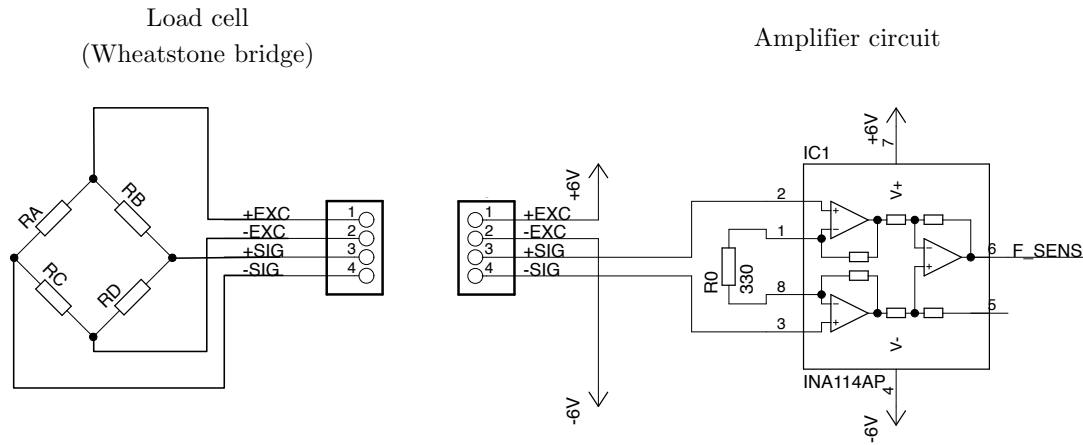


Figure 3.5: Static testing - amplifier circuit

load, a high linearity was observed, especially for the 20 kg load cell (see Figure 3.6 top).

3.4.3 Test series I: Low pressure static test

For the first test, the actuator was allowed to expand along its axis between $0 \text{ mm} < s < 20 \text{ mm}$, in 0.5 mm increments. At each position, the pressure was increased to a maximum of 80 kPa in 10 kPa steps, and the force measured after a brief period of stabilization. This included a measurement at $p = 0 \text{ kPa}$ at every position s to improve accuracy and compensate for a possible drift in the sensor output. After each series, the pressure was released and the distance between the load cell and the mounting plate increased by one increment. If the maximum capacity of the sensor was reached before the final pressure, the series was aborted prematurely to avoid damage to the setup.

The test allowed plotting complete curves for lower pressures up to 30 kPa, from 0 mm (the actuator firmly clamped with no ability to expand) $< s < s_{max}$, the maximum possible expansion when the actuator eventually stops touching the sensor plate (see Figure 3.6 bottom left). At higher pressures, the sensor was overloaded at small expansions and, additionally, in some cases the actuator did not reach its full expansion within the range allowed by the rods. The actuator failed (rupture at the seam between the two cast halves) during the attempt to measure the force at $s = 19.5 \text{ mm}$ $p = 90 \text{ kPa}$. Nevertheless, enough data was gathered to analyze the trend and venture some predictions about the actuator's behavior.

3.4.4 Analysis and model creation

The measured force at $s = 0$ showed to be 50% to 62% of the theoretical maximally reachable force ($F = p A$), with higher ratios achieved at higher pressures. The force over expansion function for a specific pressure ($F(s, p = const)$) seemed to follow a quadratic formula, with the minimum point being reached at $s = s_{max}$.

Two assumptions were made from the data to allow predictions for higher pressures and/or larger expansions:

- The initial force at $s = 0$ was assumed to be proportional to the actuator's internal pressure following the pressure law ($F = p A$), albeit reduced by a certain factor due to efficiency and other effects left unconsidered.

$$F_{max}(p) = C p$$

The obtained data supported this assumption very well.

- The maximum achievable expansion at a given pressure $s_{max}(p)$ seemed to follow a linear pattern, with a certain offset from a proportional behavior.

$$s_{max}(p) = V p + W$$

Using these assumptions, a quadratic model for predicting the force was created.

$$F(s, p) = X s^2 + Y s + Z$$

with $X, Y, Z = f(s_{max}, F_{max})$, using the boundary conditions:

- $F(s = 0, p) = F_{max}(p)$, the maximum force is achieved at zero expansion;
- $F(s = s_{max}(p), p) = 0$, a fully expanded actuator exerts no external force;
- $\frac{\partial F}{\partial s}(s = s_{max}(p), p) = 0$, the force diminishes smoothly up to the actuator's full expansion.

The resulting curves were a good approximation to the measured data points, often resulting in a more conservative estimate of the achievable force than what was actually measured (dashed lines in Figure 3.6 bottom).

It should be noted that there is a visible jump in all data series at $s = 9.5\text{mm}$, possibly caused by a slight voltage variation in the force sensor's amplifier circuit. The true behavior of the actuator is believed to fit the predictions even better than what the data shows.

3.4.5 Test series II: High pressure static test

A second series of tests was conducted using a version of the sensor capable of measuring loads of up to 20 kg, eliminating previous limitations. Pressures of up to 160 kPa could now be measured from the very start at $s = 0$; higher pressures were not attempted at the fear of prematurely damaging the actuator. Since the expected trend of the curves was already known, pressure steps were doubled to 20 kPa and expansion increments increased to 2 mm. With the current setup, only displacements of up to $s = 22\text{ mm}$ could be recorded due to the limitation of the threaded rods. Also, the actuator failed (same failure mode, rupture at the seam between the halves) at $p = 140\text{ kPa}$ and $s = 22\text{ mm}$.

3.4.6 Model verification and conclusion

Despite using a different load cell and a new actuator (as the initial one failed), data in the lower pressure range match the model's prediction quite closely (Figure 3.6 bottom right). However, as pressure increases, the model produces estimates of F_{max} up to 12 % lower than the measured value, i.e. it is too conservative, following the trend described in 3.4.4 of higher pressures reaching forces closer to the theoretical value. For increasing expansion s on the other hand, it produces numbers higher than the measured data, showing that the assumption that the maximum expansion of the actuator s_{max} increases linearly with the applied pressure clearly does not hold true throughout the range of pressures used. Partially, this could be due to a radial expansion of the actuator, resulting in a larger area on which the pressure (held constant by the regulator) could exert its force.

No improved model was created at this point, as there was not sufficient data to improve the proposed boundary conditions (a larger test setup which allows the actuator to expand further than 22 mm would be needed to gain more values for s_{max}), and characterizing the actuator in detail is not the focus of the current work, although it is a topic deserving further investigation.

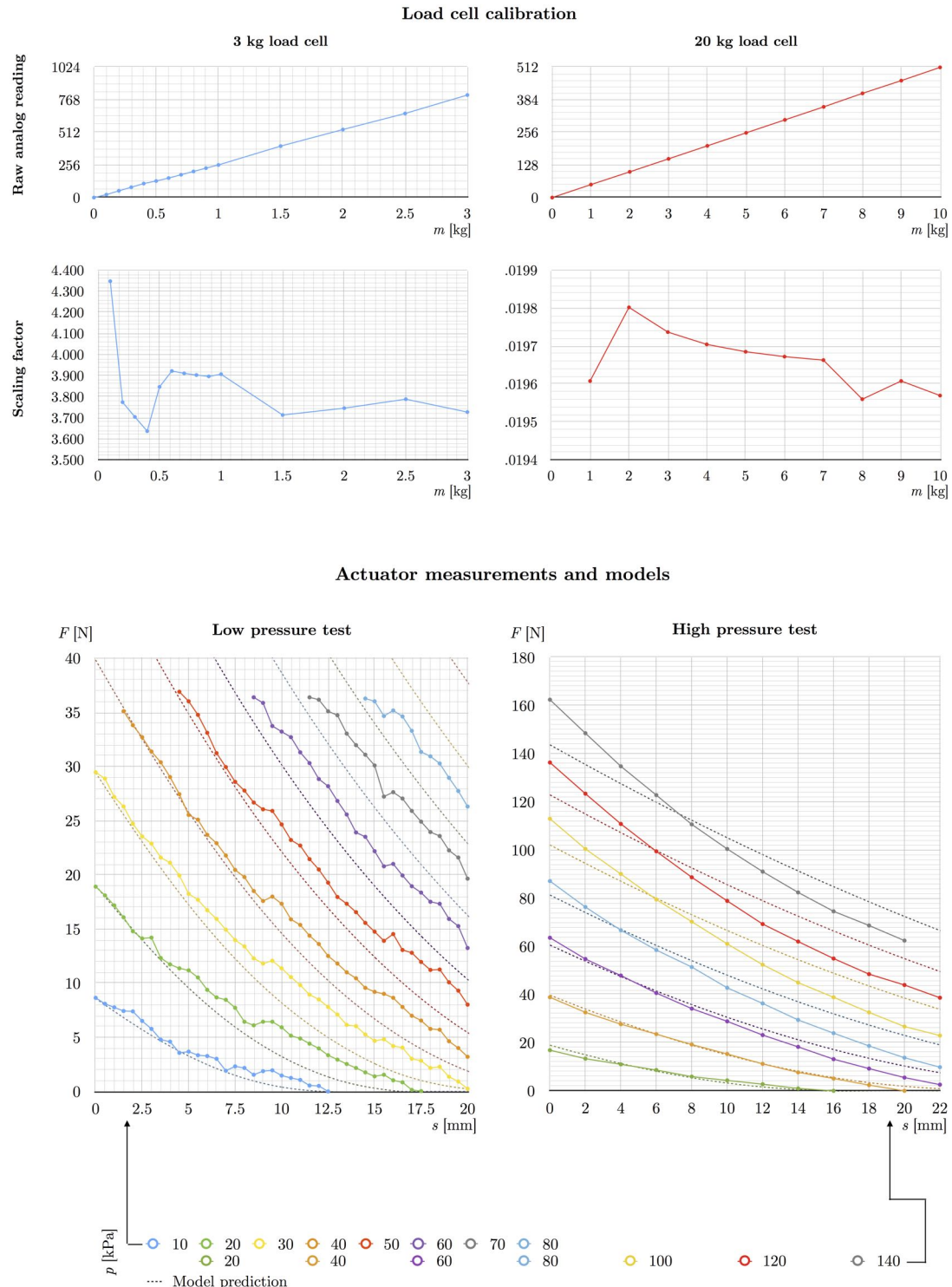


Figure 3.6: Static testing - results

3.5 Experiment: Dynamic behavior of the actuator

To determine whether the actuator is suitable for achieving the jumping motion of the robot, testing the dynamic behavior of the actuator under a sudden burst of pressure is of prime importance.

3.5.1 Experimental setup

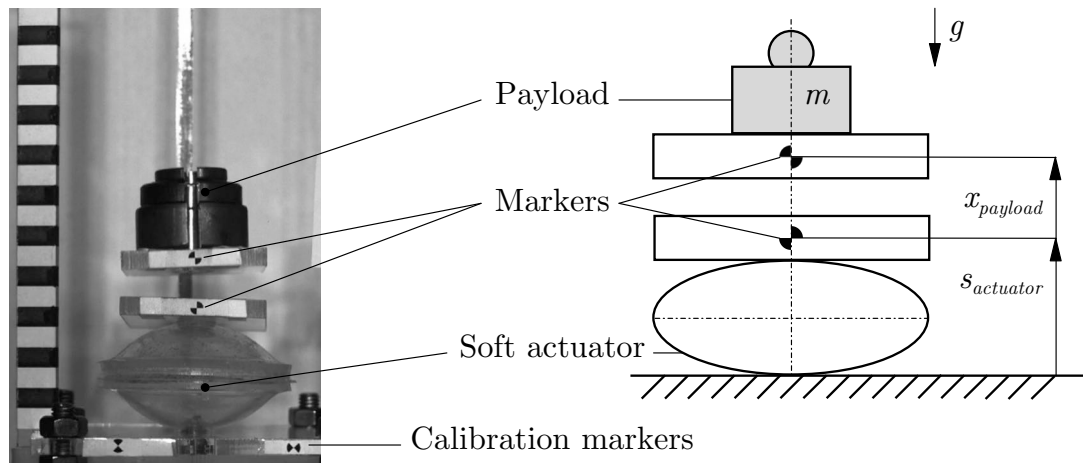


Figure 3.7: Single segment actuator - dynamic test setup

Figure 3.7 shows the design of the experiment. The actuator is placed in a holding jig, with the neck and supply pipe facing downwards. It is connected to a pressure-regulated air supply through a normally closed solenoid valve. The valve is then opened for a short period of time to generate a burst of pressure inside the actuator, by an electrical pulse sent by a microcontroller. The same pulse triggers the recording of a high speed camera to record the actuator's expansion process. For some of the tests, different weights were loosely placed on top of the actuator and allowed to fly into the air, simulating the mass of the final robot platform being accelerated upwards. Special markers on the actuator as well as on the payload allow tracking their trajectory using image recognition algorithms for plotting and analysis.

3.5.2 Hardware description

The valve used is a SNS 3V1-08-DC24V, operating at 24 VDC. It was opened after issuing a command to an Atmel ATmega328P microcontroller running an Arduino program, which sent a 50 ms pulse to a FQP30N06L MOSFET² to drive the valve and trigger the camera's recording mode synchronously. For details on the electronics layout, refer to 4.3. Datasheets of all components can be found in the appendix.

3 mm printed markers were used for tracking the positions, consisting of a circle with two white and two black quadrants as seen in Figure 3.7. A custom actuator was manufactured for this test, with a built-in cylindrical knob on the surface opposite the neck. The first marker was placed on the side of a small acrylic plate attached to this knob through its central hole. The second marker (on a similar plate) was attached to the payload using a small amount of adhesive putty; it was rotated by 90° with respect to the first one to distinguish it. Tracking both markers allowed to accurately determine the 'liftoff point' at which the payload separates from the actuator and enters the free-fall phase. Additional markers rotated by 45° and 135° respectively were placed on the fixed platform at a known distance to allow for calibration by matching the detected pixel distance between markers to their physical distance. For simplicity's sake, no other calibration or distortion compensation was implemented. The camera was

²MOSFET: Metal-Oxide-Semiconductor Field-Effect Transistor

placed at about 80 cm from the setup and placed so that its main axis was horizontal and the entire range of the acceleration visible (At higher pressures, the payload would occasionally fly off the visible area, but not within the time frame of interest). An additional scale with steps every 5 mm was placed to the side of the actuator to allow for quick visual estimation of a point's height during and after the tests.

1	1	1	0	-1	-1	-1
1	1	1	0	-1	-1	-1
1	1	1	0	-1	-1	-1
0	0	0	0	0	0	0
-1	-1	-1	0	1	1	1
-1	-1	-1	0	1	1	1
-1	-1	-1	0	1	1	1

-1	-1	-1	0	1	1	1
-1	-1	-1	0	1	1	1
-1	-1	-1	0	1	1	1
0	0	0	0	0	0	0
1	1	1	0	-1	-1	-1
1	1	1	0	-1	-1	-1
1	1	1	0	-1	-1	-1

0	-1	-1	-1	-1	-1	0
1	0	-1	-1	-1	0	1
1	1	0	-1	0	1	1
1	1	1	0	1	1	1
1	1	1	0	-1	0	1
1	0	-1	-1	-1	0	1
0	-1	-1	-1	-1	-1	0

0	1	1	1	1	1	0
-1	0	1	1	1	0	-1
-1	-1	0	1	0	-1	-1
-1	-1	-1	0	-1	-1	-1
-1	-1	0	1	0	-1	-1
-1	0	1	1	1	0	-1
0	1	1	1	1	1	0

Figure 3.8: Marker detection - convolution matrices

The camera used is a Vision Research Phantom. Images were recorded for the 250 ms following the trigger signal sent from the microcontroller synchronous to the opening of the valve. A framerate of 2000 fps and a resolution of 800x600 px was used for recording and the result compressed using a H.264 encoding at 5000 kbps for a good compromise between image quality and resulting file size.

For analysis, the resulting camera frames were analyzed using a simple convolution algorithm: The grayscale image of each video frame was convoluted with a matrix resembling each of the employed markers. In practice, a 7x7 matrix was able to detect virtually all markers (see Figure 3.8). The pixel with the highest value after each convolution was chosen to represent the respective marker. Its distance to its initial position (in the first video frame) was then output for logging. The fixed calibration markers on the platform are only analyzed in the first frame of every video. The result is a set of curves representing the motion of the trackers with approx. 0.2 mm spatial (the scale of the image being 5.6 to 6.1 px/mm) and 0.5 ms temporal resolution.

3.5.3 Test series III: Single actuator dynamic test

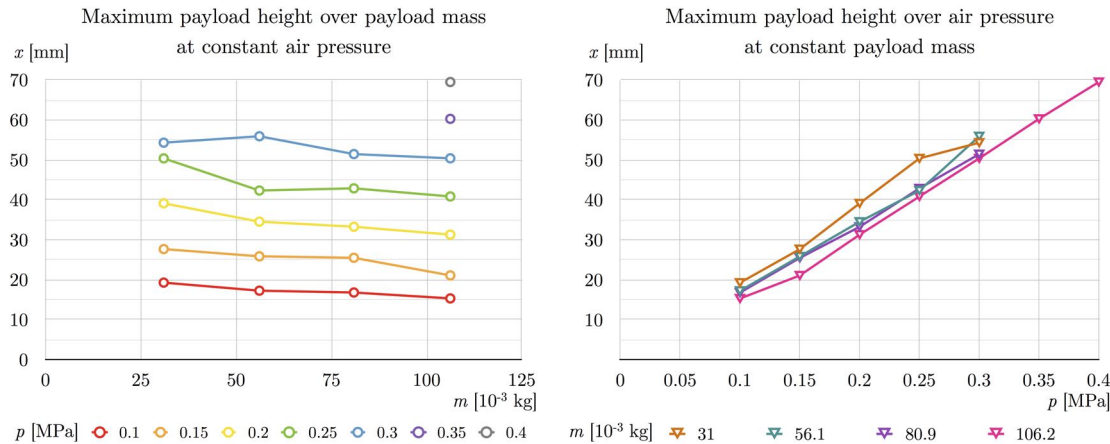


Figure 3.9: Single segment actuator - dynamic test evaluation

For the single actuator, a total of 27 tests were performed, with pressures ranging from 0.1 to 0.4 MPa and loads up to 0.106 kg, including a series with no additional payload. For each run, the maximum height reached by the payload mass was recorded.

In 23 out of 27 runs, not a single misdected marker was found. In the four remaining cases, outliers always occurred after the payload reached its peak height and began descending, which sometimes resulted in a tumbling motion causing the markers to rotate and preventing reliable detection. Manual pruning of the data was easily performed by visually identifying and removing the outliers, which always occurred after the payload had reached its peak altitude and therefore not in the region of interest for this experiment.

The data was visualized in different ways. Firstly, the relationship of payload mass to maximum jumping height was graphed, with multiple series representing different air pressures. Subsequently, the jumping height over applied air pressure was visualized with one series for each payload used (Figure 3.9).

The maximum reached height relates linearly to the applied air pressure, declining only slightly as the mass of the payload increases. A possible explanation could be that, rather than the static force of the air pressure (which at higher pressures could amount to over 1000 N), the linear momentum transferred to the payload plays the role in determining the height, and the transferred energy might itself depend on the payload mass. As it was not possible to continuously measure and quantify the progression of pressure buildup and the force on the payload during the acceleration phase, a detailed mathematical description could not be created.

By looking at the graphs of the marker positions over time, a number of observations on the actuator's behavior are made possible (Figure 3.10). A typical test run consists of various phases, starting at the moment where the solenoid valve and camera are synchronously triggered.

An aggregated view of all the tests performed can be found in Figure 3.11 arranged by payload weight; the colors signify varying pressures. Only the first 150 ms are shown for a better view of the initial acceleration phase.

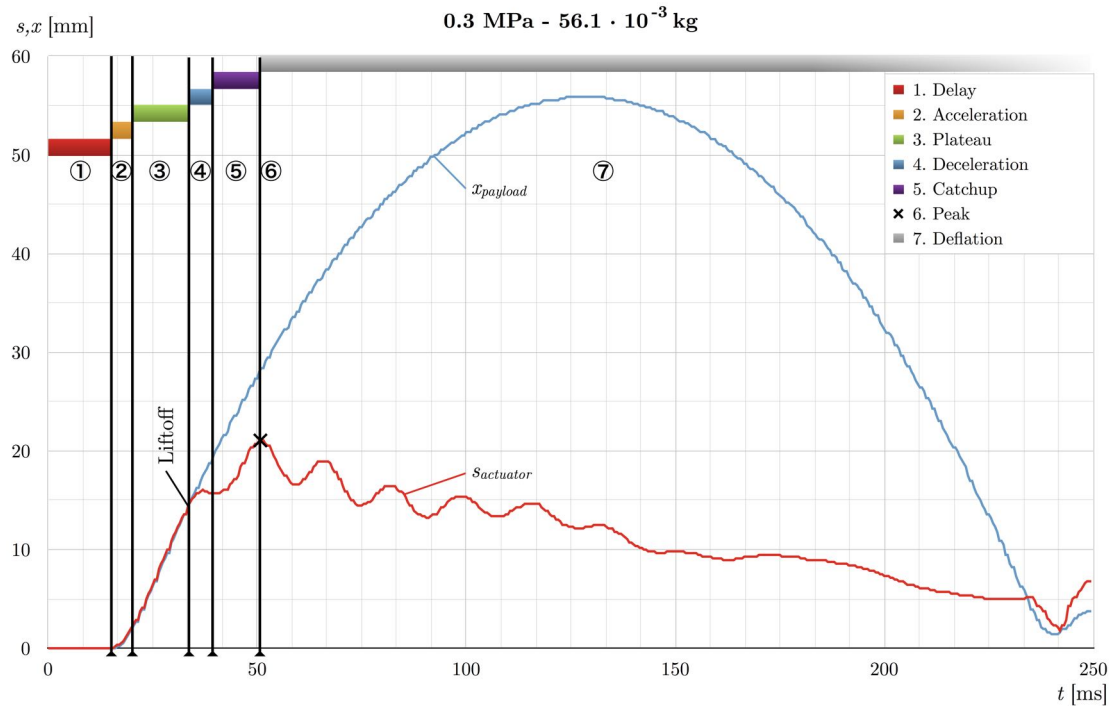


Figure 3.10: Single segment actuator - dynamic test detailed view

1. A **delay phase** in which no movement occurs. This is most likely caused by a lag in the mechanical actuation of the valve, as well as pressure buildup in the pipe running to the actuator. This value ranged from 15 to 30 ms, with higher pressures and lower payload masses having a smaller delay.
2. An **acceleration phase**. The actuator begins to inflate at what appears to be a quadratic rate (indicating a constant accelerating force) before reaching its maximum speed. Heavy payloads took up to 10 ms to reach their maximum speed, while this phase was barely discernible when no payload was applied.
3. A **plateau phase** in which the actuator extends at a constant rate, taking the payload with it.
4. A **deceleration phase**. Although the flow of air into the actuator continues, its expansion suddenly slows down, sometimes almost to a halt. Possible causes include a drop in pressure as the regulator adjusts for the change in flow, and a redistribution of the forces inside the actuator, e.g. an increasing radial expansion of the actuator's diameter. This slowdown causes the **liftoff** and initiates the free-fall phase of the payload (if present).
5. A **catchup phase** where the actuator regains the speed of the plateau phase.
6. The **peak** at or shortly after the moment the valve is closed again. It may be delayed slightly due to the actuator's own inertia as well as remaining pressure in the system.
7. The **deflation phase**. The valve's exhaust port is now open, allowing the air inside the actuator to escape back through its supply pipe. Because of the actuator's inertia and inherent elasticity, this causes a visible wobbling motion as it returns to its initial deflated state, following an approximately exponential path after the oscillations have subsided.

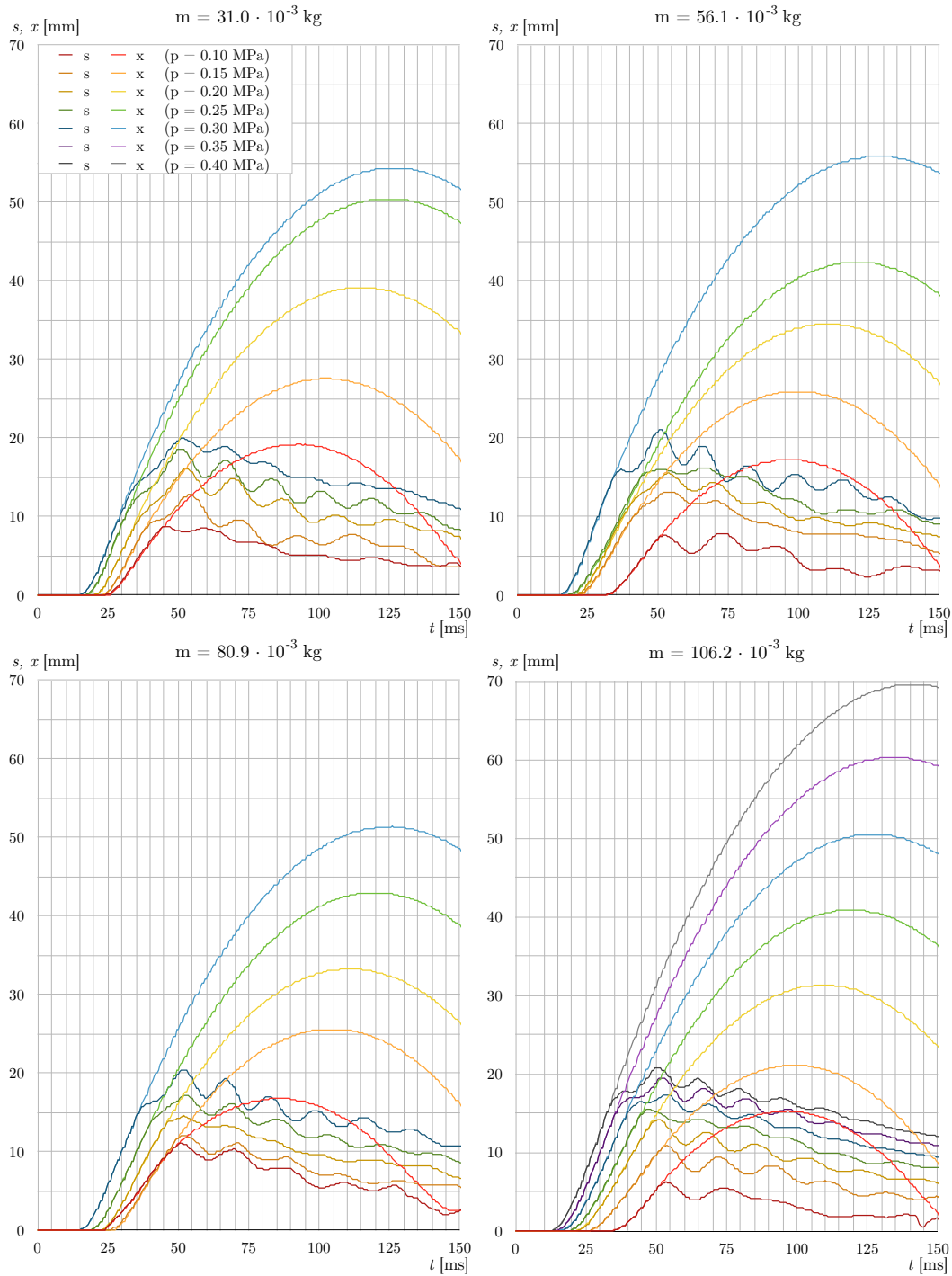


Figure 3.11: Single segment actuator - dynamic test overview

3.5.4 Test series IV: Multi-segment actuator dynamic test

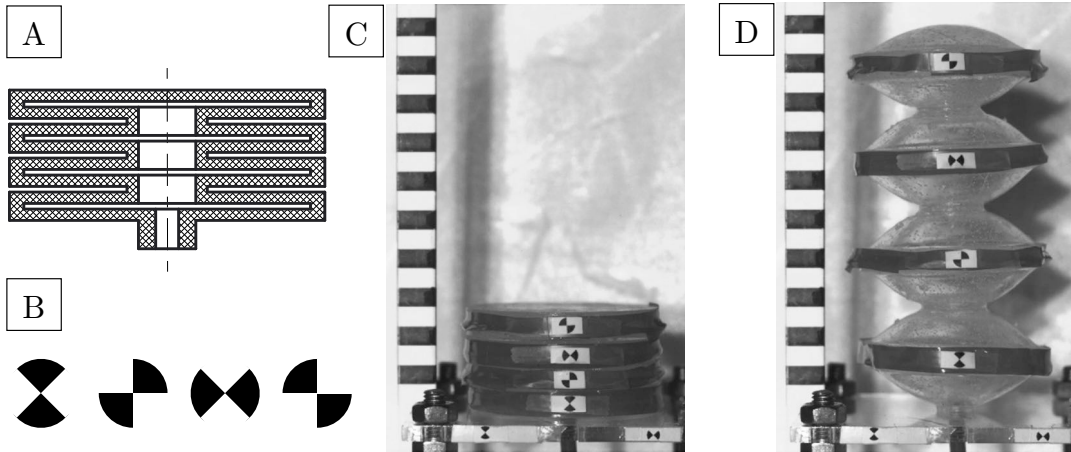


Figure 3.12: Multi-segment actuator - overview

An advanced version of the soft actuator was also constructed, consisting of four individual inflatable units joined along their central axes as presented in Figure 3.12A. The dynamic behavior of this Multi-segment actuator was evaluated using the same high speed camera. At the time of testing, more information was available on the robot platform's final dimensions, therefore a payload mass of 0.2 kg was launched to match each actuator's expected load in the final prototype. All tests used an actuation time of 50 ms.

Each segment was outfitted with one marker, each rotated by 45° for distinction as seen in Figure 3.12B. Since the manufactured actuator had a flat end on which the payload was placed (as opposed to the mounting knob in the single actuator tests), the markers were attached to the middle ring of each actuator using electrical tape, as it was one of the few adhesives found to work on the silicone rubber (Figure 3.12C/D). Because some markers are identical with the two calibration markers fixed on the platform, the software was adjusted to only scan a certain area of the image (defined beforehand) for the actuator segments, while the calibration focused on the lower edge of the image during the first frame only.

To be able to log the behavior of each one of N segments in an actuator, the measured position of each marker T_i had to be mapped to the actuator's actual expansion s_i through a simple transformation (see Figure 3.13). The model makes the assumption that each segment expands symmetrically around the marker, and this matches the observed behavior quite closely.

$$s_1 = 2 T_1 \quad (3.1)$$

$$s_i = 2 (T_i - \sum_{n=1}^{i-1} s_n) \quad \text{for } 2 \geq i \geq N \quad (3.2)$$

Figure 3.14 provides a compact overview of the three tests performed with a payload at varying pressures, while Figure 3.15 shows the different behaviors when firing the actuator with or without a payload. Each colored band represents the calculated expansion s_i of one segment over time, in the order blue (bottom segment), green, yellow and red (top segment). The crest of the colored graph therefore equates to the overall expansion s . The dark line in each band is the measured position of the respective marker T_i . It is not always in the center of the band as the segments occasionally tilted up and down while expanding, shifting the perceived location of the marker.

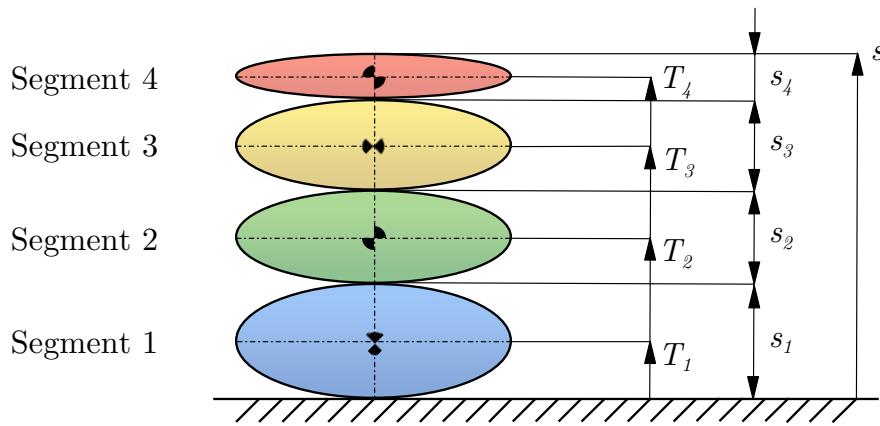


Figure 3.13: Multi-segment actuator - marker mapping

It can be observed that the individual segments do not expand uniformly upon opening the valve. When lifting a payload, the first (bottom) segment begins expanding, pushing the remaining uninflated segments up. It is then pushed back down by the second, third and fourth segments as they expand one after the other, inducing a 'wobbling' motion within the actuator. This movement results in a waste of energy which is not available for accelerating the payload upwards.

Interestingly, this behavior is inverted when no payload is placed on top of the actuator. In this case, the top segment is the first to expand, neatly followed by the subsequent segments with nearly no discernible 'wobble' up to the closing of the valve at $t = 50$ ms.

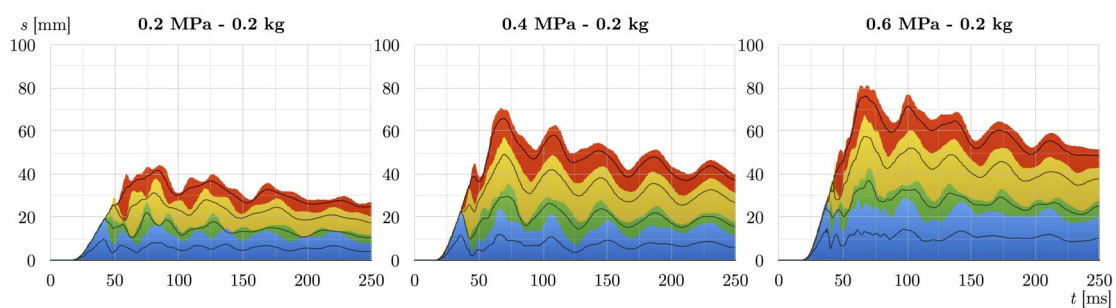


Figure 3.14: Multi-segment actuator - dynamic test overview

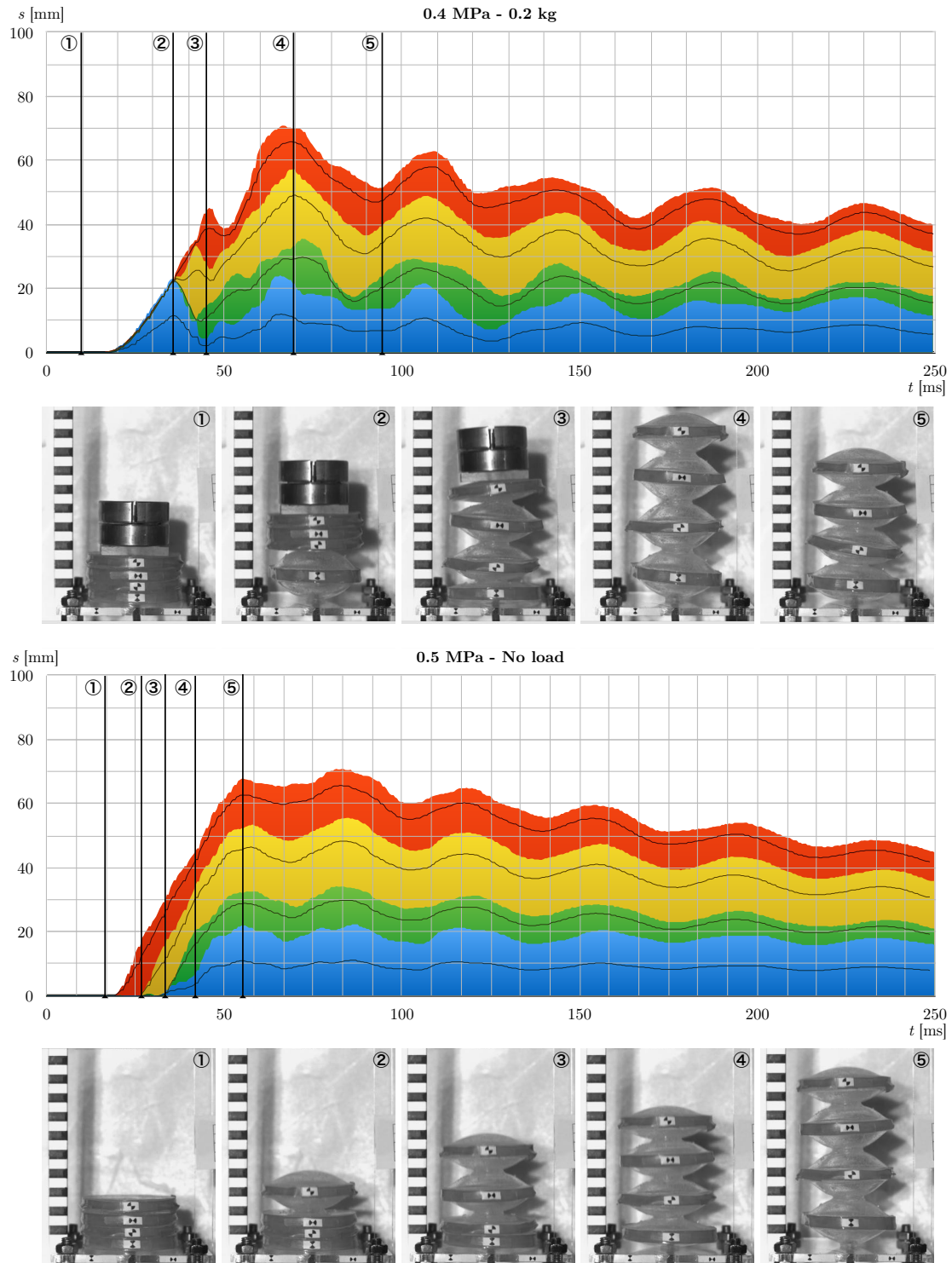


Figure 3.15: Multi-segment actuator - comparison of loaded and unloaded runs

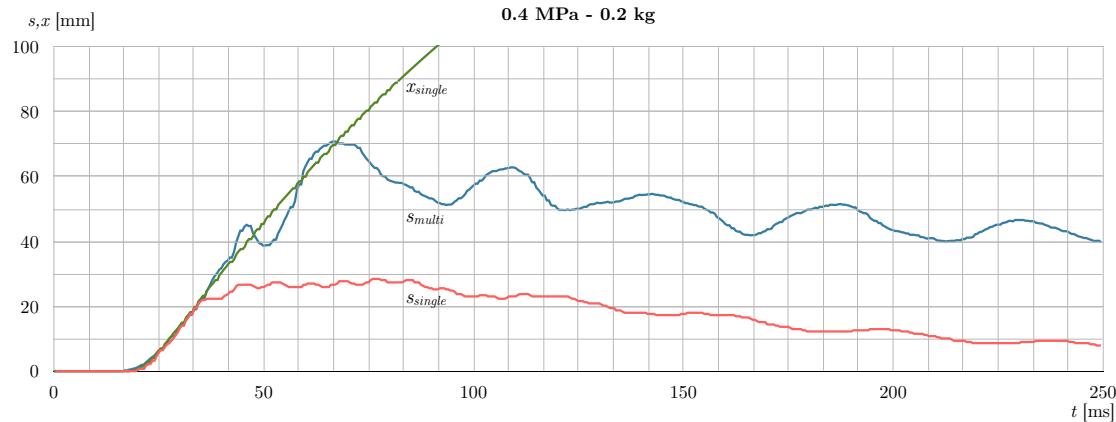


Figure 3.16: Comparison of single and Multi-segment actuators

When comparing the performance of the multi-segment actuator with its single-segment counterpart as in Figure 3.16 (both launching a payload of 0.2 kg with 0.4 MPa³) it becomes evident that there is no inherent advantage in using the more complicated multi-segment variant. The initial acceleration and plateau phases (as described in 3.5.3) are nearly identical and the terminal velocity of the payload at liftoff is virtually the same⁴. Larger diameter piping and a regulator allowing a higher airflow would probably be necessary to detect a difference in performance. Because of the difficulty in manufacturing a multi-segment actuator (requiring eight castings and seven seams for a four-segment actuator, each seam increasing the likelihood of a leak in the system) in addition to the difficulty in acquiring the aforementioned equipment for a higher airflow, the decision was taken to resort to single-segment actuators for the jumping platform described in the following chapters.

3.6 Summary

It was found that the soft pneumatic actuators used are a highly nonlinear system with many unknown characteristics and effects. This makes creating a detailed model of its behavior a very hard task, which is not the aim of this thesis. However, it was deemed necessary to gain a basic feeling and understanding of how the actuator would perform in the jumping platform proposed here, following the synthetic methodology of 'understanding by building' [54]. These tests allowed a basic confirmation that the proposed actuator design was viable for use in the intended configuration. Especially the finding that the achievable jumping height is not very strongly influenced by the weight (at least in the range the actuators were expected to perform for this projectw) gave confidence that the platform could be designed with more freedom, i.e. fewer restrictions when selecting suitable components, as weight optimization was deemed not a primary objective. It should be noted that different valves and regulators than employed here were used in the final design. Therefore, the performance of the robot cannot be quantitatively compared directly with the results from the actuators in the experiments described in this section; nevertheless the test results allow to see general trends in the actuator's behavior.

³The payload was not tracked in the multi-segment actuator test.

⁴The apparent 'bump' in s_{multi} at $t \approx 45$ s is likely due to a tilting of the actuator resulting in a marker detected higher than intended.

4 The Jumping Robot Platform

Upon having characterized and gained a feeling for the behavior of the silicone actuator, the next task was to develop, manufacture and assemble the mobile robot platform. To this end, suitable mechanical, electronic and pneumatic components had to be selected and procured. A detailed 3D CAD model was created in Pro/Engineer, and custom circuit boards developed using CADSoft EAGLE. Since a microcontroller was used on the robot to control all its functions, a firmware programm had to be written and a communication protocol was implemented to send commands to and receive data from the robot using a wireless link to a control station such as a computer.

4.1 Hardware description

Figures 4.1 and 4.2 show the finished jumping robot platform from various angles. The central piece of the robot's structure is a 5 mm thick, laser-cut, clear transparent PMMA¹ (acrylic) sheet. Its X-like shape fits in a 182x182 mm square and measures 235 mm along its diagonal axis, with 180 mm between diagonally opposing actuators. The height from the base of the (deflated) pneumatic actuators to the tip of the exhaust valve (the highest component) is 160 mm. It has mounting holes for all other components of the assembly. Figure 4.3 shows an exploded view of the main components; for clarity, the pneumatic pipes are not displayed.

Each one of the four legs holds a silicone actuator on the end. Further in are the solenoid valves controlling the actuators. Due to the pipe layout, the valve on one leg controls the actuator on the next leg, going clockwise when viewed from above. In the middle of the platform is the core electronics and air distribution module, shown in detail in Figure 4.4. It consists of various PCBs² and acrylic plates stacked on top of each other using standard hexagonal M3 standoffs. The lowest PCB is the power regulator unit, which takes the supply power (see 4.3.5) and generates the voltages required by the electronics and the solenoid valves. Above it sits the main control PCB, with the microcontroller and communications modules (see 4.3.1 and 4.3.2) plugged into dedicated sockets. From here, wires extend to the power regulator unit, the valves, and the Inertial Measurement Unit. This unit contains sensors to determine the orientation and movement of the platform. It is attached on the bottom of an acrylic sheet, directly above the main PCB. This sheet simultaneously acts as a separator between the electronics and the air distribution system. The topmost acrylic sheet holds the air pressure inlet pipe, a pressure regulator and the exhaust valve. It has 3 mm mounting holes placed in a 10x10 mm grid for attaching additional hardware, should it be required.

Two versions of the platform were used in the experiments. For most tests, both electrical power and air pressure were supplied by off-board sources, i.e. a standard benchtop power supply and the laboratory's air pressure supply. In the later phase, a fully wireless/pipelineless platform was developed. For this, rechargeable batteries were attached to the side of the center module's standoffs using cable zip ties. A small CO₂ canister was fitted underneath the center module and attached to the acrylic base plate in a similar fashion to act as the on-board pressure source, with an additional regulator located on the side opposite the battery pack. The photographs in Figures 4.1 and 4.2 show the robot with all on-board power sources attached.

The minimum working setup of the robot platform without on-board pressure supply and batteries weighs 0.720 kg. The pressure supply adds 0.273 kg, including 0.016 kg of CO₂ inside the tank. The two batteries add another 0.126 kg, resulting in a total weight of 1.12 kg for the fully wireless and pipelineless system (an increase of 55%).

¹PMMA: Poly(methyl methacrylate)

²PCB: Printed Circuit Board

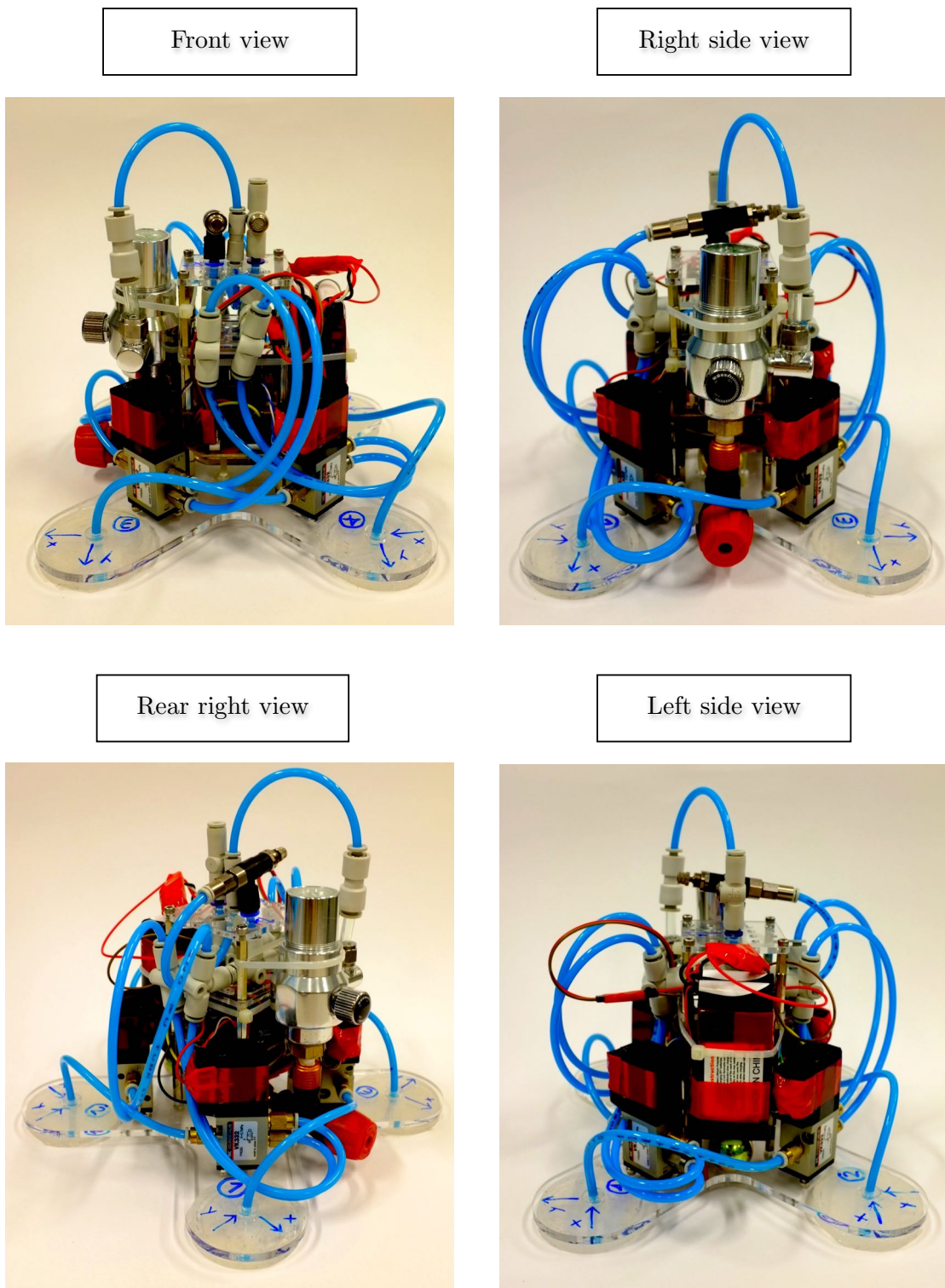


Figure 4.1: Robot platform - photos (1)

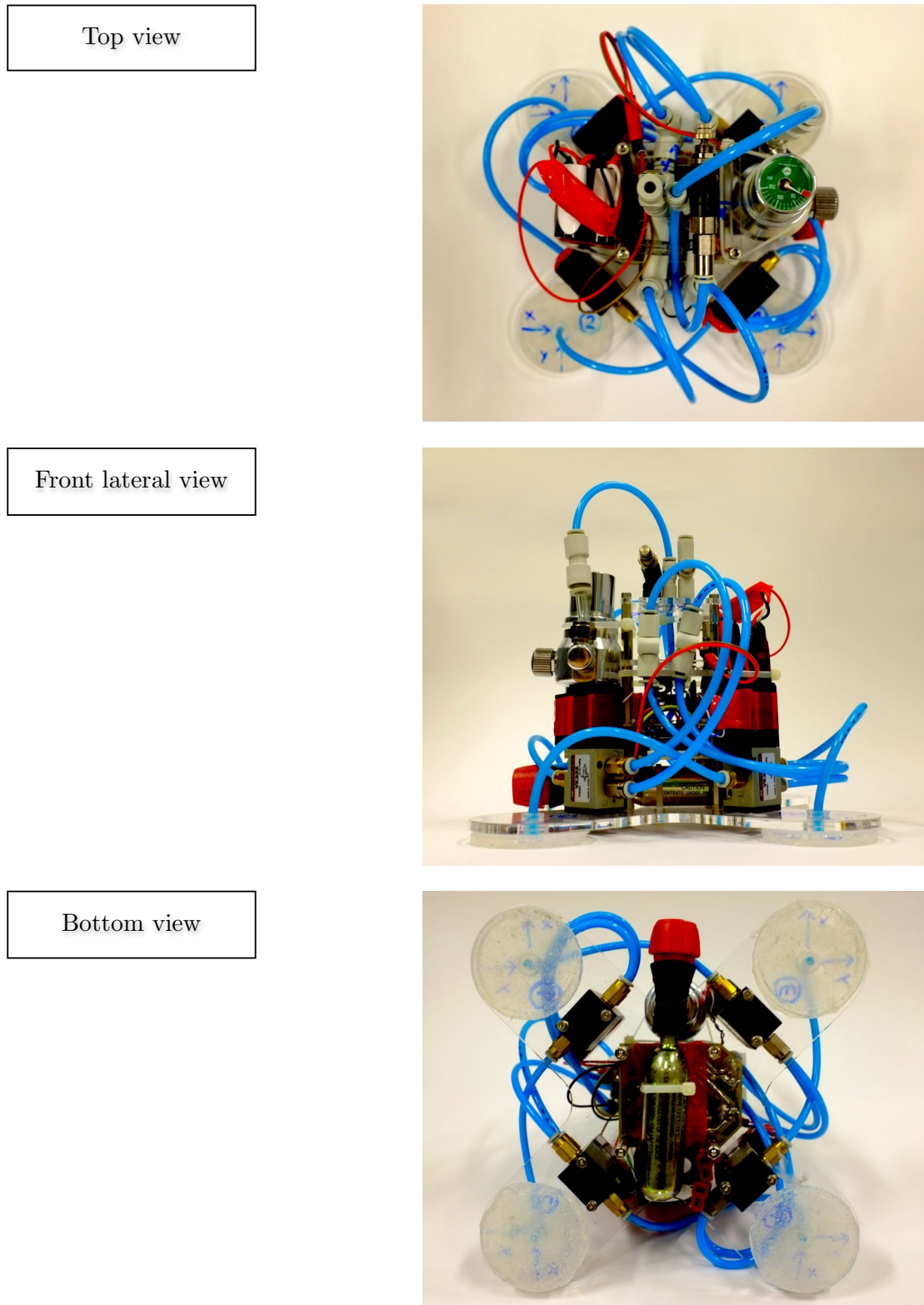


Figure 4.2: Robot platform - photos (2)

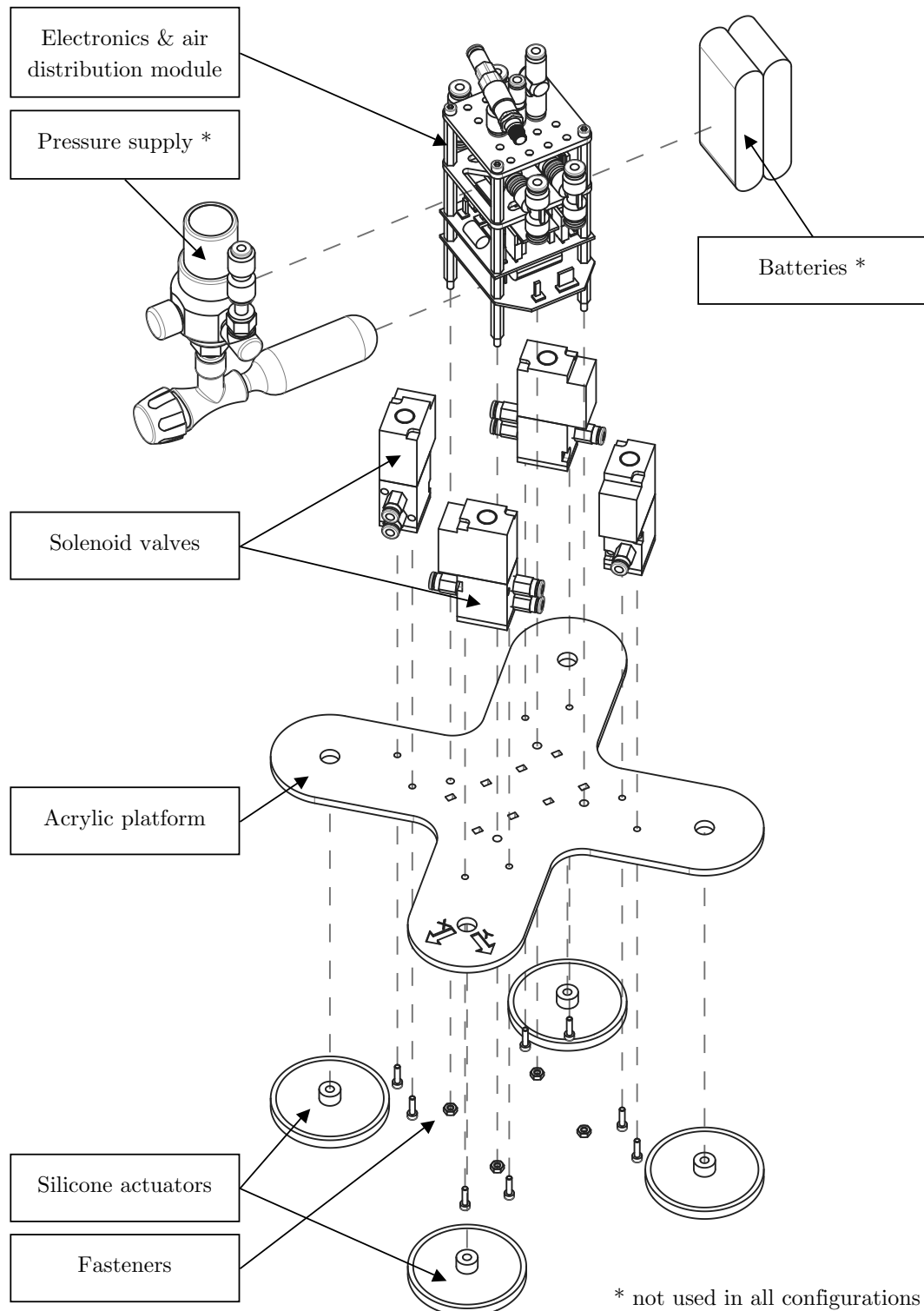


Figure 4.3: Robot platform - main components (exploded view)

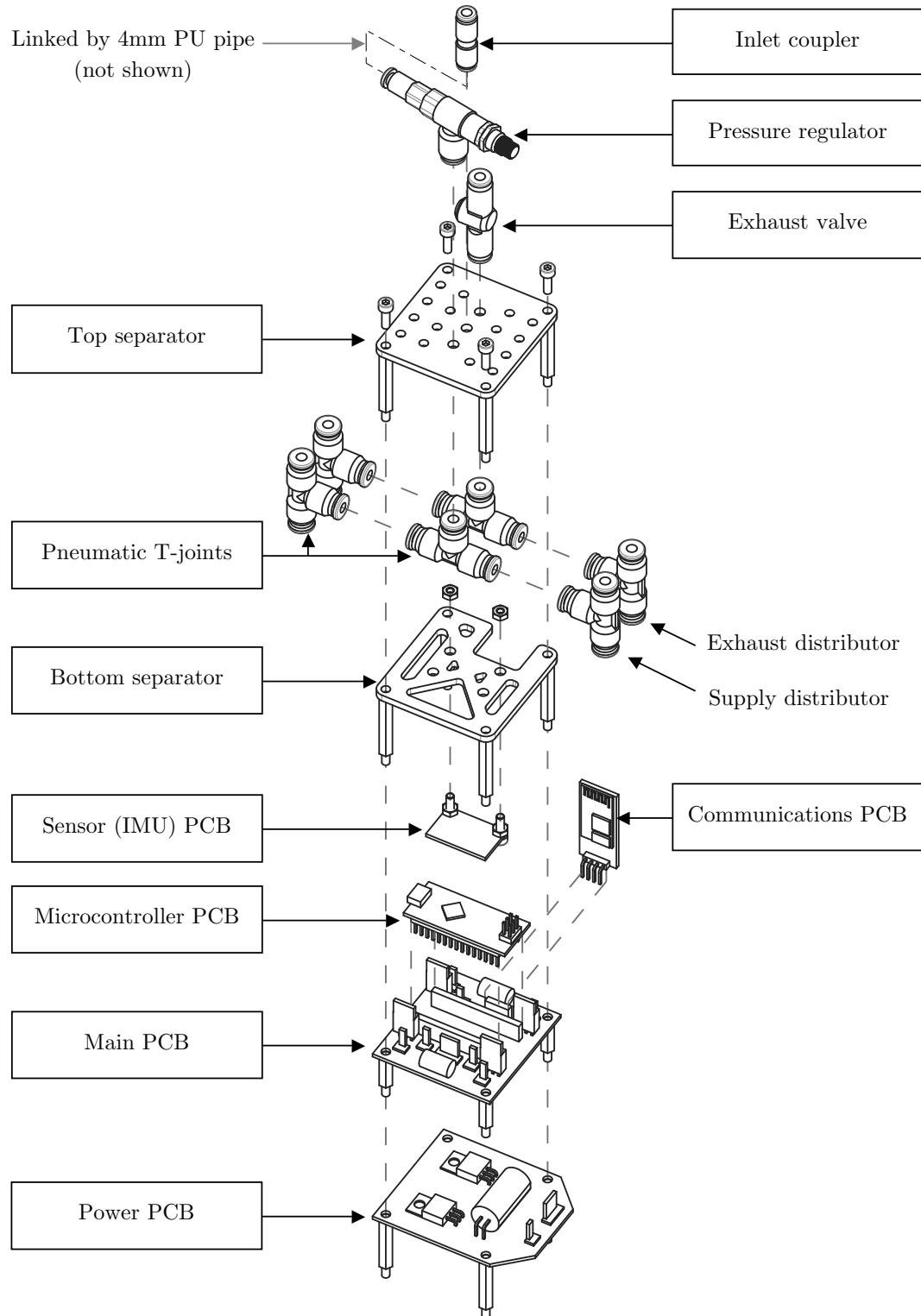


Figure 4.4: Core electronics and air distribution module (exploded view)

4.2 Pneumatic system

4.2.1 Overview

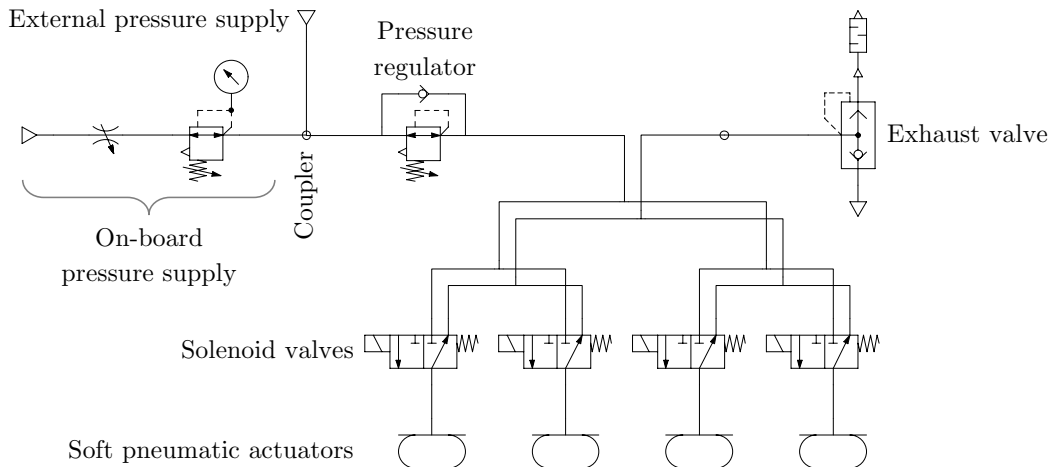


Figure 4.5: Pneumatic diagram of the robot platform

Figure 4.5 shows the pneumatic diagram of the robot platform. Datasheet excerpts for all pneumatic components described here can be found in the appendix. Standard 4 mm flexible Polyurethane (PU) tubing and One Touch fittings of type SMC KQ2 were used throughout the system. The air from the pressure source (either an external source or the on-board supply) is first routed through an easily detachable coupler (useful e.g. when transporting the robot), and from there into a miniature regulator SMC ARJ1020F-M5-04. The regulator generates a manually adjustable output pressure of 0.1 to 0.6 MPa, while the input pressure should not exceed 0.8 MPa.

The regulator's output is routed to a series of T-joints in a symmetrical arrangement, to distribute the air among the four legs. Each output of the air distributor is attached to one solenoid valve's input port. The valve is a SMC VK332-6DS-M5-Q 3-port directly operated solenoid valve. The output port is then connected to the valve's corresponding actuator. The platform's mounting hole was designed with a diameter of 9 mm, as opposed to the silicone actuator's neck with 10 mm outer diameter. By squeezing the neck through the hole and then inserting the pipe, the actuator is secured in place and the inlet tightly sealed. No leakage was detected at this point in any of the experiments. Care was taken to achieve the same pipe length on all sections for all four legs to avoid irregularities caused by a delayed pressure change in one actuator.

4.2.2 Exhaust port

The pipes from the exhaust ports for all four valves are linked together (analogous to the supply pipes). This allows to conduct experiments by varying the deflation rate of the actuators using only one flow regulator on the common exhaust. To this end, a SMC AQ240F-04-00 quick exhaust valve with silencer was mounted backwards onto the platform's exhaust port when necessary. The pressure in the actuators after the solenoid valves close then discharge through this relief mechanism at a slower rate than with an open exhaust. However, the valve was not used for the majority of the experiments except the one described in 5.2.2.

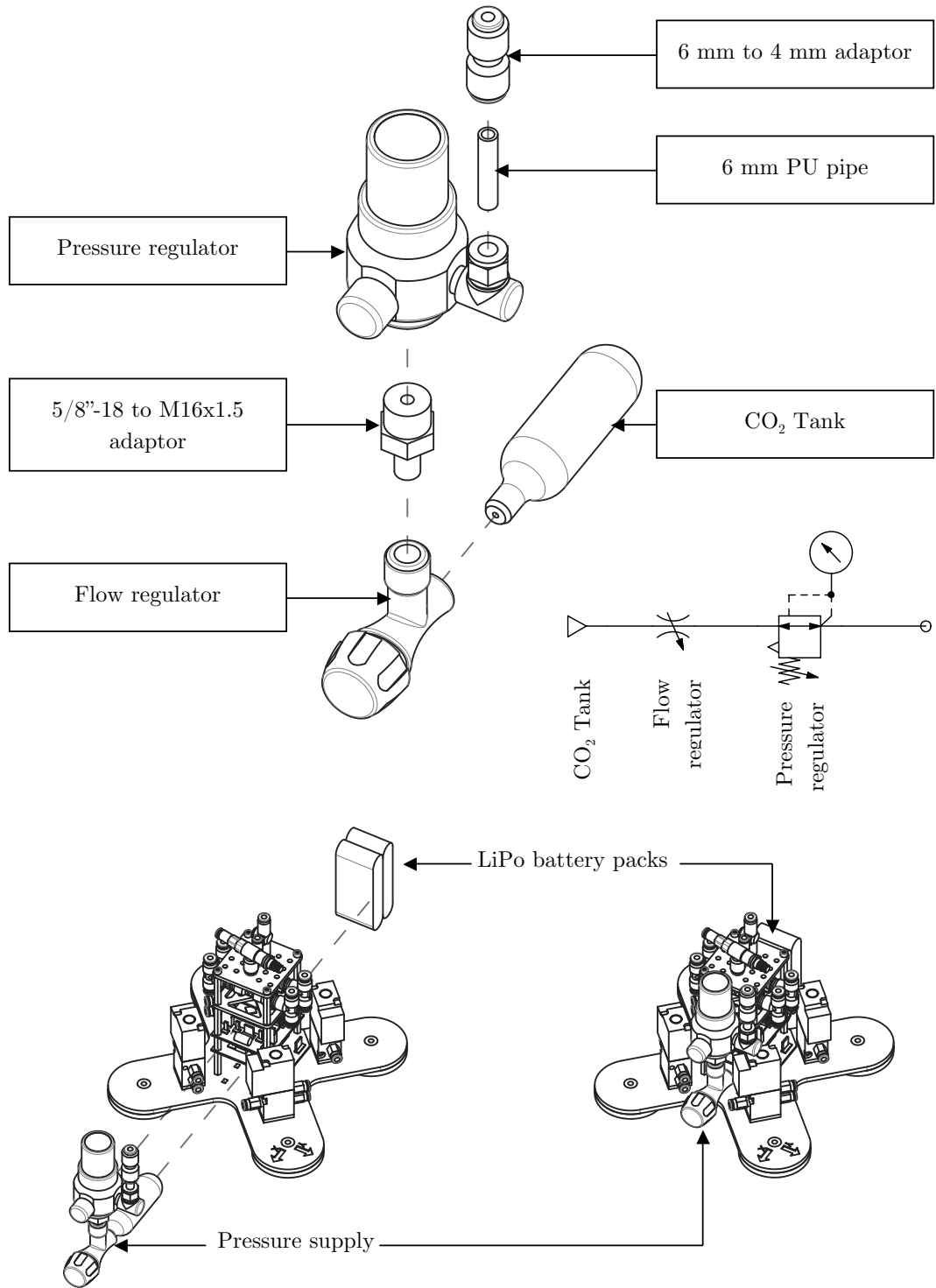


Figure 4.6: On-board pressure supply (exploded view)

4.2.3 On-board pressure supply

For the experiments with an on-board pressure supply (see 5.3), an off-the-shelf combination of a 16 gr threaded CO₂ gas cylinder and flow regulator (intended for inflating bicycle tires) was used. However, the approx. 6 MPa nominal pressure of the cylinder [55]³ far exceeds the platform's system's maximum rating, and the included regulator only allows control over the flow rate, but not over the delivered pressure. To compensate, an additional A-167-G regulator (used with the larger 88 gr CO₂ tanks in aquarium setups) was found as a suitable pressure converter to deliver the required 0.7 MPa for the robot's system. A custom adaptor from the imperial 5/8"-18 thread of the first and the M16x1.5 thread of the second regulator had to be machined. The final piece used is a converter from a 6 mm pipe from the A-167-G regulator to the 4 mm system used on the platform. The setup is shown in Figure 4.6.

4.3 Electronic system

The architecture of the robot's control electronics is shown in Figure 4.7. A detailed schematic of the main PCB is provided in Figure 4.8. Datasheets of the components are listed in the appendix.

The core of the system is the main PCB. This board acts as a hub, featuring connectors and sockets for all other parts of the system:

1. A central socket⁴ for the Arduino Nano microcontroller board (30 pins). See 4.3.1
2. A socket for the Bluetooth communications module (4 pins). See 4.3.2.
3. A header⁵ for the Inertial Measurement Unit (4 pins). See 4.3.3.
4. Four headers and a few discrete components for the solenoid valves controlling the actuators (4x2 pins). See 4.3.4.
5. A header for a trigger signal (2 pins). This was configured as an output to trigger the recording of the high-speed camera by switching from LOW to HIGH upon starting the jump. It can also be configured as an input to trigger an action of the robot based on an external signal.
6. A header for the 12 VDC supply to drive the solenoids (2 pins). See 4.3.5.
7. A header for the 5 VDC supply for the electronics (2 pins). This header was left unused as the 5 VDC were later supplied through the Arduino's built-in Micro-USB port into the system.

In addition, it holds some decoupling capacitors to smooth the 5 VDC and 3.3 VDC supply rails.

4.3.1 Microcontroller board

An Arduino Nano board [56] was chosen to control the platform. It is built around an Atmel ATmega328P microcontroller running at 16 MHz. It contains all the necessary I/O⁶ pins to control the solenoids, the sensors and the communications link. The Arduino platform was chosen for its ease of use and low cost, and for the fact that many useful libraries are provided under an open source license to easily interface the board to other modules without having to build everything from the ground up, greatly speeding up the development and allowing to test many prototypes in a short time.

³No exact data was available for the tank used; the number is an estimate from the PV diagram in the source.

⁴A socket is defined in this writing as a female connector into which another component's pins are inserted directly.

⁵A header is a male connector that receives a matching cable for indirectly attaching another component.

⁶I/O: Input/Output

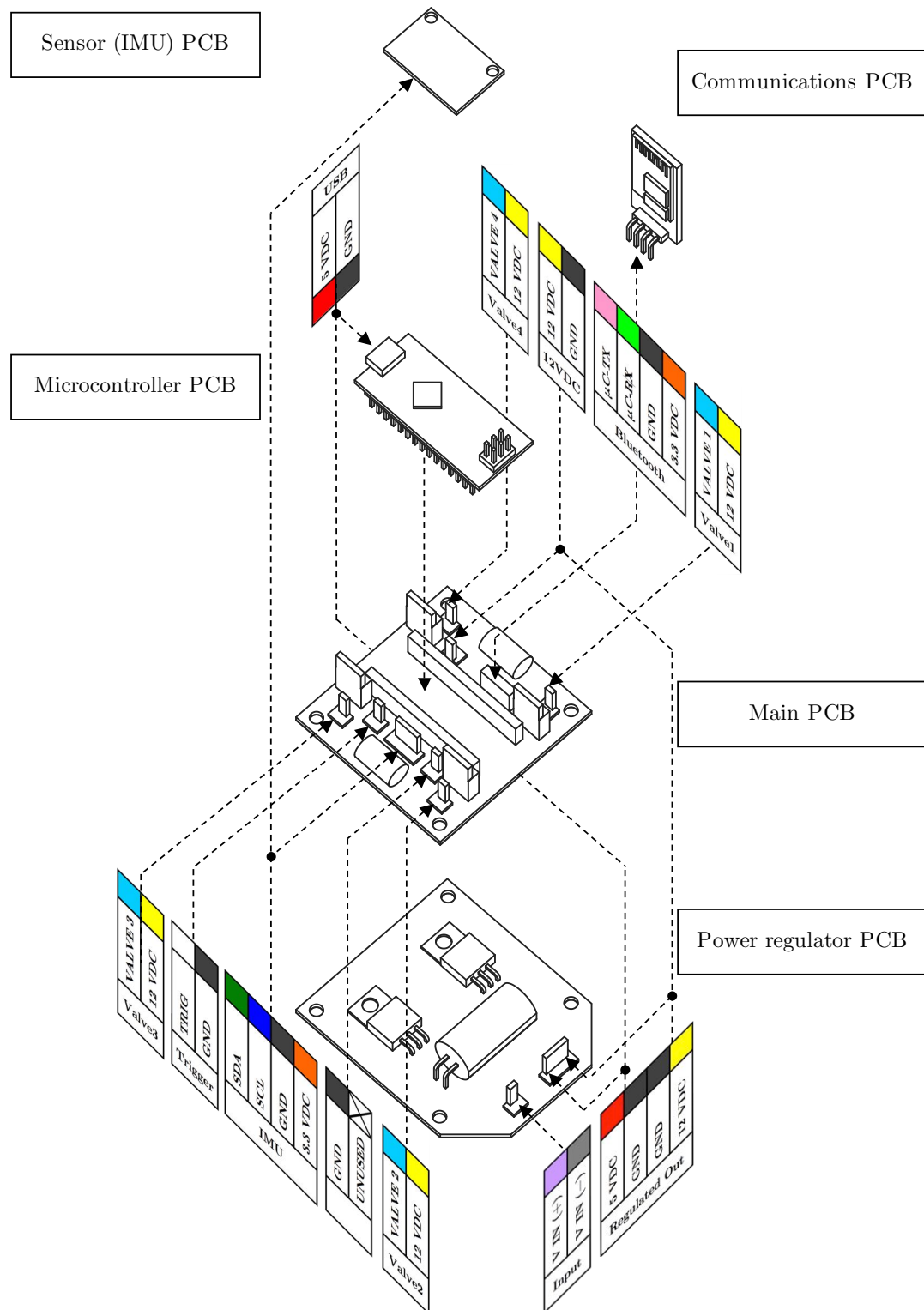


Figure 4.7: Electronics module (exploded view)

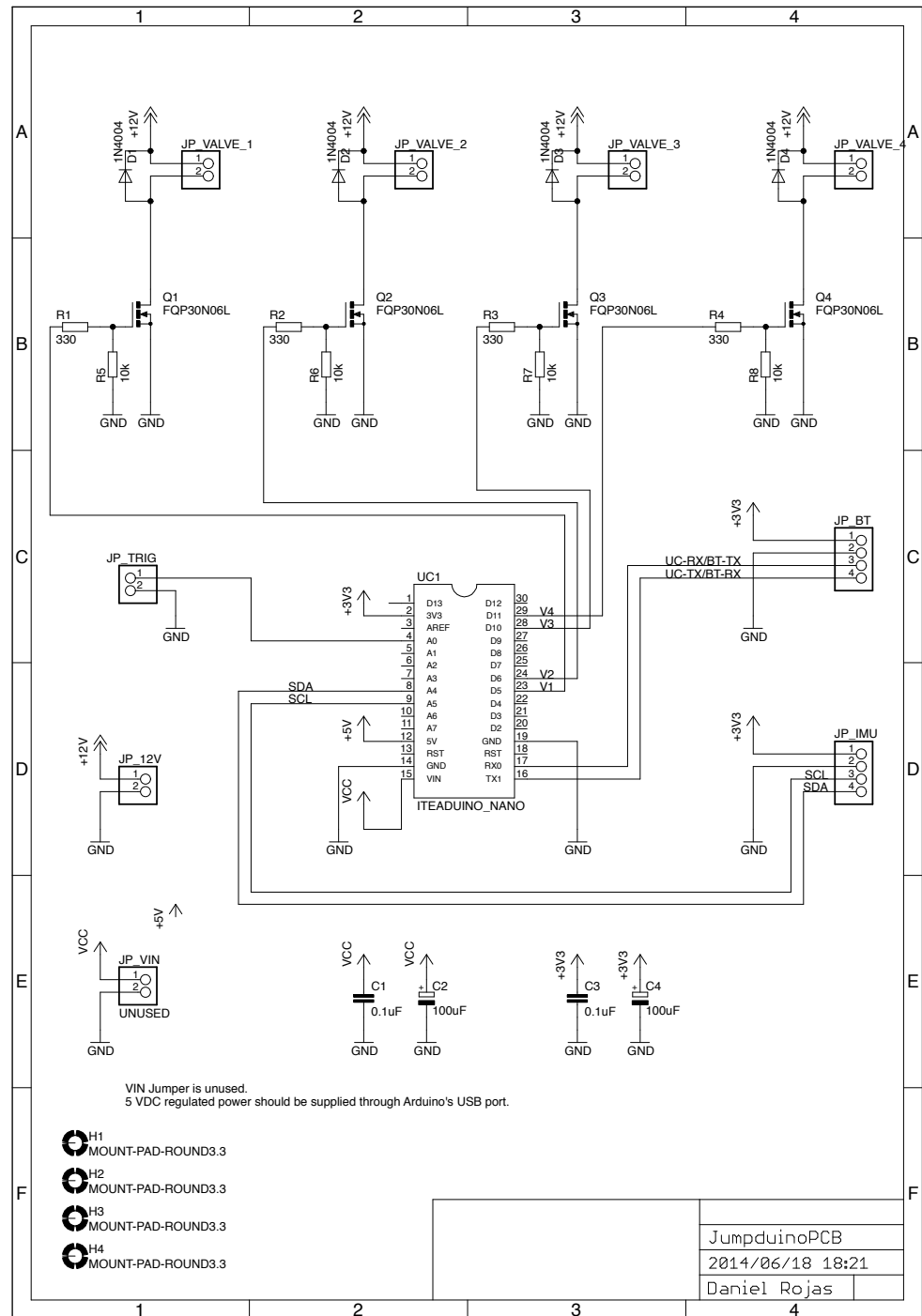


Figure 4.8: Main control PCB (Schematic)

4.3.2 Communications

It is possible to communicate with the robot from a computer or other device thanks to the on-board Bluetooth serial communications module. It is based on the CSR BC417 chipset and allows bidirectional communication with the host at 115 200 bps through the Arduino's UART⁷ pins. It receives commands to control the solenoid valves or to adjust parameters prior to a jump, and returns values from the IMU and information about the robot's status upon request from the host. The available commands are described in 4.4.

4.3.3 Inertial Measurement Unit

The GY-80 is a 9 DOF⁸ Measurement Unit (IMU) comprising an accelerometer, a gyroscope and a magnetometer/compass unit in addition to barometer and temperature sensors, all on one compact PCB. Supply voltages of 3.3 VDC or 5 VDC are supported; for the robot platform, 3.3 VDC were used. The Arduino interfaces with the individual components using the I²C protocol [57]. The individual components' I²C addresses can be gathered from Table 4.3.3.

Model No.	Sensor type	Manufacturer	I ² C Address
ADXL345	3 DOF Accelerometer	Analog Devices	0x69
L3G4200D	3 DOF Gyroscope	ST Microelectronics	0x53
MC5883L	3 DOF Magnetometer	Honeywell	0x1E
BMP085	Thermometer/Barometer	Bosch	0x77

Table 4.1: IMU sensors and I²C addresses

4.3.4 Solenoid drivers

One FQP30N06L MOSFET driver was used to control each solenoid valve. They were chosen early in the design process for their availability in the lab, as well as their ability to handle large currents (up to 32 A) at high voltages (60 V), as the valves' power requirements were not yet known at the time of the electronic design. Flyback diodes of type 1N4004 were installed for each valve to protect the circuit against sudden voltage spikes induced by the solenoid when power is removed.

The MOSFETs were specifically attached to the pins on the Arduino which support PWM⁹. While only on/off control has been used so far, these pins would allow a precise control over the airflow into the actuators, should proportional flow control valves be used later on.

4.3.5 Power supply

During the breadboard stage, power to the circuit was provided through a regulated benchtop power supply capable of providing the 5 VDC required by the Arduino (which in turn produced a 3.3 VDC supply for the IMU and Bluetooth modules) and the 12 or 24 VDC for the solenoid valves, depending on the type being used at the time.

For the mobile platform, a dedicated PCB (see Figure 4.9) was developed to provide the necessary voltages from a single supply. When supplied with a voltage of 14.6 VDC or higher, two regulators of the 78XX family generate the required 5 VDC (7805) and 12 VDC (7812). Since firing all four valves at once draws a significant amount of power, a large 1000 μ F decoupling capacitor was installed on the 12 VDC rail. A four pin header allows cables to connect the power regulator circuit to the main PCB.

For the wireless platform, two RFI 20C LiPo¹⁰ rechargeable batteries providing 7.4 VDC and 1000 mAh each were connected in series to generate the 14.8 VDC input voltage for the circuit. Battery life tests

⁷UART: Universal asynchronous receiver/transmitter

⁸DOF: Degree of Freedom Inertial

⁹PWM: Pulse Width Modulation

¹⁰LiPo: Lithium Polymer

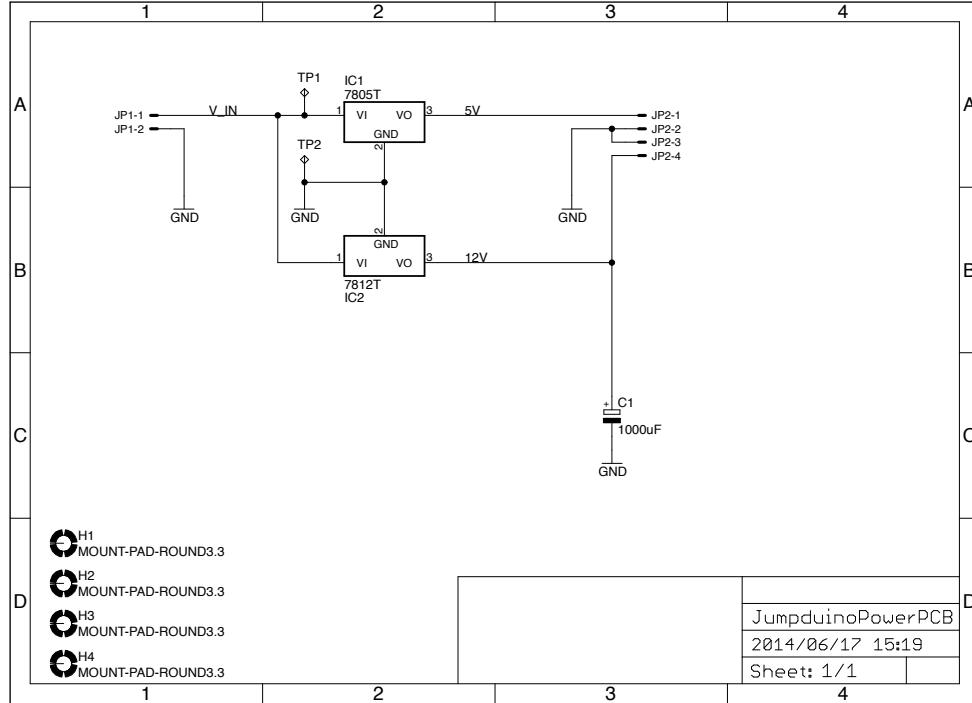


Figure 4.9: Power supply PCB (Schematic)

were not carried out and power saving techniques were not used in the prototype presented here, as it was not the focus of the project and most experiments were performed with an off-board power source.

In order to take advantage of the Arduino's built-in 3.3 VDC regulator to power the IMU and Bluetooth modules, the 5 VDC supply from the power regulator circuit was routed to the Arduino's USB connector through a custom adaptor¹¹. For debugging purposes, the Arduino can also receive power via USB from a host PC attached directly, while the valves still receive the required 12 VDC from the power regulator circuit and a dedicated supply.

4.4 Communication protocol

A communication protocol was designed to send commands between the robot platform and a host device (usually a PC) via a serial Bluetooth link. The robot only sends commands in response to a request by the host. The highest available speed of 115 200 bps was used to allow a higher throughput of information.

Commands from the host take the following format:

```
X a b c d e f g h
```

with X being the command name and a-h being up to eight parameters, separated by a single whitespace each. X can be any single alphanumeric or symbol ASCII character (e.g. 'J' or '!'). a-h are ASCII strings of arbitrary length representing integers (e.g. '0' or '123'). A command is terminated using the 'new line' character (ASCII 10).

¹¹Due to the design of the Arduino PCB, its 3.3 VDC regulator can only be powered directly from the USB connector, not from a supply voltage connected to the VIN pin.

A response from the robot can have various forms. For instantaneous commands (such as adjusting the robots parameters), the response format is:

```
X      OK    1234
```

The command name is repeated, followed by an OK flag and the elapsed time since program start (in ms). Responses are tab-separated for easy importing into spreadsheets.

A command that takes a certain time to execute (e.g. performing a jump) is immediately acknowledged upon receiving with a 'GO' response and followed up with the same 'OK' message upon completion:

```
X      GO    1234
X      OK    5678
```

Commands that request additional data from the platform (like acceleration data) may send other responses (tab-separated), but they will always be preceded by a 'GO' message and terminated with an 'OK' to signal completion.

A sample communications log might look like the following. Input from the host is marked with '`->`', output from the platform with '`<-`'.

Send a ping to the robot

```
->      !
<-      !          OK        5000
```

*Set front valves to open for 0 ms < t < 50 ms
and rear valves to open for 50 ms < t < 100 ms*

```
->      d  0  0  50  50  50  50  100  100
<-      d          OK        6000
```

Perform a jump and log the linear acceleration of all axes for 500 ms at 5 ms intervals

```
->      J  500  5  1  1  1  0  0  0
<-      J          GO        7000
<-      L      t      Ax      Ay      Az
<-      L      5000    40      -2      1001
<-      L      10000   22      4       998
<-      L      15000   40      -2      1000
<-      L      20000   36      -1      1007
...
<-      L      500000  99      -10     1010
<-      J          OK        7500
```

Cmd	Par.	Description	Possible values
!		Ping, returns OK	
j		Execute jump Parameters same as D command (to set jump delays)	all 0 = no change
J		Execute logged jump Parameters same as L command (logging settings)	
X,x		Reset jump	
D		Set leg delays (in ms) <i>flo</i> Front left leg open <i>fro</i> Front right leg open <i>rlo</i> Rear left leg open <i>rro</i> Rear right leg open <i>flc</i> Front left leg close <i>frc</i> Front right leg close <i>rlc</i> Rear left leg close <i>rrc</i> Rear right leg close	opening values default to 0 ms closing values default to 50 ms after last opening
d	c	Set leg delays quickly All legs close (All legs open at 0 ms)	
L	t i ax ay az rx ry rz	Start logging acceleration Logging time in ms Output interval in ms Output X axis acceleration? Output Y axis acceleration? Output Z axis acceleration? Output X axis angular velocity? Output Y axis angular velocity? Output Z axis angular velocity? (displays all if ax=ay=az=rx=ry=rz=0) (Units of response: μ s; g \cdot 10 $^{-3}$; $^{\circ}$ /s)	0 for continuous logging. 0 for default (100ms) 0/1 0/1 0/1 0/1 0/1 0/1 0/1
I		Stop logging acceleration	
T		Perform training jump in set heading	
t		Reset all training data	
H	dir	Set training heading Direction	0 = front (Y+) 1 = back (Y-) 2 = right (X+) 3 = left (X-)
M		Output current magnetic heading (0 - 359 $^{\circ}$)	
V	<i>fl</i> <i>fr</i> <i>rl</i> <i>rr</i> v	Set valve states Front left leg Front right leg Rear left leg Rear right leg Toggle all valve states	0/1 0/1 0/1 0/1 0/1

Table 4.2: The command protocol: available commands and parameters

5 Experimental Evaluation

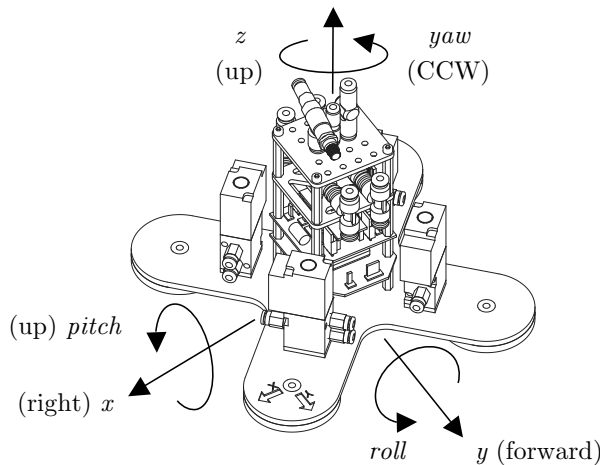


Figure 5.1: Axis and sign convention for the robot platform

Figure 5.1 shows the axis and sign convention used for the robot platform in all experiments in this section. y is defined as the forward-facing axis, while x points right with pitch becoming positive as the front of the robot points up, and z is the upwards axis, defining positive yaw as a counterclockwise rotation of the platform on the horizontal xy plane as viewed from the top. The roll axis was not used in any of the experiments.

5.1 Vertical jumping

Based on the findings described in 3.5, the actuation time of the valves was set to 50 ms for all tests, to allow the actuators to expand up to their plateau phase (3.5.3, phase 3) and guarantee the longest possible acceleration phase, while preventing an overexpansion that could result in the rupture of the actuator's material. The pressure was set to 0.5 MPa to determine the maximum achievable jumping height if all actuators were fired at the same time. The jump was measured using the same high speed camera as in 3.5. The jumping height was manually determined by measuring the location of the acrylic platform's center before the jump and during its apex, taking the difference and scaling it appropriately.

The test jumps averaged a height of 95 mm, with variations of approx. ± 5 mm over the five measured jumps. Although this more or less matches the predictions made by the experiments from 3.5 (which would have yielded around 88 mm assuming an average load of $\frac{1}{4}m_{robot} = 0.180$ kg per leg at 0.5 MPa), it is not enough height to be able to tackle obstacles such as stair steps, which usually start at 210 to 230 mm [58].

Quite possibly, performance is stifled because of insufficient air flow into the actuators. The combination of the pressure regulator, the 4 mm pipes connecting the components and the multiple T-joints places limits on the amount of air that enters the actuators during the acceleration period, with one component possibly acting as a critical 'bottleneck'. Experiments that worked well using only one actuator encounter problems once four legs have to be powered at the same time. As noted before, the comparison between the robot's jumping performance and the tests conducted with a single actuator should not be

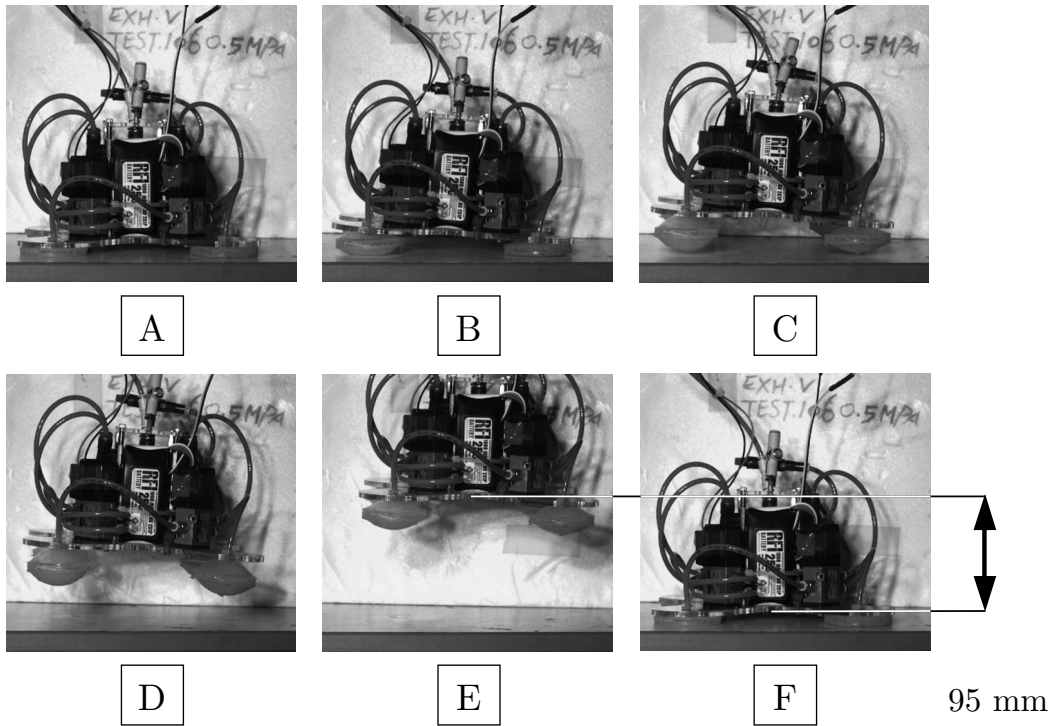


Figure 5.2: Vertical jumping - photo sequence

taken as an absolute measure, as different valves and slightly improved actuators were used in the final prototype. A detailed examination of the fluid dynamic and rheological effects inside the system was not performed, as key parameters of some components were unknown at the time of writing and time for systematic testing was limited. This topic is due for further investigation. Nevertheless, some basic studies on the general behavior of the platform are made possible this way.

5.2 Directional jumping

5.2.1 Experiment description

For the purpose of locomotion, an issue of prime importance is evaluating the performance and control of directional jumps. With the platform presented in this writing, the only mechanism available to generate an acceleration along the horizontal x - y -plane is a combination of different timing patterns for the firing of the solenoid valves and the effects of friction between the silicone actuators and the floor beneath the robot. The concept is illustrated in Figure 5.3.

By initially inflating the rear legs (defined as the actuators opposite the direction of the intended heading, from the platform's center) first, the entire rear section of the robot is pushed upwards into the air while the front legs are still inactive and on the ground, causing the robot to rotate along its sideways axis (achieving negative pitch when described in roll-pitch-yaw coordinates). A subsequent inflation of the front legs (now tilted relative to the ground) would yield a force separating into a constituent normal to the ground, reversing the pitching motion of the platform and propelling it further into the air, and a tangential force (caused by friction) effectively pushing the entire robot forward before lifting off. Depending on the parameters of the experiment, the platform may or may not reach a horizontal position (pitch = 0) in the air before touching down again.

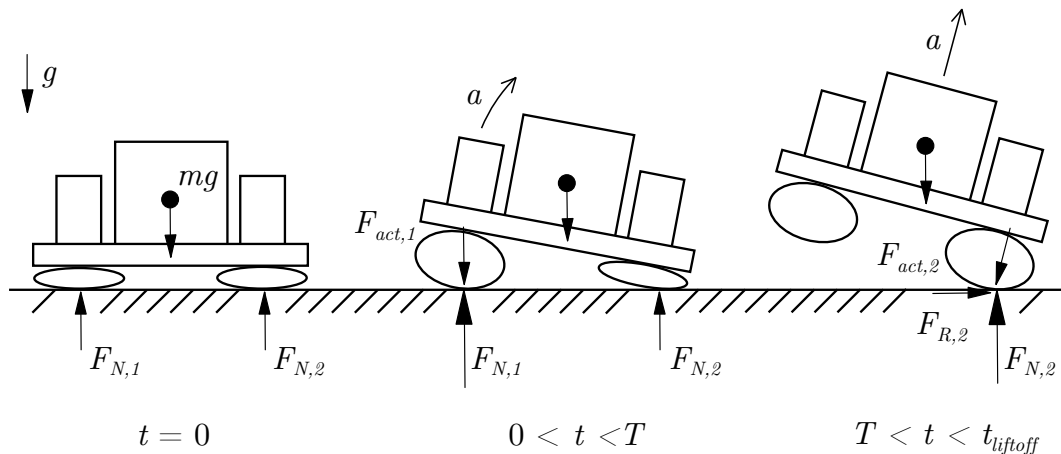


Figure 5.3: Directional jumping - concept

In order to find timing patterns that would maximize the distance traveled after a jump, a series of tests was performed. The delay in activation between the front and rear legs' solenoids was incrementally adjusted for each test series from 10 ms to 100 ms in 10 ms increments. For a determined timing pattern, the robot performed ten jumps one after another, with sufficient time between jumps to allow the system to stabilize (0.5 s). Afterwards, the platform's position was measured relative to the starting point. The experiment was repeated five times for the same parameters and the results averaged. The entire experiment was run four times, one in each main direction of the robot, to find and compensate for differences caused by an uneven weight distribution and possible performance differences between the actuators. The jumping commands therefore took one of the following forms (depending on the direction of the jump), with T as the delay between rear and front leg actuation.

j 0 0 T T 50 50 T+50 T+50	(Y+)
j T T 0 0 T+50 T+50 50 50	(Y-)
j T 0 T 0 T+50 50 T+50 50	(X+)
j 0 T 0 T 50 T+50 50 T+50	(X-)

These experiments were conducted with off-board power sources. The harness with the air pipe and power cables was kept suspended above the jumping platform, hanging from a line held taut along the desired heading and able to move with the robot with little resistance, so as not to affect the jumping performance.

In preliminary tests, an operating pressure of 0.2 MPa was selected for this test, as higher pressures often resulted in the robot behaving uncontrollably and erratically (see 5.2.2). The activation time for each solenoid valve was kept constant at 50 ms, independent of the delay between front and rear actuators. The substrate was the PVC-like laboratory floor, cleaned beforehand to reduce the influence of dust and dirt. The platform's exhaust port was kept open with no exhaust valve attached (see also the following section 5.2.2).

5.2.2 Higher pressure and exhaust tests

When trying the same experiment with pressures of ≥ 0.4 MPa, the back of the robot accelerated so quickly that it flipped over. It was not possible to find a suitable timing pattern to achieve a controlled jump; small delays between rear and front legs resulted in essentially vertical jumps upwards, while larger ones immediately lead to exaggerated rotation. It is believed that at these pressures, some interplay

between the actuators occurs, preventing the front legs from inflating and instead injecting more air into the rear ones. The reasons are still unknown as of this writing.

Some preliminary experiments were conducted by attaching an exhaust valve to the common exhaust port of the actuators as described in 4.2.2. Due to the slower deflation rate, after executing a jump more air remained inside the actuators at touchdown. The dampening effect of the escaping air resulted in a better shock absorption for the platform. However, this caused the platform to bounce back up, sometimes multiple times, and usually resulted in degraded performance with respect to jumping distance and accuracy. Since on occasion the front of the robot is facing down before touchdown, the entire platform bounces back in the direction opposite to the desired heading. If a yawing motion occurs, its effect on the robot's rotation is worsened due to the rebound. For this reason, the experiments in the previous and the following sections were all carried out with the exhaust port open to allow for quick deflation.

5.2.3 Results

From the measured (cartesian) position of the robot, its traveled distance (projected onto the intended heading's axis), its deviation from a straight trajectory and its rotation (yaw angle) were calculated and plotted as seen in Figure 5.4 (top). Each color represents the test series in a certain direction. The top chart shows the results of every single run, while the bottom one shows only the average over the five runs performed for a specific configuration. The x-axis displays the actuation delay between the rear and front legs, in ms. Figure 5.4 (bottom) visualizes the data in an intuitive way. The arrow indicates the final position of the platform after each run; its color reveals the timing pattern employed.

By analyzing the effective traveled distance, it becomes apparent that there is an optimal set of timing parameters where the distance is maximal. Short delays between the rear and front legs make the robot hop in place (often rotating significantly around its own axis), while long delays caused it to sway back and forth without making any net progress; inbetween the extremes lies an optimal delay. However, due to the slightly uneven weight distribution on board the robot, the maximum traveled distance and the corresponding optimal timing pattern varied depending on the intended heading.

For most of the tested configurations, the results were very consistent over the five runs using the same timing pattern, while the direction of the deviation changed randomly between different timing configurations. Most of the tests showed significant sideways drifting of the robot to either side, deviating from the intended heading while simultaneously rotating, most often outwards and sometimes more than 45°, thus describing a circular trajectory over many jumps instead of a straight line.

A number of possible reasons were listed for this erratic behavior. Most notably, even after thorough cleaning of the floor surface, the silicone actuators quickly become dirty after a number of jumps. This drastically affects the friction between the legs and the ground, resulting in a reduced traveled distance. Also, the lack of consistency in the resulting deviation could be explained by the legs collecting dirt at different, random rates. It was also theorized that an actuator might perform worse due to small differences in the material and the manufacturing.

A possibility that was not explored in depth is the onset of fatigue in the actuator's material and especially at the seam between the two halves, either from the initial pressure surge when firing the valves, or from pressure shock occurring at landing. During the 200 runs, two actuators failed at the seam, resulting in significantly degraded jumping performance as all the opening acted as a pressure relief preventing the legs from inflating properly. The affected test runs were not included and the experiment repeated with a new actuator. Abrasion of the actuator's bottom surface through contact with the floor could also be an issue, though it is unlikely this had any significant effect on the relatively low number of test runs performed.

Another discarded reason for the deviation was the effect of the air supply pipe. It was initially thought that a twisted pipe could exert a torque on the robot while in midair, causing it to yaw. However, simple counter-experiments conducted with the supply pipe severely twisted by turning the robot multiple times around its axis before placing it on the ground resulted in no change in its behavior, regardless of the twisting direction.

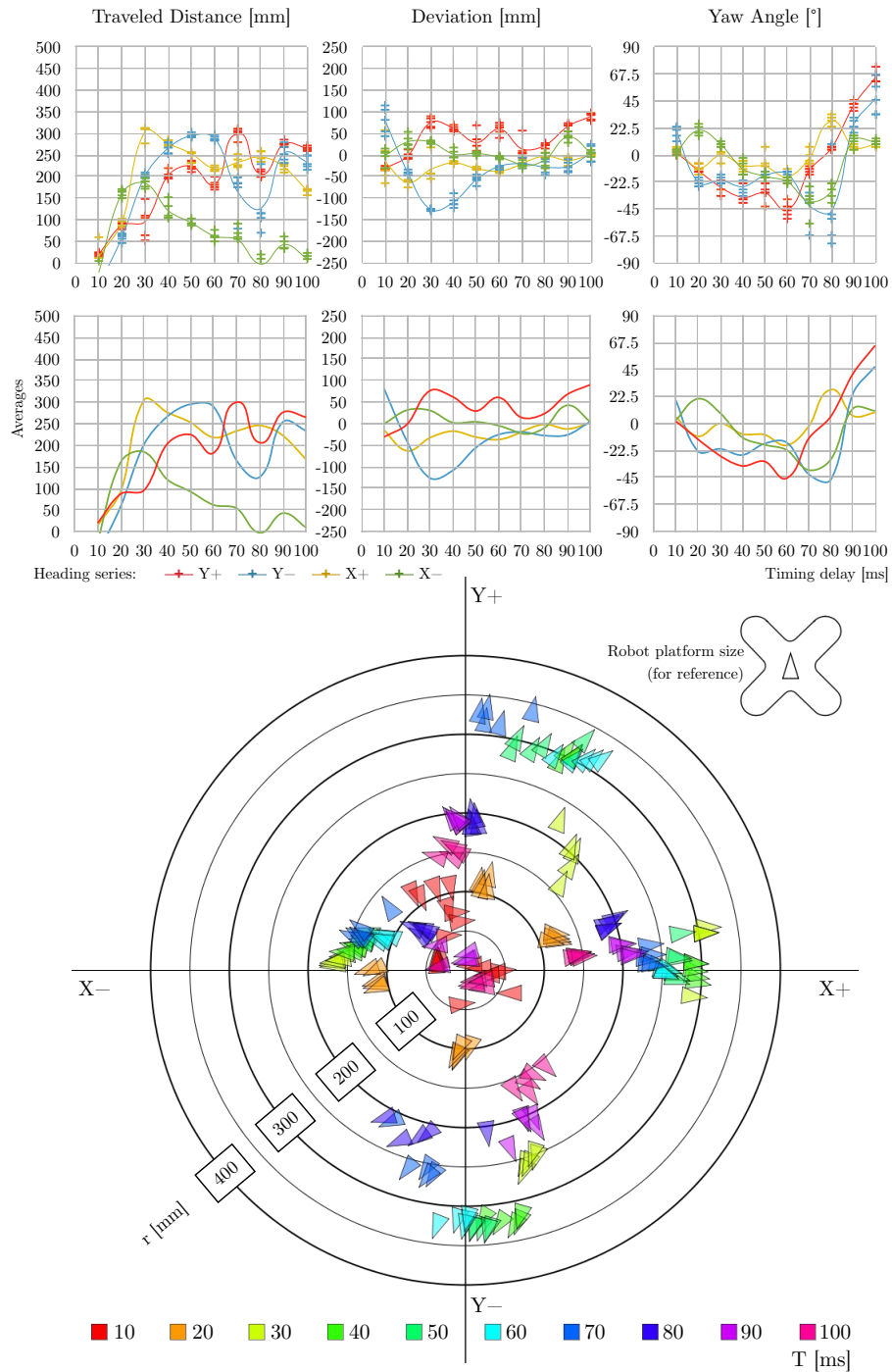


Figure 5.4: Directional jumping - experimental results

5.2.4 Sensor data

Figure 5.5 shows some data collected by the robot's IMU sensors while performing a typical jump, here with 100 ms between beginning the recording and performing the jump, and a 50 ms timing difference between rear and front legs, although with a slightly higher pressure of 0.3 MPa. The values displayed are linear acceleration in the y (forward) and z (upward) directions and the rotational speed around the robot's pitch axis (x). After an initial acceleration burst from the rear legs, the robot tilts forward until the front legs reverse the rotation, the platform lifts off the ground shortly after and enters the freefall phase (while rotating) before touching down again and bouncing before coming to a complete stop. The top chart showing an experiment with the exhaust valve attached reveals the increased bouncing upon touchdown due to the remaining air in the actuators (see 5.2.2).

The IMU's accelerometer and gyroscope were used to measure jumping performance, both for direct measurement of acceleration and rotation, as well as for determining locomotion speed and distance through integration of the gathered acceleration data. It is known that integrating a digitized physical quantity will show inherent drift [59], especially when using double integration to gain travelled distance from the measured acceleration, $x = \int \int a dt^2$.

However, while filtering techniques might reduce issues such as noise and drifting, a more basic problem became apparent when observing the raw accelerometer and gyroscope data: Random peaks in the data at the moment the solenoid valve opens and closes. Figure 5.6 shows the reading of the accelerometer and gyroscope data from various runs, with significant peaks in the readings taken while the solenoid valve closes at $t = 150$ ms, even with no pneumatic pressure applied to the system. The peaks in Figure 5.5 might also be affected by this problem. Both mechanical vibrations and sudden supply voltage drops were discarded as possible reasons for the peaks by powering the valves and sensor via independent power supplies and mechanically decoupling them to prevent any vibration effects, to no avail; so the most likely cause is an electromagnetic pulse (EMP) from the solenoid. Additional measures such as shielding the IMU sensors against electromagnetic interference (EMI) should be taken to be able to access their full potential.

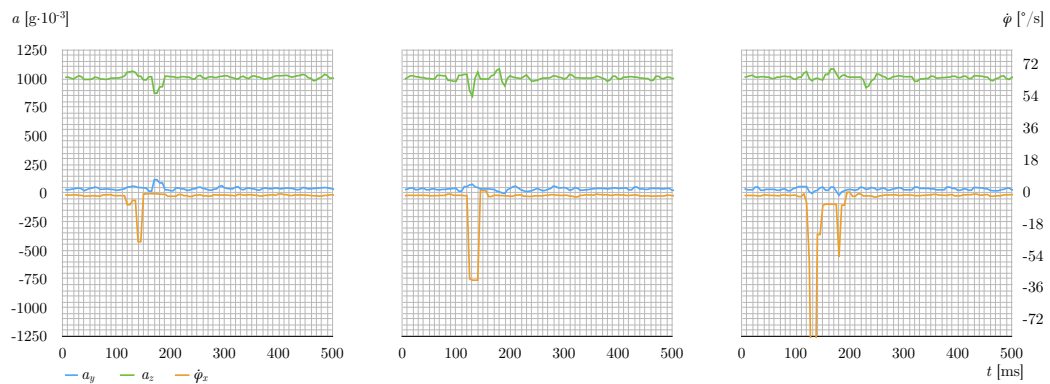


Figure 5.6: Electromagnetic interference in IMU data

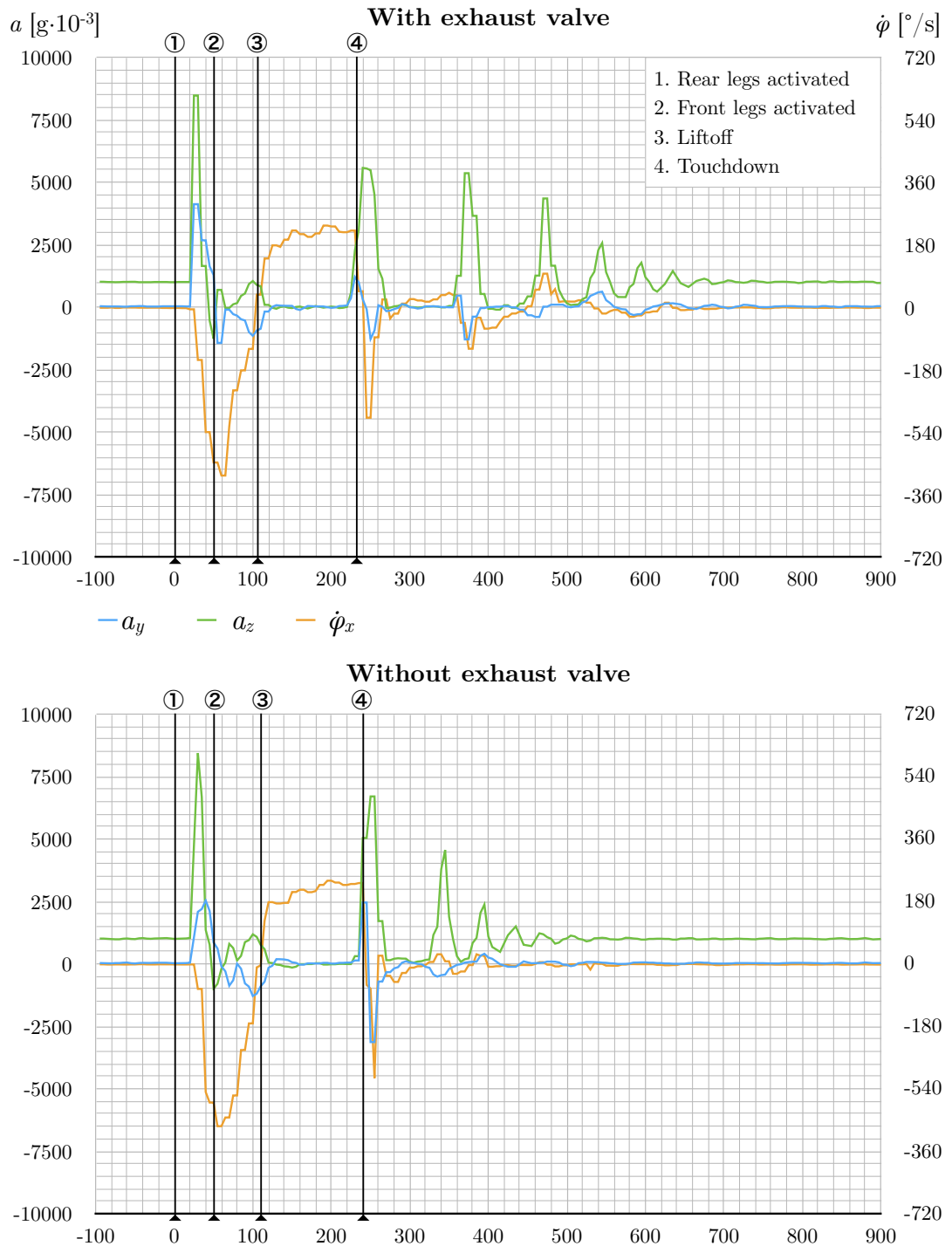


Figure 5.5: Jump pattern - IMU data

5.2.5 Heading control

It was found that at times, an actuator showing subpar performance through slower expansion had different effects on the platforms jumping behavior. A difference between the two rear actuators seemed to cause only small deviations, whereas the robot would noticeably swerve towards the side of the weaker leg when the defect was on the front actuators. This was confirmed by artificially 'weakening' one of the front legs through software, by further delaying its actuation time by an interval d with respect to the other one:

```
j T T+d 0 0 T+50 T+50 50 50
```

Even delays in the order of $1 \text{ ms} \leq d \leq 3 \text{ ms}$ caused a change of heading of the robot of $\leq 10^\circ$ (measured by the platform's compass sensor), making it describe a circular trajectory when repeated multiple times.

This lead to the development of a simple, proof-of-concept control strategy to help the robot maintain a straight heading by compensating for small deviations as outlined in Figure 5.7. After performing a (theoretically) straight jump, the compass sensor would measure any change in heading and adjust the timing pattern accordingly before continuing with the next jump. By continually tuning the jumping parameters, this resulted in a proportional control scheme able to dramatically improve the locomotion performance.

The minimal solution presented here takes the deviation $\Delta\alpha_i$ gathered by the sensor (in degrees) after the i th jump, and determines a new delay d_i based on the delay used in the previous jump d_{i-1} and the deviation $\Delta\alpha_i$ scaled by a learning rate factor μ . Depending on the sign of d_i , either the left or right front leg's actuation is delayed by the amount $d_{1,i}$ or $d_{2,i}$, respectively.

$$d_0 = 0 \quad (5.1)$$

$$d_i = d_{i-1} + \mu \cdot \Delta\alpha_i \quad (5.2)$$

$$d_{1,i} = \begin{cases} |d| & \text{if } d_i < 0 \\ 0 & \text{otherwise} \end{cases} \quad (5.3)$$

$$d_{2,i} = \begin{cases} d & \text{if } d_i > 0 \\ 0 & \text{otherwise} \end{cases} \quad (5.4)$$

The resulting behavior can be described by the following command:

```
j T+d1i T+d2i 0 0 T+50 T+50 50 50
```

In practice, a factor of $\mu = 1$ (adjusting the delay by 1 ms for each degree of deviation) proved itself most useful, as higher values resulted in an overcorrecting, zig-zag-like motion. This method only compensates for rotational deviation; any sideways drifting of the platform is not accounted for.

5.3 Wireless/pipelineless operation

All experiments described previously were conducted using external sources of air pressure and electrical power, mostly for practical reasons so as to avoid wasting compressed gas tanks and having to stop to recharge batteries. Another cause was the difficulty in finding suitable components to achieve the desired pneumatic system as this is a highly unusual setup, resulting in limited time to test the on-board pressure supply. However, one of the motivations of this endeavor was to examine the feasibility of a fully wireless and pipelineless system, for applications where providing a tether would pose too many problems, e.g. in

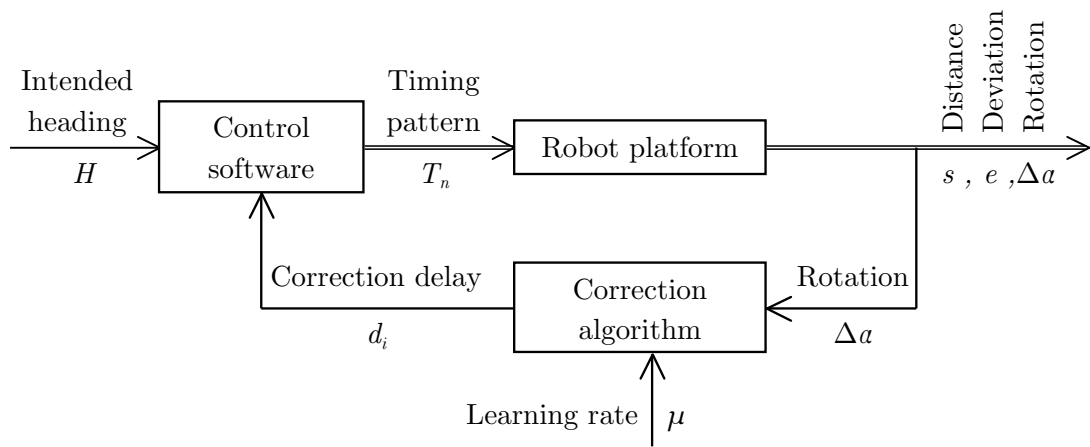


Figure 5.7: Heading control - block diagram

cramped places or when traveling long distances. The platform was thus outfitted with an on-board pressure source as described in 4.2.3 and the rechargeable LiPo batteries mentioned in 4.3.5.

It immediately became apparent that the concatenation of regulators put strong limits on the performance of the robot by limiting the effective flow rate of gas going into the actuators, in addition to the increased payload weight. Vertical jumping height dropped from 95 mm to between 40 and 50 mm due to the combined effect of these factors. Unfortunately, at the time of testing there was no simpler way of attaching the high pressure CO₂ tank to the relatively low pressure system of the platform than the large and cumbersome regulator.

Directional jumping was also severely hampered by the added weight and especially by the weight distribution inside the robot. When choosing a Y+ or Y- heading (with the actuator and batteries on either side of the platform), locomotion was possible, albeit with a strong tendency to swerve towards the regulator's side due to its significant weight. It was possible to correct this inaccuracy by way of the control algorithm (5.2.5), but it was difficult to find a suitable learning rate to balance between fast adaptation and overcompensation (which resulted in zig-zag-like trajectories), as the behavior often changed from jump to jump. Jumping in the X+ direction with the heavy regulator in the front did not allow any significant movement in the desired heading, while jumps towards X- regularly resulted in the platform flipping over. Due to time limitations, it was not possible to perform a systematic study of the optimal timing patterns as described in 5.2.3 for the autonomous robot, though this would be of key interest for further analyzing the practicality of compact autonomous pneumatic robots. An optimized version of the platform with an optimized weight distribution including all pressure supply components should perform better than the initial prototype presented here.

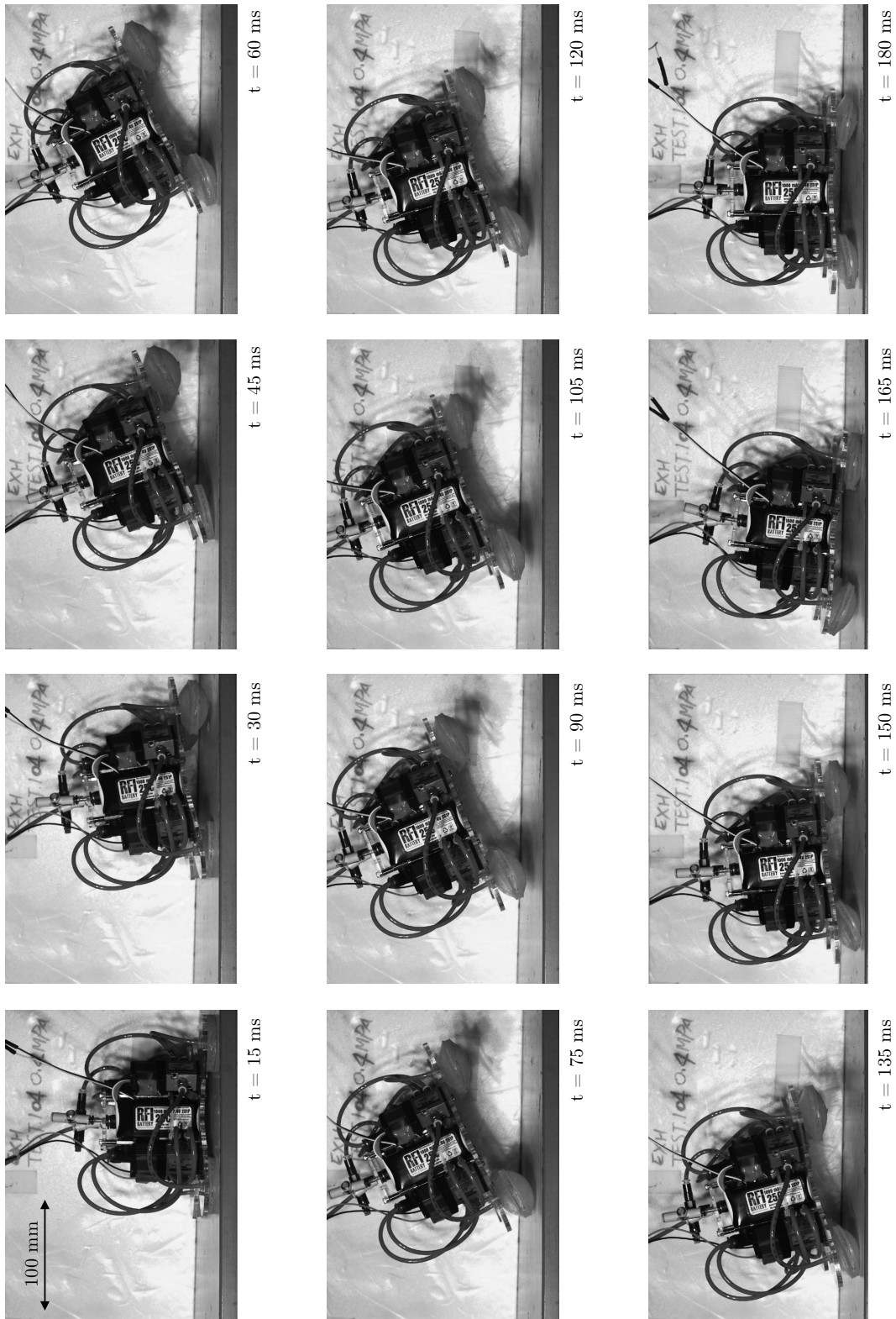


Figure 5.8: Sequential pictures of a directional jump

6 Summary and Outlook

6.1 Summary

In the previous chapters, a robotic jumping platform was developed, starting from the design and study of the silicone elastomer actuators all the way to a working prototype capable of performing both upwards jumps and small leaps in different directions specified by the user, adapting its control parameters to ensure the deviation from the intended path stays as low as possible. By analyzing both the results of the jumps as well as the stream of data collected during each run, a number of interesting insights were gained. Perhaps most importantly, the study helped highlight some of the challenges that arise when developing mobile jumping robots, especially those using pneumatic systems.

6.2 Challenges

Firstly, while section 5.2 demonstrated that directional control of the jumping motion is indeed possible, the behavior observed is perhaps best described by the term *hopping* rather than jumping. In order to better deal with obstacles, a higher ratio of jumping height and distance to body size should be achieved, e.g. for climbing stairs. Only limited knowledge about the airflow within the system was available; nevertheless, it is believed that the maximum flow rate into the actuators plays a key role in determining overall jumping performance. It is most difficult to find compact pneumatic components capable of delivering flowrates higher than the regulators and valves presented here at the required pressure ratings, especially when employing CO₂ canisters. It is unclear whether using larger diameter piping throughout the system could partially alleviate the shortcomings of the current setup. A radically different idea was proposed by Kojimoto [60]: A chemical pneumatic battery capable of producing pressurized oxygen from a catalytic reaction of H₂O₂, capable of producing almost the 0.5 MPa used in the current jumping platform setup.

When measuring the performance of the soft actuators on the platform, there were a number of uncertainties to be dealt with. Manufacturing defects, material wear and dirt buildup during test runs are very difficult to quantify. When employing on-board power sources, the charging state of both the pressure tank and the battery at any given time could greatly affect the motion capabilities of the robot and become two more variables to take into account, with potentially many ramifications (e.g. varying valve opening delays due to lower battery voltage, requiring adapted timing patterns for optimal performance).

6.3 Further ideas

Future improvements to the jumping robot platform could open up new fields of study. The soft silicone actuators' shape and dimensions were selected quite early in the development, as they were large enough to be easy to manufacture (especially before perfecting the laser-cut molds) and handle, and small enough to require reasonable amounts of air to be fully inflated. Of course, much can still be done in terms of improving the overall design as well as particular dimensions of the actuators. A more systematic study to reveal more about the effects that influence their performance would be highly desirable.

Regarding the jumping motion, one aspect left largely unconsidered so far is the landing after a jump. Perhaps by inflating the actuators again shortly before touchdown in a specific pattern, the traveled distance could be increased and the physical shock to the platform reduced, mitigating stress on the individual parts. A continuous jumping motion, akin to natural gaits such as galloping could also be explored,

by omitting the stationary phase between two jumps, potentially reusing some of the energy before landing for the subsequent jump. Another possibility would be for the robot to adjust its own position *during* the flight phase to prepare for the furthest jump or the smoothest possible landing, be it by inflating its own legs, by using dedicated actuators (e.g. attached to inertial masses) or by using controlled ejection of gas in a specific direction.

If the IMU's sensor data could be gathered in a more reliable fashion (without the drawbacks mentioned in 5.2.4), a machine learning approach could be used to allow the robot to self-improve its performance. By measuring the precise acceleration and rotation profile during a jump and deducing the traveled distance, a self-optimizing system without the need for external data analysis could be implemented. For example, by performing a large number of jumps with random timing patterns and measuring their effect on the jumping motion, optimal patterns could potentially be discovered by the robot itself, without the need for systematic testing as portrayed here and with no necessary detailed knowledge of the underlying mechanics. Furthermore, as no external measurement instruments are necessary for the proposed approach, this would constitute learning from the robot's own perspective [61]. This system could easily compensate for differences between individual actuators, changing weight distributions and other factors. Machine algorithms are very well documented, the critical factor is to gather reliable training data.

Currently, only one regulator is used to adjust the pressure in the whole system. Being able to control the pressure sent into each actuator independently might lead to new ways to control the behavior of the robot. At the same time, if the regulator were found to be a main limiter of the achievable flowrate, this would lead to better performance since the airflow would be spread over multiple regulators (one per leg). Proportional valves might offer a similar way to fine-tune the robot's behavior.

Lastly, in the spirit of Soft Robotics, it would be very interesting to further simplify the manufacturing of the jumping robot. It would be highly desirable to have a platform that is fully soft and that can be cast in only a few separate parts, including all necessary actuators and the air distribution system as canals embedded in the material, possibly even a kind of soft valve, to eliminate the need for a rigid structure holding all components. By even embedding the electronics into the silicone, a highly robust system could be used for exploring rough terrain and withstand dangers such as shock (critical for hard or brittle materials), water (fatal for electronics) or even chemical substances (e.g. corrosion of metal).

7 Appendix

Silicone datasheets

1. EcoFlex 00-30
2. ShinEtsu KE-1310ST
3. Sylgard 184

Pneumatic datasheets

1. SNS 3V1-08-DC24V Solenoid Valve
2. SMC VK332-6DS-M5-Q Solenoid Valve
3. SMC ARJ1020F-M5-04 Regulator
4. SMC AQ240F-04-00 Exhaust Valve
5. UP A-167-G Regulator
6. LUFT CO2 Tire Inflator

Electronics datasheets

1. Iteaduino Nano Microcontroller Board
2. FQP30N06L N-Channel MOSFET
3. GY-80 Inertial Measurement Unit
4. CHHBS Load Cell
5. INA114 Instrumentation Amplifier
6. LM78XX Positive Voltage Regulator

Ecoflex® Series

Super-Soft, Addition Cure Silicone Rubbers



www.smooth-on.com

PRODUCT OVERVIEW

Ecoflex® rubbers are platinum-catalyzed silicones that are versatile and easy to use. Ecoflex® rubbers are mixed 1A:1B by weight or volume and cured at room temperature with negligible shrinkage. Rubber also cures without a "tacky" surface. Low viscosity ensures easy mixing and de-airing, or you can choose to mix and dispense using our convenient dispensing cartridges.

Cured rubber is very soft, very strong and very "stretchy", stretching many times its original size without tearing and will rebound to its original form without distortion. Ecoflex® rubbers are water white translucent and can be color pigmented with Silc Pig® pigments for creating a variety of color effects. You can also add Smooth-On's Silicone Thinner® to further lower the viscosity. THI-VEX® silicone thickener can be added by weight to Ecoflex® 5 or Ecoflex® 00-10 for brushable applications. **Note: THI-VEX® is NOT compatible with Ecoflex® 00-30, Ecoflex® 00-20 or Ecoflex® 00-50.**

Soft, Softer, Softest... Ecoflex® rubbers are based on Smooth-On's Dragon Skin® technology and are currently available in four different hardness': Shore A-5, Shore 00-10, 00-20, 00-30 and 00-50. They are suitable for a variety of applications including making prosthetic appliances, cushioning for orthotics and special effects applications (especially in animatronics where repetitive motion is required). Ecoflex® 5 has a pot life of 1 minute and a demold time of 5 minutes – Available only in dispensing cartridges.

TECHNICAL OVERVIEW

	Mixed Viscosity (ASTM D-23393)	Specific Gravity (g/cc) (ASTM D-1475)	Specific Volume (cu. in./lb.) (ASTM D-1475)	Pot Life (ASTM D-2471)	Cure Time	Shore Hardness (ASTM D-2240)	Tensile Strength (ASTM D-412)	100% Modulus (ASTM D-412)	Elongation at Break % (ASTM D-412)	Die B Tear Strength (ASTM D-624)	Shrinkage (in./in.) (ASTM D-2566)
Ecoflex® 5	13,000 cps	1.07	25.8	1 min.	5 min.	5A	350 psi	15 psi	1000%	75 pli	<.001 in./in.
Ecoflex® 00-50	8,000 cps	1.07	25.9	18 min.	3 hours	00-50	315 psi	12 psi	980%	50 pli	<.001 in./in.
Ecoflex® 00-30	3,000 cps	1.07	26.0	45 min.	4 hours	00-30	200 psi	10 psi	900%	38 pli	<.001 in./in.
Ecoflex® 00-20	3,000 cps	1.07	26.0	30 min.	4 hours	00-20	160 psi	8 psi	845%	30 pli	<.001 in./in.
Ecoflex® 00-10	14,000 cps	1.04	26.6	30 min.	4 hours	00-10	120 psi	8 psi	800%	22 pli	<.001 in./in.

*All values measured after 7 days at 73°F/23°C

Mix Ratio: 1A:1B by volume or weight
Color: Translucent

Useful Temperature Range: -65°F to 450°F (-53°C to 232°C)
Dielectric Strength (ASTM D-147-97a): >350 volts/mil

PROCESSING RECOMMENDATIONS

PREPARATION... Safety – Use in a properly ventilated area ("room size" ventilation). Wear safety glasses, long sleeves and rubber gloves to minimize contamination risk. Wear vinyl gloves only. Latex gloves will inhibit the cure of the rubber.

Store and use material at room temperature (73°F/23°C). Warmer temperatures will drastically reduce working time and cure time. Storing material at warmer temperatures will also reduce the usable shelf life of unused material. These products have a limited shelf life and should be used as soon as possible.

Cure Inhibition – Addition-cure silicone rubber may be inhibited by certain contaminants in or on the pattern to be molded resulting in tackiness at the pattern interface or a total lack of cure throughout the mold. Latex, tin-cure silicone, sulfur clays, certain wood surfaces, newly cast polyester, epoxy or urethane rubber may cause inhibition. If compatibility between the rubber and the surface is a concern, a small-scale test is recommended. Apply a small amount of rubber onto a non-critical area of the pattern. Inhibition has occurred if the rubber is gummy or uncured after the recommended cure time has passed.

Because no two applications are quite the same, a small test application to determine suitability for your project is recommended if performance of this material is in question.

To prevent inhibition, one or more coatings of a clear acrylic lacquer applied to the model surface is usually effective. Allow any sealer to thoroughly dry before applying rubber. Note: Even with a sealer, platinum silicones will not work with modeling clays containing heavy amounts of sulfur. Do a small scale test for compatibility before using on your project.

Safety First!

The Material Safety Data Sheet (MSDS) for this or any Smooth-On product should be read prior to use and is available upon request from Smooth-On. All Smooth-On products are safe to use if directions are read and followed carefully.

Keep Out of Reach of Children

Be careful. Use only with adequate ventilation. Contact with skin and eyes may cause irritation. Flush eyes with water for 15 minutes and seek immediate medical attention. Remove from skin with waterless hand cleaner followed by soap and water.

Important: The information contained in this bulletin is considered accurate. However, no warranty is expressed or implied regarding the accuracy of the data, the results to be obtained from the use thereof, or that any such use will not infringe upon a patent. User shall determine the suitability of the product for the intended application and assume all risk and liability whatsoever in connection therewith.

Applying A Release Agent - Although not usually necessary, a release agent will make demolding easier when pouring into or over most surfaces. Ease Release® 200 is a proven release agent for use with silicone rubber. Mann Ease Release® products are available from Smooth-On or your Smooth-On distributor.

IMPORTANT: To ensure thorough coverage, lightly brush the release agent with a soft brush over all surfaces of the model. Follow with a light mist coating and let the release agent dry for 30 minutes.

If there is any question about the effectiveness of a sealer/release agent combination, a small-scale test should be made on an identical surface for trial.

MEASURING & MIXING...

Before you begin, pre-mix Part B thoroughly. After dispensing required amounts of Parts A and B into mixing container (1A:1B by volume or weight), **mix thoroughly for 3 minutes making sure that you scrape the sides and bottom of the mixing container several times**. After mixing parts A and B, vacuum degassing is recommended to eliminate any entrapped air. Vacuum material for 2-3 minutes (29 inches of mercury), making sure that you leave enough room in container for product volume expansion.

POURING, CURING & MOLD PERFORMANCE...

For best results, pour your mixture in a single spot at the lowest point of the containment field. Let the rubber seek its level up and over the model. **A uniform flow will help minimize entrapped air.** The liquid rubber should level off at least 1/2" (1.3 cm) over the highest point of the model surface.

Curing / Post Curing - Allow rubber to cure as prescribed at room temperature (73°F/23°C) before demolding. Do not cure rubber where temperature is less than 65°F/18°C. **Optional:** Post curing the mold will aid in quickly attaining maximum physical and performance properties. After curing at room temperature, expose the rubber to 176°F/80°C for 2 hours and 212°F/100°C for one hour. Allow mold to cool to room temperature before using.

If Using As A Mold - When first cast, silicone rubber molds exhibit natural release characteristics. Depending on what is being cast into the mold, mold lubricity may be depleted over time and parts will begin to stick. No release agent is necessary when casting wax or gypsum. Applying a release agent such as Ease Release® 200 (available from Smooth-On) prior to casting polyurethane, polyester and epoxy resins is recommended to prevent mold degradation.

Thickening Ecoflex® Silicones - THI-VEX® may be added into Ecoflex® 5 & 00-10 by weight. The recommended maximum amount of THI-VEX® is 2% by weight. **THI-VEX® thickener is not compatible with Ecoflex® 00-30, 00-20 or 00-50.** An alternative for thickening Ecoflex® silicones is to add Ure-Fil® 9 or Ure-Fil® 11.

Thinning Ecoflex® Silicones - Smooth-On's Silicone Thinner® will lower the viscosity of Ecoflex® silicones for easier pouring and vacuum degassing. A disadvantage is that ultimate tear and tensile are reduced in proportion to the amount of Silicone Thinner® added. **It is not recommended to exceed 10% by weight of total system (A+B).** See the Silicone Thinner® technical bulletin (available from Smooth-On or your Smooth-On distributor) for full details.

Mold Performance & Storage - The physical life of the mold depends on how you use it (materials cast, frequency, etc.). Casting abrasive materials such as concrete can quickly erode mold detail, while casting non-abrasive materials (wax) will not affect mold detail. Before storing, the mold should be cleaned with a soap solution and wiped fully dry. Two part (or more) molds should be assembled. Molds should be stored on a level surface in a cool, dry environment.



Call Us Anytime With Questions About Your Application.

Toll-free: **(800) 762-0744** Fax: **(610) 252-6200**

The new www.smooth-on.com is loaded with information about mold making, casting and more.

Shin-Etsu

Shin-Etsu Silicone

RTV Silicone Rubber for Moldmaking



General Characteristics

● Addition-cure type

High strength addition-cure type								
Product		KE-1300T	KE-1310ST		KE-1310T	KE-1314-2		KE-1316
Before curing	Appearance	Translucent	Translucent		Translucent	Translucent		Translucent
	Viscosity (Pa·s)	95	75		70	75		35
	Curing agent Standard added amount	CAT-1300 10.0%	CAT-1310S 10.0% ^{*3}	CAT-1310L 10.0%	CX-32-1649 10.0%	CAT-1314S 10.0% ^{*3}	CAT-1314L 10.0%	CAT-1316 10.0% ^{*4}
	Finger touch method: 23°C (min.)	90	80	330	480	90	570	60
	Standard curing time (hours/°C) ^{*2}	24/23	24/23	–	24/23	24/23	–	24/23
	Curing inhibition	Yes	Yes	Yes	Yes	Yes	Yes	Yes
	Time to make test piece (hours/°C)	2/60	2/60	4/60	2/60	2/60	4/60	2/60
After curing	Appearance	Translucent	Translucent	Translucent	Translucent	Translucent	Translucent	Translucent
	Density (23°C)	1.09	1.08	1.08	1.08	1.08	1.08	1.13
	Hardness (durometer A)	40	40	40	40	40	40	23
	Tensile strength (MPa)	5.0	5.5	5.7	5.5	5.0	5.9	6.5
	Elongation (%)	400	350	320	350	350	350	700
	Tear strength (kN/m)	17	25	26	21	25	25	33
	Linear shrinkage (%)	0.1	0.1	0.1	0.1	0.1	0.1	0.1
	Special characteristics	Improved urethane resistance		Improved epoxy resistance	Oil bleed		Low hardness	

*1 The workable time of RTV rubbers indicates how long the material will remain fluid at 23 °C. However, work should be carried out in the shortest possible time because viscosity increases with time.

*2 Standard curing time will vary depending on the size of the cured item.

*3 For KE-1310ST and KE-1314-2, we offer a special curing agent used to adjust cure speed and hardness.

*4 For KE-1316, we offer a special curing agent used to adjust hardness and cure speed and impart adhesiveness.

*5 KE-1600: Hardness can be increased to 70 by performing an aging process (150 °C×30 min) after the standard cure time elapses.

*6 KE-1241: Hardness measured by Asker C hardness tester.

*7 For KE-1308, we offer a special curing agent used to adjust hardness.

*8 The hardness of KE-1308 is affected by cure temperature. To achieve the prescribed hardness, we recommend 120 °C×30 min.

*9 KE-1308: Hardness measured by Asker C hardness tester.

Product Information

DOW CORNING

Encapsulants

Dow Corning® 184 Silicone Elastomer

FEATURES

- Flowable
- RT and heat cure
- High tensile strength
- Same as Sylgard 182 but with RT cure capability
- UL and Mil Spec tested

BENEFITS

- Rapid, versatile cure processing controlled by temperature
- High transparency allows easy inspection of components
- Can be considered for uses requiring UL and Mil Spec requirements

COMPOSITION

- 2-part
- 10:1 mix ratio
- Polydimethylsiloxane elastomer

APPLICATION METHODS

- Automated metered mixing and dispensing
- Manual mixing

Transparent encapsulant with good flame resistance

APPLICATIONS

- General potting applications
- Power supplies
- Connectors
- Sensors
- Industrial controls
- Transformers
- Amplifiers
- High voltage resistor packs
- Relays
- Adhesive/encapsulant for solar cells
- Adhesive handling beam lead integrated circuits during processing

TYPICAL PROPERTIES

Specification Writers: These values are not intended for use in preparing specifications. Please contact your local Dow Corning sales office or your Global Dow Corning Connection before writing specifications on this product.

Property	Unit	Value
Viscosity (Part A)	cP	5175
	mPa-sec	5175
	Pa-sec	5.2
Viscosity (Mixed)	cP	3500
	mPa-sec	3500
	Pa-sec	3.5
Specific Gravity (Uncured Base)	-	1.03
Specific Gravity (Cured)	-	1.04
Working Time at 25°C (Pot Life - hours)	hr	1.4
Cure Time at 25°C	hrs	48
Heat Cure Time @ 100°C	minutes	35
Heat Cure Time @ 125°C	minutes	20
Heat Cure Time @ 150°C	minutes	10

DESCRIPTION

Dow Corning® silicone encapsulants are supplied as two-part liquid component kits. When liquid components are thoroughly mixed, the mixture cures to a flexible elastomer, which is well suited for the protection of electrical/electronic applications. Dow Corning silicone encapsulants cure without exotherm at a constant rate regardless of sectional thickness or degree of confinement. Dow Corning silicone elastomers require no post cure and can be placed in service immediately following the completion of the cure schedule. Standard silicone encapsulants require a surface treatment with a primer in addition to good cleaning for adhesion while primerless silicone encapsulants require only good cleaning. Underwriters Laboratory (UL) 94 recognition is based on minimum thickness requirements. Please consult the UL Online Certifications Directory for the most accurate certification information.

MIXING AND DE-AIRING

The 10:1 mix ratio these products are supplied in gives one latitude to tune the modulus and hardness for specific application needs and production lines. In most cases de-airing is not required.

PREPARING SURFACES

In applications requiring adhesion, priming will be required for many of the silicone encapsulants. See the Primer Selection Guide for the correct primer to use with a given product. For best results, the primer should be applied in a very thin, uniform coating and then wiped off after application. After application, it should be thoroughly cured prior to application of the silicone elastomer. Additional instructions for primer usage can be found in the information sheets specific to the individual primers.

PROCESSING/CURING

Thoroughly mixed Dow Corning silicone encapsulant may be poured/dispensed directly into the

TYPICAL PROPERTIES, continued

Property	Unit	Value
Tensile Strength	psi MPa kg/cm ²	1025 7.1 71
Elongation	%	120
Tear Strength (Die B)	ppi N/cm	5 2
Durometer Shore A	-	44
Dielectric Strength	volts/mil kV/mm	475 19
Volume Resistivity	ohm*cm	2.9E+14
Dielectric Constant at 100 Hz	-	2.72
Dielectric Constant at 100 kHz	-	2.68
Dissipation Factor at 100 hz	-	0.00257
Dissipation Factor at 100 kHz	-	0.00133
Mil Specification	NA	Mil Spec
Agency Listing	-	UL 94V-0
Shelf Life at 25°C	months	24
Refractive Index @ 589 nm	-	1.4118
Refractive Index @ 632.8 nm	-	1.4225
Refractive Index @ 1321 nm	-	1.4028
Refractive Index @ 1554 nm	-	1.3997

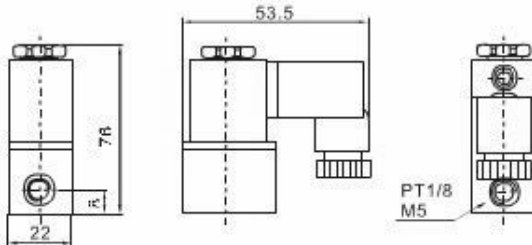
container in which it is to be cured. Care should be taken to minimize air entrapment. When practical, pouring/dispensing should be done under vacuum, particularly if the component being potted or encapsulated has many small voids. If this technique cannot be used, the unit should be evacuated after the silicone encapsulant has been poured/dispensed. Dow Corning

silicone encapsulants may be either room temperature (25°C/77°F) or heat cured. Room temperature cure encapsulants may also be heat accelerated for faster cure. Ideal cure conditions for each product are given in the product selection table. Two-part condensation cure encapsulants should not be heat accelerated above 60°C (140°F).



3V1-06

外型尺寸



3V1系列电磁阀

订货型号

3V1

- **06**

AC220V

规格代号
三口二位电磁阀

接管口径
06:1/8"
08:1/4"

标准电压
DC12V
DC24V
AC24V 50/60Hz
AC110V 50/60Hz
AC220V 50/60Hz
AC380V 50/60Hz

技术参数

型号	3V1-06	3V1-08
工作介质		空气
工作方式		直动式
型式		常闭式
流量孔径(mm ²)		2.5
CV值		0.23
接管口径	1/8 "	1/4 "
使用流体粘滞度		Under 20CST
使用压力		0~8.0kgf/cm ²
最大耐压力		10kgf/cm ²
工作温度		-5~60°C
使用电压范围		±10%
重量(kg)		
主要配件材质	本体	铝合金
	密封圈	NBR

3 Port Direct Operated Poppet Solenoid Valve Rubber Seal Series VK300

Universal porting

Available for N.C. valve, N.O. valve, divider valve, selector valve, etc.

N/min: 196

Compact/Width 18 X Length 63 (mm)

Low consumption

4W DC (Standard)

2W DC (Low wattage style)

Applicable for vacuum use

-101.2kPa

Copper-free specifications standard

The portions that come in contact with fluids do not contain copper, thus enabling the standard product to be used as is.



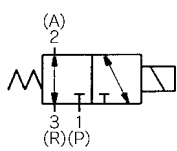
Body ported



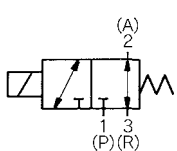
Base mounted

JIS symbol

Body ported



Base mounted



Regarding mixed installations

Series VK300 can be mounted on manifold base (VV5K3) of series VK3000.

Refer to p.1.4-4 for detailed information.

Model

	Valve Model	Operating pressure range (MPa)	Port size	Effective area* (Nl/min)	Weight (g)	
Body ported	VK332	0 to 0.7	M5	3.6 (196)	80	
	VK332Y (Low wattage, DC2W)			2.7 (147)		
	VK332E (Long loading time)	-101.2kPa to 0.1		2.7 (147)		
	VK332V (Vacuum)			3.6 (196)		
	VK332W (Low wattage, vacuum)			2.7 (147)		
Base mounted (With sub-plate)	VK334	0 to 0.7	1/8	4.2 (225)	120	
	VK334Y (Low wattage, DC2W)			2.7 (147)		
	VK334E (Long loading time)	-101.2kPa to 0.1		2.7 (147)		
	VK334V (Vacuum)			4.2 (225)		
	VK334W (Low wattage, vacuum)			2.7 (147)		



* Value at single style. In case of manifold, it depends on operating conditions.

SY

SYJ

VK

VZ

VT

VT

VP

VG

VQ

VQZ

Specifications

Actuation	Direct operated style 2 port single solenoid
Fluid	Air
Ambient and fluid temperature	MAX.50°C
Response time (0.5MPa) ⁽¹⁾	10ms or less (standard), 15ms or less (low wattage)
Manual override	Non-locking push style
Lubrication	Non-lube (Use turbine oil # 1 ISO VG32, if lubrication is required)
Mounting position	Free
Impact/vibration resistance ⁽²⁾	300/50m/s ²
Protection structure	Dust proof

Note 1) According to dynamic performance test of JIS B8374- 1981. (Coil temperature 20°C, rated voltage, without surge voltage suppressor)

Note 2) Impact resistance: No malfunction from test using drop impact tester, to axis and right angle directions of main valve and armature, each one time when energized and de-energized. (Value in the initial stage.)

Vibration resistance: No malfunction from test with 8.3 to 2000Hz 1 sweep, to axis and right angle directions of main valve and armature, each one time when energized and de-energized. (Value in the initial stage.)

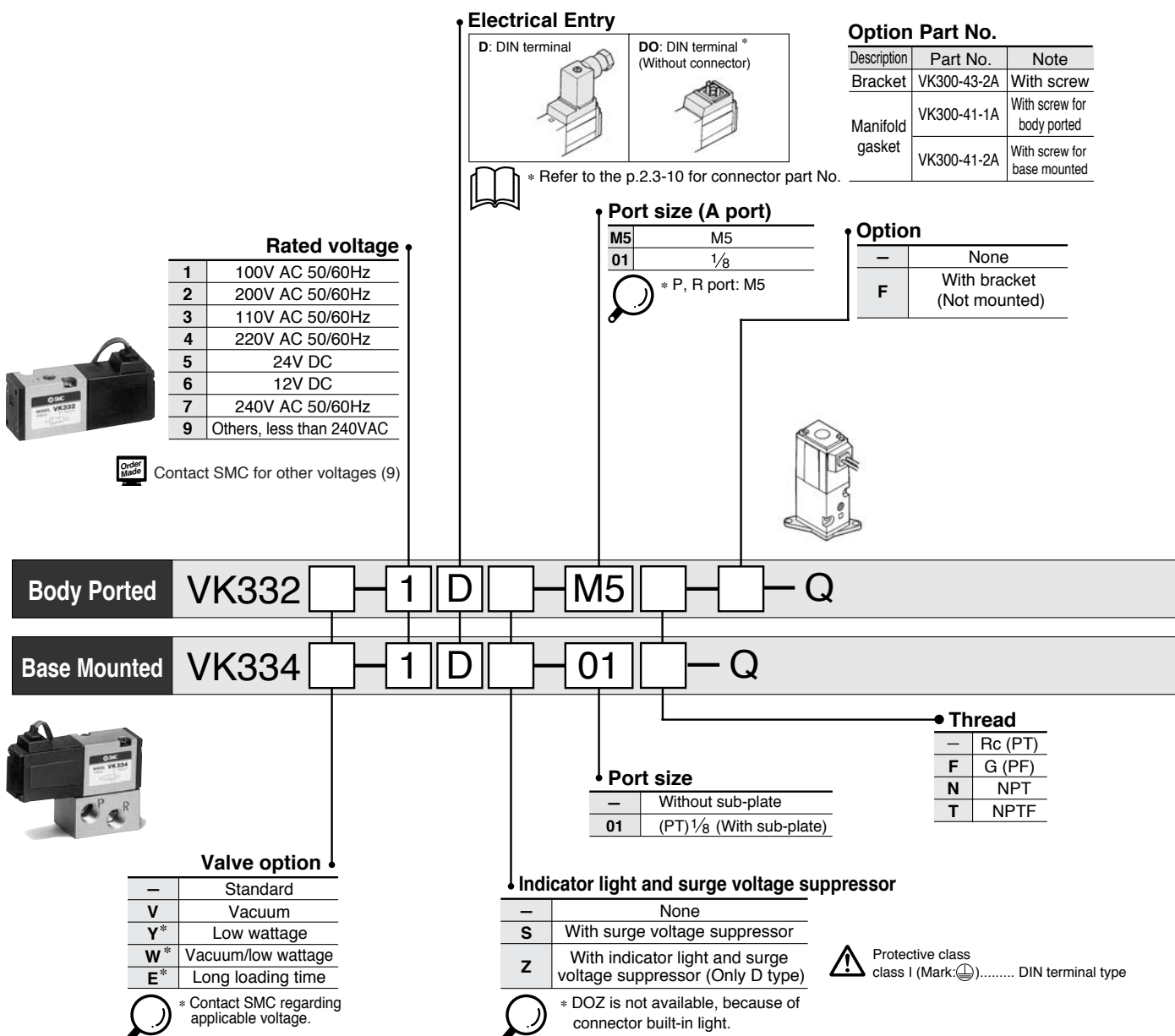
Solenoid specifications

Electrical entry	DIN terminal (D)		
Rated voltage	AC	100V, 110V, 200V, 220V, 240V	
	DC	6V, 12V, 24V, 48V	
Allowable voltage	±10% of rated voltage		
Apparent power (AC)*	Standard	Inrush	9.5VA/50Hz, 8VA/60Hz
		Holding	7VA/50Hz, 5VA/60Hz
Power consumption (DC)*	Long loading time	Inrush	3.5VA/50Hz, 3.3VA/60Hz
		Holding	3VA/50Hz, 2.8VA/60Hz
Surge voltage suppressor	Without light	4W (Standard), 2W (Low wattage)	
	With light	4.3W (Standard), 2.3W (Low wattage)	
Indicator light	AC	Varistor	
	DC	Diode (12V DC or less: varistor)	
	AC	Neon lamp	
	DC	LED	

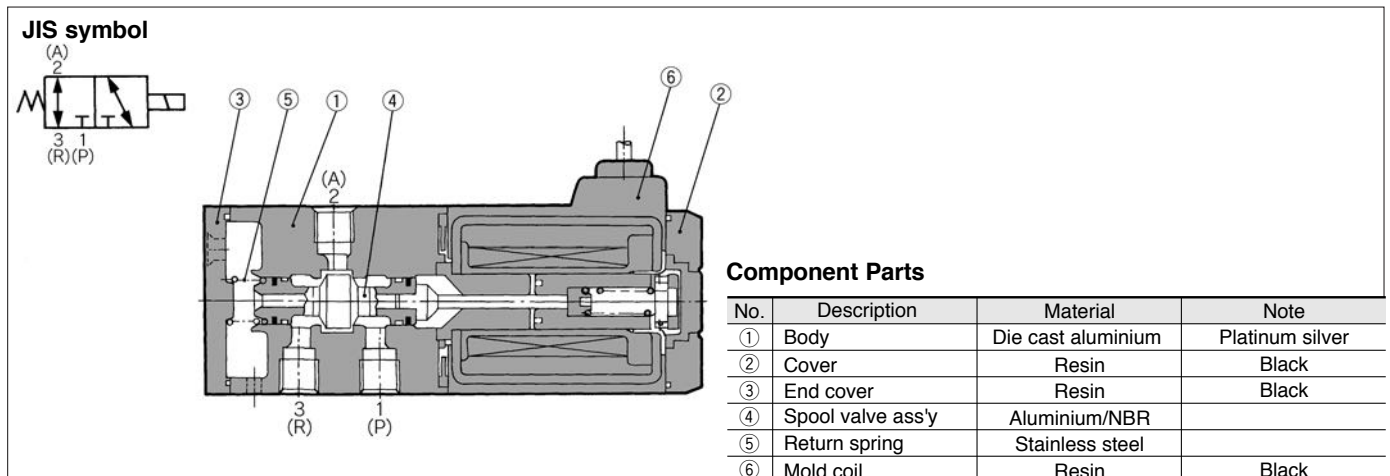


* At rated voltage

How to Order

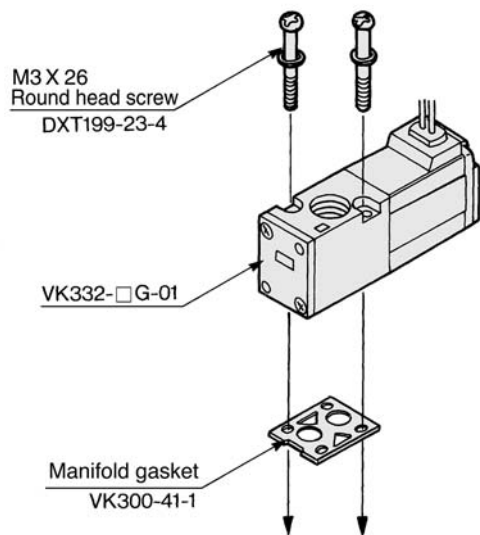


Construction



Combinations of Solenoid Valve, Manifold Gasket and Manifold Base

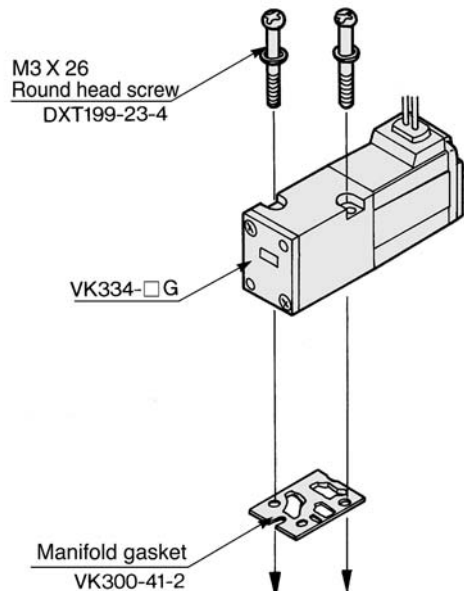
3 Port body ported: VK332



Applicable base

VV3K3-20 21	}	Manifold base
VV5K3-20 21		

3 Port base mounted: VK334



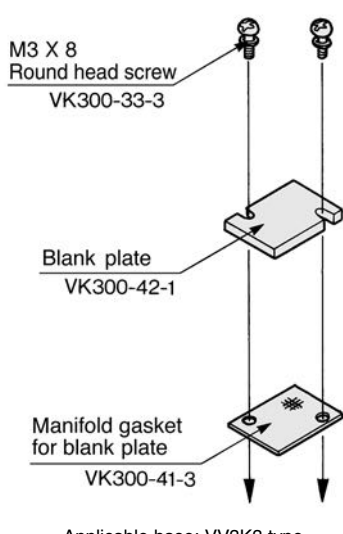
Applicable base

VK300-45-1 Sub-plate	}	Manifold base
VV3K3-40 (S) 42		
VV5K3-40 (S) 41		
(S) 42		

Note 1) Mounting direction is fixed, so do not mount on opposite side.

Note 2) Series VK300 can be mounted on manifold base (VV5K3) of series VK3000.

Combinations of Blank Plate Ass'y and Manifold Base

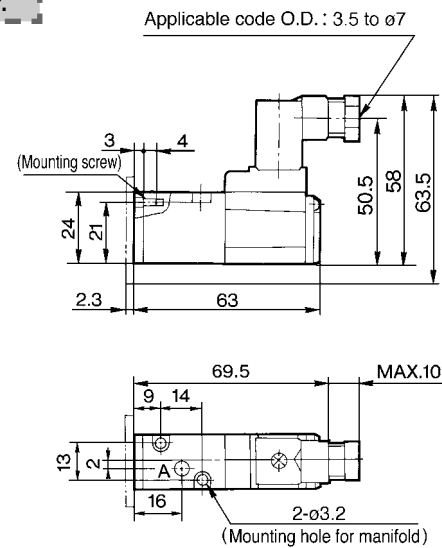
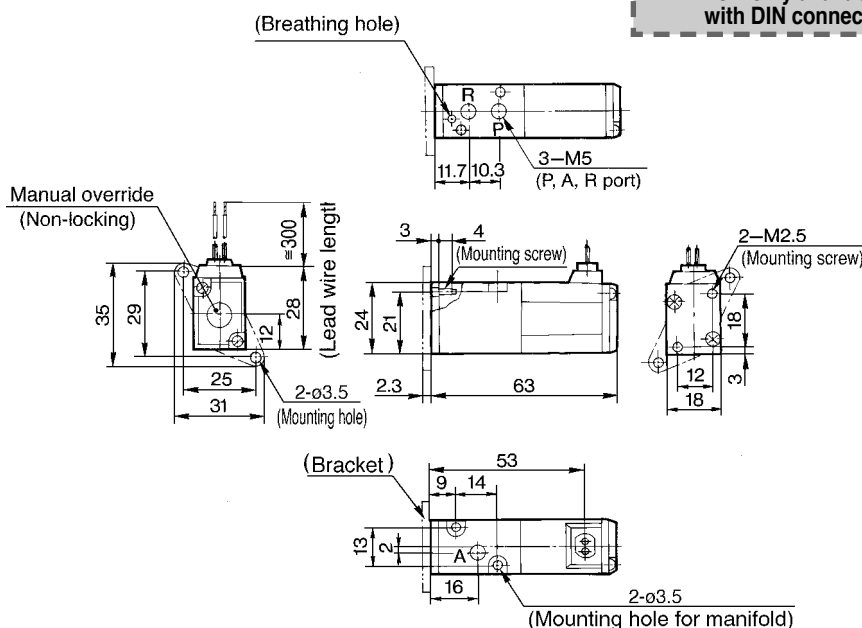


Applicable base: VV3K3 type

Body Ported/Dimensions

Grommet: VK332-□G-M5

DIN terminal: VK332-□D-M5-Q



Refer to grommet type for other dimensions.

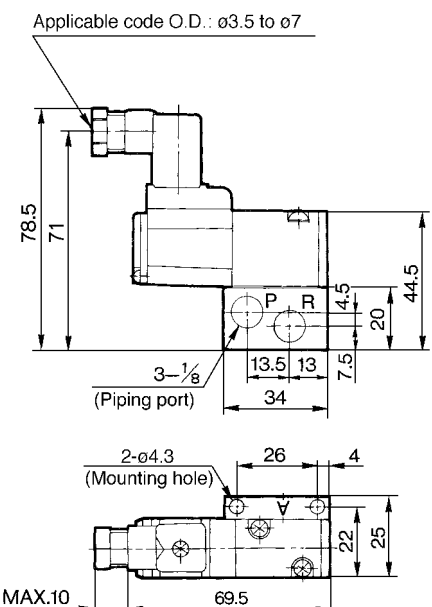
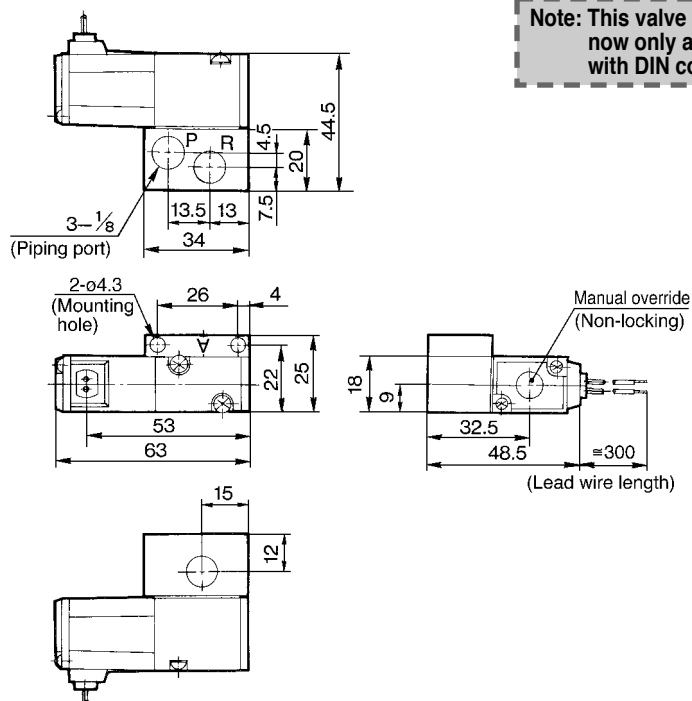
SY
SYJ
VK
VZ
VT
VT
VP
VG

VQ
VQZ

Base Mounted/Dimensions

Grommet: VK334-□G-01

DIN terminal: VK334-□D-01-Q



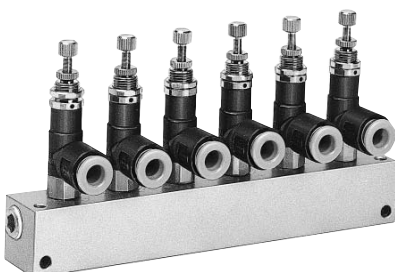
Refer to grommet type for other dimensions.

Miniature Regulator Series ARJ1020F

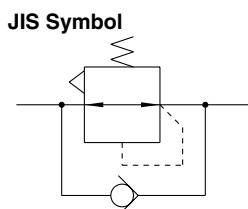
- Compact and lightweight (16 g)
- Low cracking pressure 0.02 MPa
- Standard model equipped with backflow function



ARJ1020F-M5-04 ARJ1020F-M5-06



ARJM10-6



Standard Specifications

Model		ARJ1020F	
Port size	IN side OUT side (Applicable tubing O.D.)	M5 (Male thread) ø4	ø6
Fluid		Air	
Proof pressure		1.2 MPa	
Maximum operating pressure		0.8 MPa	
Regulating pressure range		0.1 to 0.7 MPa 0.2 MPa setting 0.05 to 0.2 MPa	
Ambient and fluid temperature		-5 to 60°C (No freezing)	
Construction		Relieving type	
Weight (kg)		0.015	0.016
Cracking pressure (Valve)		0.02 MPa	
Max. effective area (OUT → IN)		1.8 mm ²	
Applicable tubing material Note)		Nylon, Soft nylon, Polyurethane	

Note) Be sure to note the maximum operating pressure for soft nylon and polyurethane.
(Refer to Best Pneumatics Vol. 15.)

Accessory (Option)/Part No.

Description	Part no.
Manifold base	ARJM10-4, -6, -10

How to Order

ARJ 10 20 F — M5 — 04 — 1

• Miniature regulator

Body size
10 M5

• Port size

M5 M5 × 0.8

• With One-touch fitting

Piping
20 Elbow type

• Option

1 0.2 MPa setting

Note 1) Compared with standard specifications, its adjusting spring has only been changed. It is not the product which does not allow the pressure more than 0.2 MPa. Adjusting spring is not replaceable.

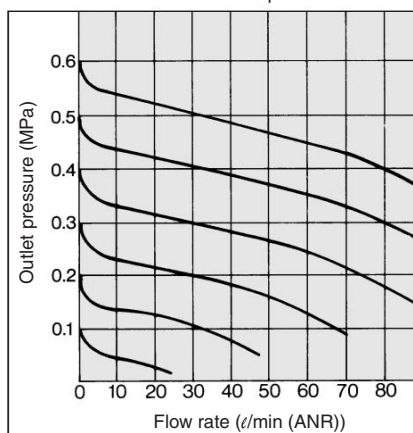
• Applicable tubing O.D.

04 4 mm

06 6 mm

Flow Characteristics

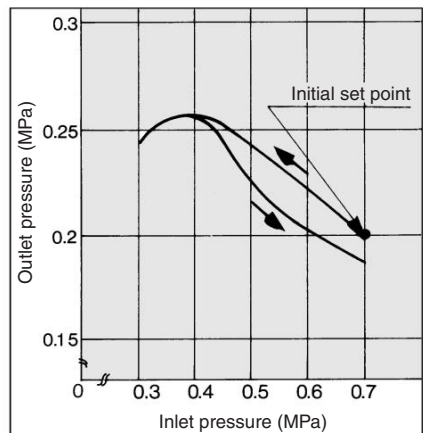
Inlet pressure: 0.7 MPa

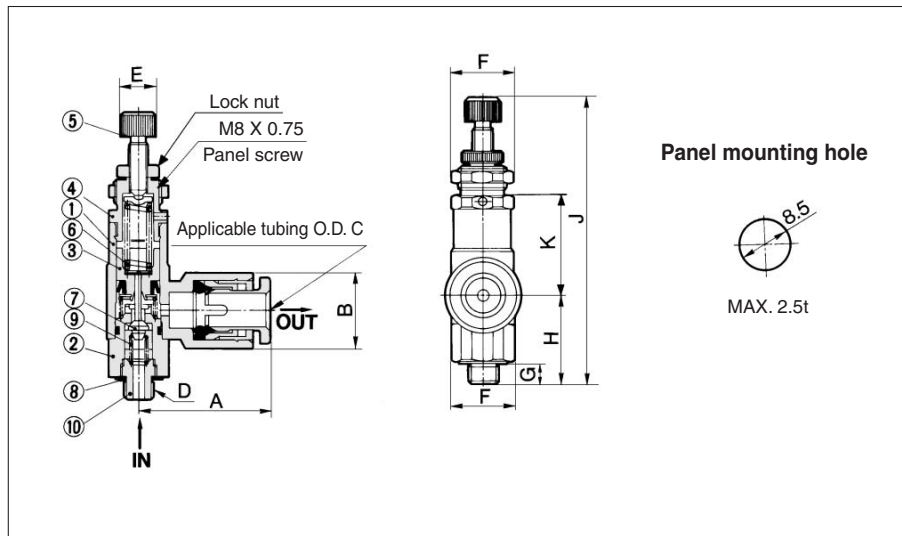


Pressure Characteristics

Conditions (Initial setting)
Inlet pressure: 0.7 MPa
Outlet pressure: 0.2 MPa

Flow rate: 10 ℓ/min (ANR)



Construction/Dimensions**Component Parts**

No.	Description	Material	Note
①	Body	PBT	
②	Valve guide	Brass	Electroless nickel plated
③	Piston	Polyacetal	
④	Bonnet	Brass	Electroless nickel plated
⑤	Handle	Brass	Electroless nickel plated
⑥	Adjusting spring	Steel wire	Zinc chromated
⑦	Valve	Brass	Rubber lining
⑩	Nipple	Brass	Electroless nickel plated

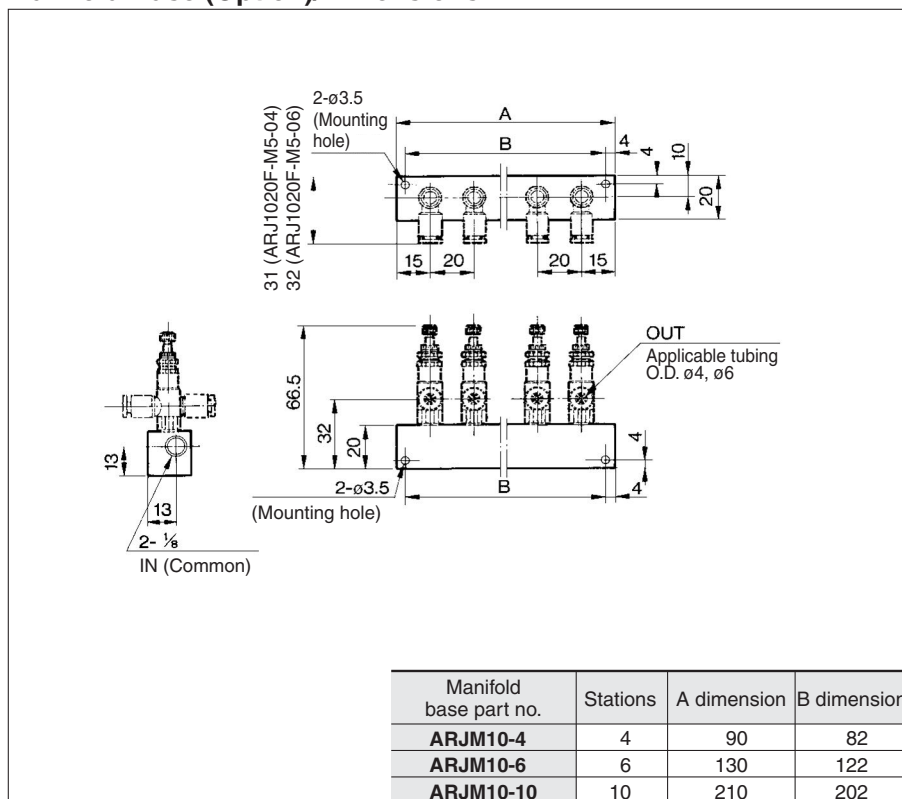
Replacement Parts

No.	Description	Material	Part no.
⑦	Valve	Brass, HNBR	13434-30
⑧	Gasket	Stainless steel NBR	P233014-04
⑨	Spring	Stainless steel	134313

* When replacing valves and springs, remove nipple first. Note that adhesive is applied to the nipple portion.

Dimensions

Model	A	B	C	D	E	F	G	H	J	K
ARJ1020F-M5-04	21	10.4	4		M5 x 0.8	6	10.6 (Width across flats: 10)	3.5	15.5	50
ARJ1020F-M5-06	22	12.8	6							17.2

Manifold Base (Option)/Dimensions**Precautions**

Be sure to read before handling.
Refer to pages 14-21-3 to 14-21-4
for Safety Instructions and
Common Precautions.

Piping**Warning**

- To connect the IN side, hold the valve guide at its wrench flats (opposite side 10) and tighten it at the recommended torque of 1.5 to 2 N·m. Excessive torque or holding it at an area other than the specified portion may result in a malfunction.
- While piping to products or operating the handle, ensure that an excess bending moment should not be applied to a product, because it may result in damage.

Mounting/Adjustment**Warning**

- Set up the regulator while verifying the pressure that is indicated on the inlet and the outlet pressure gauges. Turning the handle excessively could damage the internal parts.

Caution

- Release the lock to adjust the pressure. After the adjustment, engage the lock. Failure to observe this procedure could damage the handle or cause the outlet pressure to fluctuate.
<Lock operating method>
Loosen the lock nut to unlock it, and tighten it to lock it.
- This product cannot be used as a check regulator by installing it between solenoid valve and actuator.

F.R.L.
AV
AU
AF
AR
IR
VEX
AMR
ITV
IC
VBA
VE
VY1
G
PPA
AL

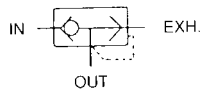
Quick Exhaust Valve with One-touch Fittings Series AQ240F/340F



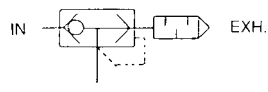
With exhaust port fitting

With silencer

JIS Symbol

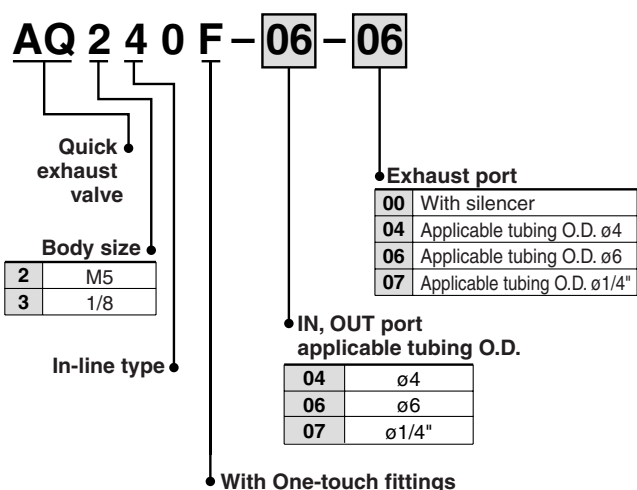


With exhaust port fitting



With silencer

How to Order



Note) Brass parts are all electroless nickel plated.

⚠ Specific Product Precautions

Be sure to read before handling.
Refer to front matters 58 and 59 for Safety Instructions and pages 412 to 414 for Flow Control Equipment Precautions.

Design/Selection

⚠ Caution

1. In the following cases, insufficient exhaust or vibration may cause noise.
 - (a) With residual pressure or back pressure on the IN side.
 - (b) When the differential pressure between the IN and OUT sides is smaller than the minimum operating pressure.
 - (c) When the effective area of the IN side piping of AQ, or the solenoid valve, is smaller than AQ.

Space-saving

Rectilinear IN-OUT tubing connections

- With One-touch fittings and silencer
- With silencer
- Lightweight (Resin body)

Specifications

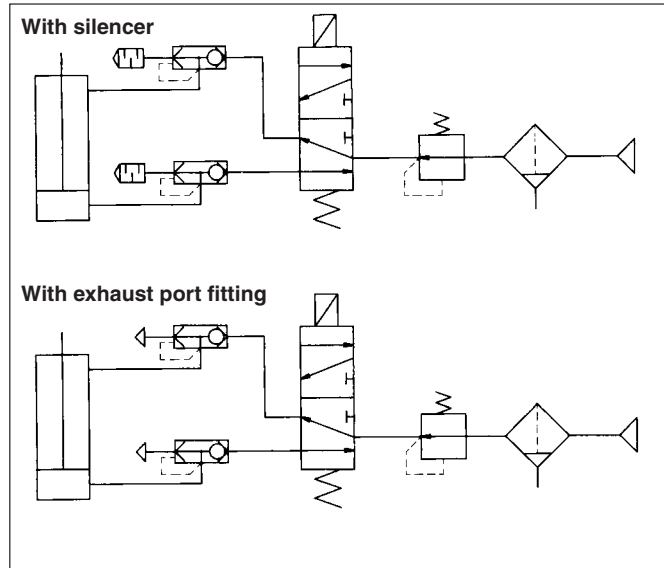
Fluid	Air			
Proof pressure	1.5 MPa			
Max. operating pressure	1 MPa			
Min. operating pressure	0.1 MPa			
Ambient and fluid temperature	-5 to 60°C (No freezing)			
Applicable tubing material ⁽¹⁾	Nylon, Soft nylon, Polyurethane			

Note 1) Use caution regarding the max. operating pressure when soft nylon or polyurethane tubing is used. (Refer to pages 371 and 372 for details.)

Model

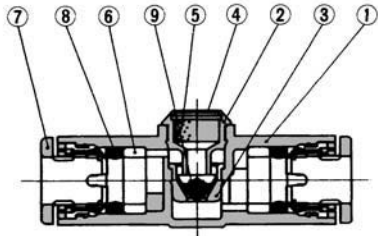
Model	Applicable tubing O.D.			Effective area (mm ²)	
	4	6	1/4"	IN→OUT	OUT→EXH.
AQ240F-04-□	●			1.7	2.5
AQ240F-06-□		●		2.4	2.7
AQ340F-06-□		●		4	4
AQ240F-07-□			●	2.4	2.7
AQ340F-07-□			●	4	4

Circuit

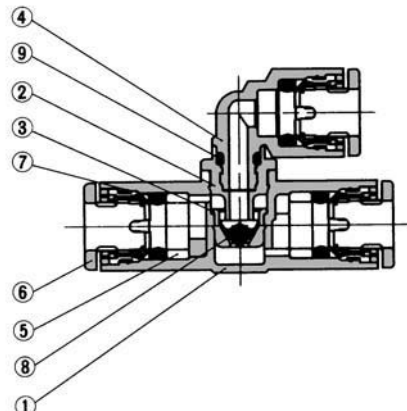


Construction

With silencer



With exhaust port fitting

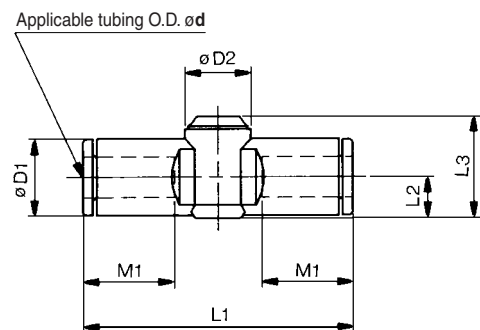


No.	Description	Material	Note
1	Body A	PBT	
2	Seat ring	Brass	Electroless nickel plated
3	Valve seat	Brass	Electroless nickel plated
4	Silencer cover	Stainless steel 304	
5	Silencer	PVA sponge	
6	Spacer	POM	
7	Cassette	—	
8	Seal	NBR	
9	Valve	HNBR	

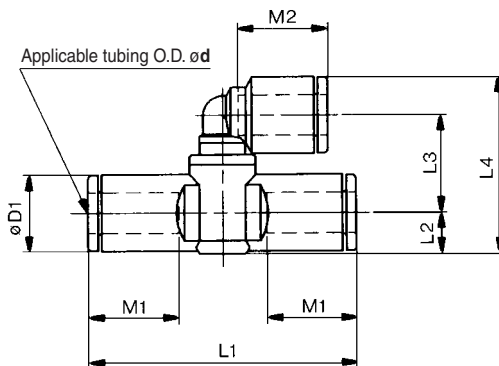
No.	Description	Material	Note
1	Body A	PBT	
2	Seat ring	Brass	Electroless nickel plated
3	Valve seat	Brass	Electroless nickel plated
4	Elbow union body	POM	
5	Spacer	POM	
6	Cassette	—	
7	Seal	NBR	
8	Valve	HNBR	
9	O-ring	NBR	

Dimensions

With silencer



With exhaust port fitting



Model	Tubing O.D. \varnothing d	D1	D2	L1	L2	L3	M1	Weight (g)
AQ240F-04-00	4	9.3	10.0	39.2	5.2	14.3	12.9	5
AQ240F-06-00	6	11.6	10.0	40.7	6.2	15.4	13.7	6
AQ340F-06-00	6	11.6	11.8	44.8	6.3	19.5	13.7	11
AQ240F-07-00	1/4"	12	10.0	40.7	6.2	15.4	13.7	6
AQ340F-07-00	1/4"	13.2	11.8	52.2	7.1	20.3	16.8	11

Model	Tubing O.D. \varnothing d	D1	L1	L2	L3	L4	M1	M2	Weight (g)
AQ240F-04-04	4	9.3	39.2	5.2	13.7	23.5	12.9	12.9	6
AQ240F-06-06	6	11.6	40.7	6.2	14.7	26.7	13.7	13.7	8
AQ340F-06-06	6	11.6	44.8	6.3	19.6	31.7	13.7	13.7	13
AQ240F-07-07	1/4"	12	40.7	6.2	15.1	27.3	13.7	13.7	8
AQ340F-07-07	1/4"	13.2	52.2	7.1	20.0	33.1	16.8	13.7	13

AS

ASP

ASN

AQ

ASV

AK

VCHC

ASS

ASR

ASQ

KE

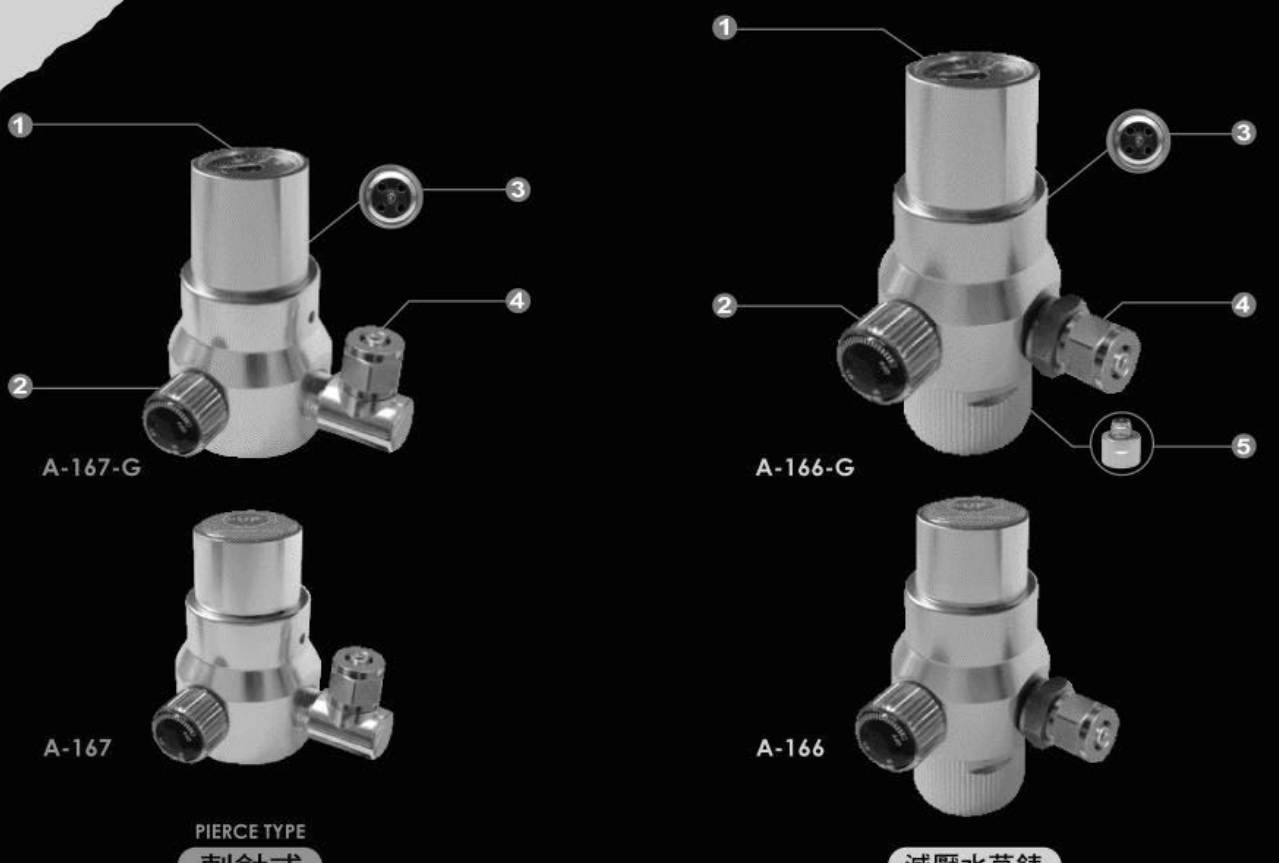
TMH



www.up-aqua.com

CO₂ REGULATOR

DECOMPRESS PRESSURE DESIGNED



PIERCE TYPE

刺針式

PATENT DESIGNED

DECOMPRESS PRESSURE DESIGNED

① Working pressure gauge

② Flow adjustment needle valve

③ Over-pressure valve

④ CO₂ line connection

⑤ Connector

① 工作壓力計

② 微調閥

③ 洩壓閥

④ 洩壓閥

⑤ 轉接頭(可拆卸)

OPTIONAL
選購配件



Solenoid
valve set
電磁閥控制組



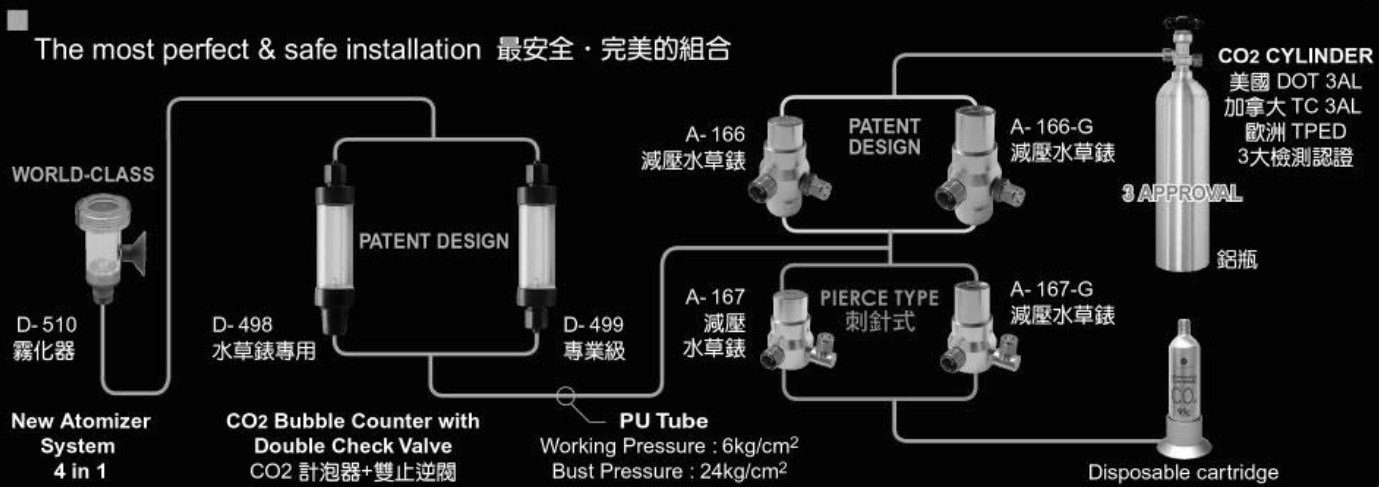
減壓水草錶

PATENT DESIGNED

DECOMPRESS PRESSURE DESIGNED

PATENT DESIGNED

The most perfect & safe installation 最安全 · 完美的組合



ADVANTAGE

- Designed with decompress pressure gate, easily to adjust, stable and accurate CO₂ output.
- To change the connector, the regulator can be used on different specification of CO₂ cylinder.
- Tool-free installation.

優點

- 減壓閥設計，輸出更穩定。
- 水草錶更換轉接頭，可配合不同規格CO₂瓶使用。
- 安裝時，不需使用工具。



上鴻實業有限公司
UP AQUARIUM SUPPLY INDUSTRIES CO., LTD.

MP: +86 13570055062 黃小姐

TEL : 886-2-22967988 FAX: 886-2-22977375

<http://www.up-aqua.com> e-mail : service@up-aqua.com



SOLD OUT

Luft Mini CO2 Bike Tire Inflator - Red + Black

★★★★★ (0 reviews)

SKU: 163766 (Added on 11/2/2012)

Price: US\$ 15.39

Shipping: Free Shipping To GERMANY

Dispatch: Item is temporarily sold out.

Quantity: (Sold out)[ADD TO CART](#)[Add to wish list](#)

Price Match

100% Satisfaction guaranteed

Report Error

[Product Details](#)[Reviews](#)[Discussions](#)[Overview](#)[Specifications](#)[Buy 3+ and Save](#)[Reviews](#)**Brand**

Luft

Quantity

1

Color

Red + black + golden

Material

Plastic + stainless steel

Functions

Automatically fast air inflation

Best Use

Suitable for mountainous region and cross-country

Other Features

Fits Presta and Schrader valves without adapters; Includes 16g threaded CO2 cartridges and insulator sleeve

Packing List

1 x CO2 inflation Devices

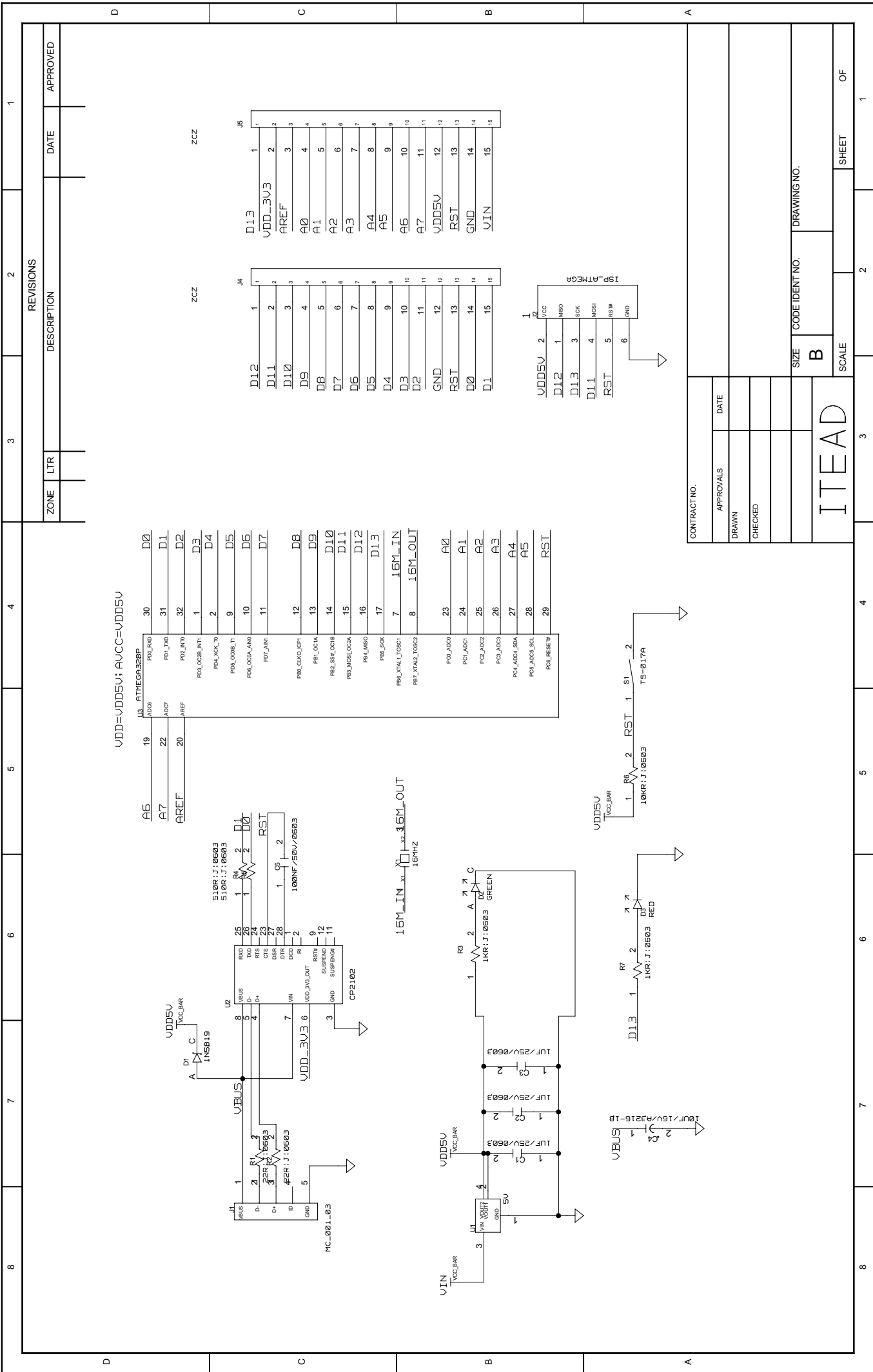
1 x CO2 cartridge

1 x Insulator sleeve

1 x English user manual

Dimensions: 3.54 in x 1.06 in x 1.06 in (9.0 cm x 2.7 cm x 2.7 cm)

Weight: 3.60 oz (102 g)





November 2013

FQP30N06L

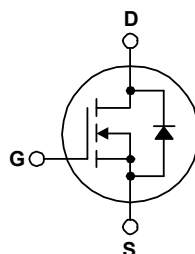
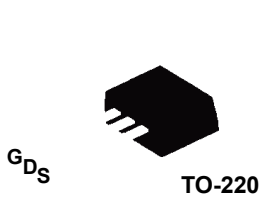
N-Channel QFET® MOSFET 60 V, 32 A, 35 mΩ

Description

This N-Channel enhancement mode power MOSFET is produced using Fairchild Semiconductor's proprietary planar stripe and DMOS technology. This advanced MOSFET technology has been especially tailored to reduce on-state resistance, and to provide superior switching performance and high avalanche energy strength. These devices are suitable for switched mode power supplies, audio amplifier, DC motor control, and variable switching power applications.

Features

- 32 A, 60 V, $R_{DS(on)} = 35 \text{ m}\Omega$ (Max.) @ $V_{GS} = 10 \text{ V}$, $I_D = 16 \text{ A}$
- Low Gate Charge (Typ. 15 nC)
- Low C_{rss} (Typ. 50 pF)
- 100% Avalanche Tested
- 175°C Maximum Junction Temperature Rating



Absolute Maximum Ratings

 $T_C = 25^\circ\text{C}$ unless otherwise noted.

Symbol	Parameter	FQP30N06L	Unit
V_{DSS}	Drain-Source Voltage	60	V
I_D	Drain Current - Continuous ($T_C = 25^\circ\text{C}$)	32	A
	- Continuous ($T_C = 100^\circ\text{C}$)	22.6	A
I_{DM}	Drain Current - Pulsed	(Note 1)	A
V_{GSS}	Gate-Source Voltage	± 20	V
E_{AS}	Single Pulsed Avalanche Energy	(Note 2)	mJ
I_{AR}	Avalanche Current	(Note 1)	A
E_{AR}	Repetitive Avalanche Energy	(Note 1)	mJ
dv/dt	Peak Diode Recovery dv/dt	(Note 3)	V/ns
P_D	Power Dissipation ($T_C = 25^\circ\text{C}$)	79	W
	- Derate above 25°C	0.53	W/°C
T_J, T_{STG}	Operating and Storage Temperature Range	-55 to +175	°C
T_L	Maximum Lead Temperature for Soldering, 1/8" from Case for 5 seconds	300	°C

Thermal Characteristics

Symbol	Parameter	FQP30N06L	Unit
$R_{\theta JC}$	Thermal Resistance, Junction-to-Case, Max.	1.90	°C/W
$R_{\theta JA}$	Thermal Resistance, Junction-to-Ambient, Max.	62.5	°C/W

Package Marking and Ordering Information

Part Number	Top Mark	Package	Packing Method	Reel Size	Tape Width	Quantity
FQP30N06L	FQP30N06L	TO-220	Tube	N/A	N/A	50 units

Electrical Characteristics

$T_C = 25^\circ\text{C}$ unless otherwise noted.

Symbol	Parameter	Test Conditions	Min	Typ	Max	Unit
Off Characteristics						
BV_{DSS}	Drain-Source Breakdown Voltage	$V_{GS} = 0 \text{ V}, I_D = 250 \mu\text{A}$	60	--	--	V
$\Delta BV_{DSS} / \Delta T_J$	Breakdown Voltage Temperature Coefficient	$I_D = 250 \mu\text{A}$, Referenced to 25°C	--	0.06	--	$\text{V}/^\circ\text{C}$
I_{DSS}	Zero Gate Voltage Drain Current	$V_{DS} = 60 \text{ V}, V_{GS} = 0 \text{ V}$	--	--	1	μA
		$V_{DS} = 48 \text{ V}, T_C = 150^\circ\text{C}$	--	--	10	μA
I_{GSSF}	Gate-Body Leakage Current, Forward	$V_{GS} = 20 \text{ V}, V_{DS} = 0 \text{ V}$	--	--	100	nA
I_{GSSR}	Gate-Body Leakage Current, Reverse	$V_{GS} = -20 \text{ V}, V_{DS} = 0 \text{ V}$	--	--	-100	nA

On Characteristics

$V_{GS(\text{th})}$	Gate Threshold Voltage	$V_{DS} = V_{GS}, I_D = 250 \mu\text{A}$	1.0	--	2.5	V
$R_{DS(\text{on})}$	Static Drain-Source On-Resistance	$V_{GS} = 10 \text{ V}, I_D = 16 \text{ A}$ $V_{GS} = 5 \text{ V}, I_D = 16 \text{ A}$	--	0.027	0.035	Ω
g_{FS}	Forward Transconductance	$V_{DS} = 25 \text{ V}, I_D = 16 \text{ A}$	--	24	--	s

Dynamic Characteristics

C_{iss}	Input Capacitance	$V_{DS} = 25 \text{ V}, V_{GS} = 0 \text{ V}, f = 1.0 \text{ MHz}$	--	800	1040	pF
C_{oss}	Output Capacitance		--	270	350	pF
C_{rss}	Reverse Transfer Capacitance		--	50	65	pF

Switching Characteristics

$t_{d(on)}$	Turn-On Delay Time	$V_{DD} = 30 \text{ V}, I_D = 16 \text{ A}, R_G = 25 \Omega$	--	15	40	ns
t_r	Turn-On Rise Time		--	210	430	ns
$t_{d(off)}$	Turn-Off Delay Time		--	60	130	ns
t_f	Turn-Off Fall Time		--	110	230	ns
Q_g	Total Gate Charge	$V_{DS} = 48 \text{ V}, I_D = 32 \text{ A}, V_{GS} = 5 \text{ V}$	--	15	20	nC
Q_{gs}	Gate-Source Charge		--	3.5	--	nC
Q_{gd}	Gate-Drain Charge		--	8.5	--	nC

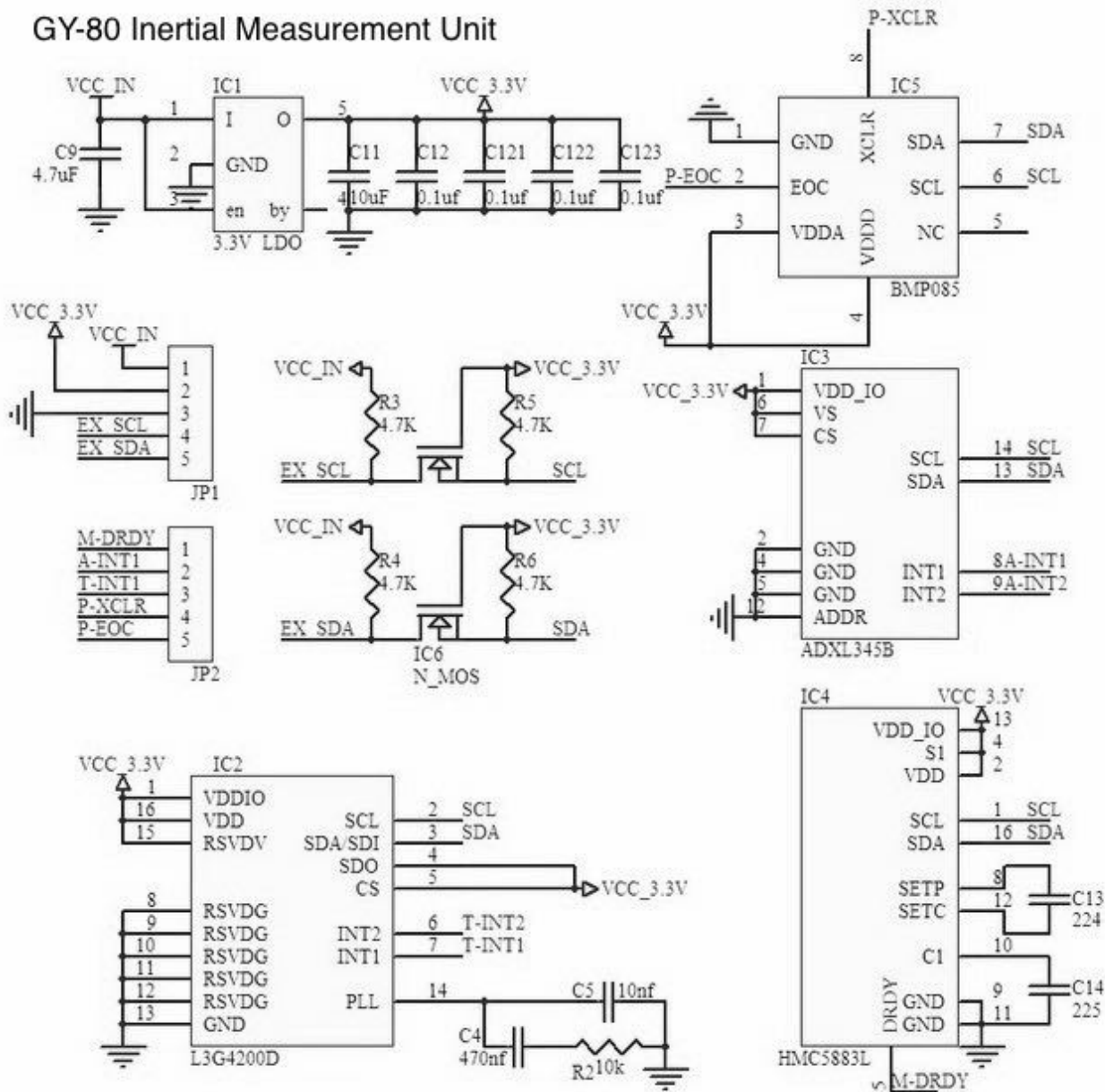
Drain-Source Diode Characteristics and Maximum Ratings

I_S	Maximum Continuous Drain-Source Diode Forward Current	--	--	32	A
I_{SM}	Maximum Pulsed Drain-Source Diode Forward Current	--	--	128	A
V_{SD}	Drain-Source Diode Forward Voltage	$V_{GS} = 0 \text{ V}, I_S = 32 \text{ A}$	--	--	1.5
t_{rr}	Reverse Recovery Time	$V_{GS} = 0 \text{ V}, I_S = 32 \text{ A}, dI_F / dt = 100 \text{ A}/\mu\text{s}$	--	60	--
Q_{rr}	Reverse Recovery Charge		--	90	--

Notes:

1. Repetitive Rating : Pulse width limited by maximum junction temperature.
2. $L = 400 \mu\text{H}, I_{AS} = 32 \text{ A}, V_{DD} = 25 \text{ V}, R_G = 25 \Omega$, starting $T_J = 25^\circ\text{C}$.
3. $I_{SD} \leq 32 \text{ A}, di/dt \leq 300 \text{ A}/\mu\text{s}, V_{DD} \leq BV_{DSS}$, starting $T_J = 25^\circ\text{C}$.
4. Essentially independent of operating temperature.

GY-80 Inertial Measurement Unit



合格证书
CERTIFICATE

检 验 结 果

Testing Report

型 号 规 格: CHHBS
 (Model & Specification)
 编 号: 13121203
 准 确 度 级 别: 0.05%F.S
 (Accuracy Scale)
 检 验 日 期: 2013.9.18
 (Test Date)
 检 验 员: 石家庄触达科技有限责任公司
 (Checker)

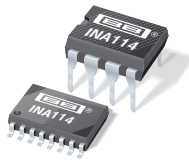
- 我们保证本产品的性能指标满足有关计量范围的要求，标定地点在河北石家庄，重力加速度为9.81m/s²。
- 改变电缆线长度会影响传感器性能。

石家庄触达科技有限责任公司

量程(Rated Load): 3000g		温度: 25°
输出灵敏度过	S	1.514mV/V
Reted Output	L	±0.05%F.S
线性	H	±0.05%F.S
滞后	R	±0.05%F.S
Hysteresis	Z	±0.05%F.S
重复性	Zt	±0.05%F.S
零点输出	Creep(30min)	±0.05%F.S/30min
Zero Balance	Input Impedance	380 ± 10 Ω
零点温度影响	Output Impedance	350 Ω
Tempeature Effect On Zero	绝缘阻抗	≥ 5000 MΩ
蠕变	Insulation	温度范围
Creep(30min)		-30° ~ 70°
输入阻抗	安全超载	
Input Impedance	Aafe Overload	150 %
输出阻抗	输入端	黑
Output Impedance	Output End	Exc -
绝缘阻抗	输出端	绿
Insulation	Output End	白
温度范围	激励电压	卡 Sig -
Tempetature Range	Excitation Votage	5-12(建议 10) VDC

保 修 卡

产品自销售之日起3月之内,在用户遵守使用规则的条件下,出现非人为故障,本公司凭此卡负责保修!
 石家庄触达科技有限责任公司
 Te: 0311-67507331
 网址: www.cd669.com

**INA114**

Precision INSTRUMENTATION AMPLIFIER

FEATURES

- LOW OFFSET VOLTAGE: $50\mu\text{V}$ max
- LOW DRIFT: $0.25\mu\text{V}/^\circ\text{C}$ max
- LOW INPUT BIAS CURRENT: 2nA max
- HIGH COMMON-MODE REJECTION: 115dB min
- INPUT OVER-VOLTAGE PROTECTION: $\pm 40\text{V}$
- WIDE SUPPLY RANGE: ± 2.25 to $\pm 18\text{V}$
- LOW QUIESCENT CURRENT: 3mA max
- 8-PIN PLASTIC AND SOL-16

APPLICATIONS

- BRIDGE AMPLIFIER
- THERMOCOUPLE AMPLIFIER
- RTD SENSOR AMPLIFIER
- MEDICAL INSTRUMENTATION
- DATA ACQUISITION

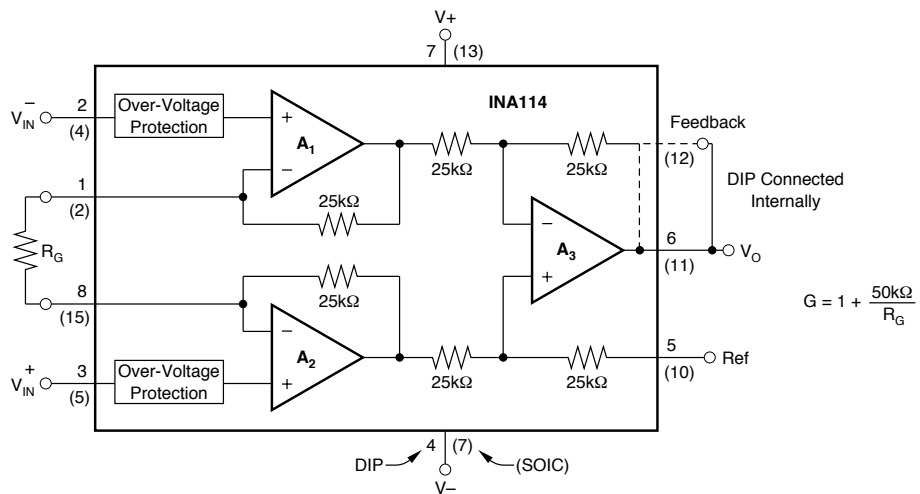
DESCRIPTION

The INA114 is a low cost, general purpose instrumentation amplifier offering excellent accuracy. Its versatile 3-op amp design and small size make it ideal for a wide range of applications.

A single external resistor sets any gain from 1 to 10,000. Internal input protection can withstand up to $\pm 40\text{V}$ without damage.

The INA114 is laser trimmed for very low offset voltage ($50\mu\text{V}$), drift ($0.25\mu\text{V}/^\circ\text{C}$) and high common-mode rejection (115dB at $G = 1000$). It operates with power supplies as low as $\pm 2.25\text{V}$, allowing use in battery operated and single 5V supply systems. Quiescent current is 3mA maximum.

The INA114 is available in 8-pin plastic and SOL-16 surface-mount packages. Both are specified for the -40°C to $+85^\circ\text{C}$ temperature range.



International Airport Industrial Park • Mailing Address: PO Box 11400, Tucson, AZ 85734 • Street Address: 6730 S. Tucson Blvd., Tucson, AZ 85706 • Tel: (520) 746-1111 • Twx: 910-952-1111
Internet: <http://www.burr-brown.com/> • FAXLine: (800) 548-6133 (US/Canada Only) • Cable: BBRCORP • Telex: 066-6491 • FAX: (520) 889-1510 • Immediate Product Info: (800) 548-6132

SPECIFICATIONS

ELECTRICAL

At $T_A = +25^\circ\text{C}$, $V_S = \pm 15\text{V}$, $R_L = 2\text{k}\Omega$, unless otherwise noted.

PARAMETER	CONDITIONS	INA114BP, BU			INA114AP, AU			UNITS
		MIN	TYP	MAX	MIN	TYP	MAX	
INPUT								
Offset Voltage, RTI Initial vs Temperature vs Power Supply Long-Term Stability Impedance, Differential Common-Mode Input Common-Mode Range Safe Input Voltage Common-Mode Rejection	$T_A = +25^\circ\text{C}$ $T_A = T_{\text{MIN}} \text{ to } T_{\text{MAX}}$ $V_S = \pm 2.25\text{V} \text{ to } \pm 18\text{V}$ $V_{\text{CM}} = \pm 10\text{V}, \Delta R_S = 1\text{k}\Omega$ $G = 1$ $G = 10$ $G = 100$ $G = 1000$	± 11	$\pm 10 + 20/G$ $\pm 0.1 + 0.5/G$ $0.5 + 2/G$ $\pm 0.2 + 0.5/G$ $10^{10} \text{ II } 6$ $10^{10} \text{ II } 6$ ± 13.5	$\pm 50 + 100/G$ $\pm 0.25 + 5/G$ $3 + 10/G$	$\pm 25 + 30/G$ $\pm 0.25 + 5/G$ *	$\pm 125 + 500/G$ $\pm 1 + 10/G$ *	μV $\mu\text{V}/^\circ\text{C}$ $\mu\text{V}/\text{V}$ $\mu\text{V}/\text{mV}$ $\Omega \text{ II } \text{pF}$ $\Omega \text{ II } \text{pF}$ V V	
BIAS CURRENT vs Temperature			± 0.5 ± 8	± 2		*	± 5	nA $\text{pA}/^\circ\text{C}$
OFFSET CURRENT vs Temperature			± 0.5 ± 8	± 2		*	± 5	nA $\text{pA}/^\circ\text{C}$
NOISE VOLTAGE, RTI	$G = 1000, R_S = 0\Omega$		15 11 11 0.4 0.4 0.2 18			*		$\text{nV}/\sqrt{\text{Hz}}$ $\text{nV}/\sqrt{\text{Hz}}$ $\text{nV}/\sqrt{\text{Hz}}$ $\mu\text{Vp-p}$ $\text{pA}/\sqrt{\text{Hz}}$ $\text{pA}/\sqrt{\text{Hz}}$ pAp-p
GAIN								
Gain Equation Range of Gain Gain Error	$G = 1$ $G = 10$ $G = 100$ $G = 1000$	1	$1 + (50\text{k}\Omega/R_G)$ ± 0.01 ± 0.02 ± 0.05 ± 0.5 ± 1 ± 2 ± 25	10000 ± 0.05 ± 0.4 ± 0.5 ± 1 ± 10 ± 100	*	*	*	V/V V/V $\%$ $\%$ $\%$ $\%$ $\%$
Gain vs Temperature 50kΩ Resistance ⁽¹⁾ Nonlinearity	$50\text{k}\Omega$ $50\text{k}\Omega$ $50\text{k}\Omega$ $50\text{k}\Omega$	$G = 1$ $G = 10$ $G = 100$ $G = 1000$	± 0.0001 ± 0.0005 ± 0.0005 ± 0.002	± 0.001 ± 0.002 ± 0.002 ± 0.01		*	± 0.002 ± 0.004 ± 0.004 ± 0.02	$\text{ppm}/^\circ\text{C}$ $\text{ppm}/^\circ\text{C}$ $\%$ of FSR $\%$ of FSR
OUTPUT								
Voltage	$I_O = 5\text{mA}, T_{\text{MIN}} \text{ to } T_{\text{MAX}}$ $V_S = \pm 11.4\text{V}, R_L = 2\text{k}\Omega$ $V_S = \pm 2.25\text{V}, R_L = 2\text{k}\Omega$	± 13.5 ± 10 ± 1	± 13.7 ± 10.5 ± 1.5 1000 $+20/-15$		*	*		V V V pF mA
Load Capacitance Stability Short Circuit Current						*		
FREQUENCY RESPONSE								
Bandwidth, -3dB	$G = 1$ $G = 10$ $G = 100$ $G = 1000$		1 100 10 1			*		MHz kHz kHz kHz
Slew Rate Settling Time, 0.01%	$V_O = \pm 10\text{V}, G = 10$ $G = 1$ $G = 10$ $G = 100$ $G = 1000$	0.3	0.6 18 20 120 1100 20		*	*		$\text{V}/\mu\text{s}$ μs μs μs μs μs
Overload Recovery	50% Overdrive					*		
POWER SUPPLY								
Voltage Range Current	$V_{\text{IN}} = 0\text{V}$	± 2.25	± 15 ± 2.2	± 18 ± 3	*	*	*	V mA
TEMPERATURE RANGE								
Specification Operating θ_{JA}		-40 -40	80	85 125	*		*	$^\circ\text{C}$ $^\circ\text{C}$ $^\circ\text{C}/\text{W}$

* Specification same as INA114BP/BU.

NOTE: (1) Temperature coefficient of the "50kΩ" term in the gain equation.

The information provided herein is believed to be reliable; however, BURR-BROWN assumes no responsibility for inaccuracies or omissions. BURR-BROWN assumes no responsibility for the use of this information, and all use of such information shall be entirely at the user's own risk. Prices and specifications are subject to change without notice. No patent rights or licenses to any of the circuits described herein are implied or granted to any third party. BURR-BROWN does not authorize or warrant any BURR-BROWN product for use in life support devices and/or systems.

FAIRCHILD

SEMICONDUCTOR®

August 2013

LM78XX / LM78XXA

3-Terminal 1 A Positive Voltage Regulator

Features

- Output Current up to 1 A
- Output Voltages: 5, 6, 8, 9, 10, 12, 15, 18, 24 V
- Thermal Overload Protection
- Short-Circuit Protection
- Output Transistor Safe Operating Area Protection

Description

The LM78XX series of three-terminal positive regulators is available in the TO-220 package and with several fixed output voltages, making them useful in a wide range of applications. Each type employs internal current limiting, thermal shut-down, and safe operating area protection. If adequate heat sinking is provided, they can deliver over 1 A output current. Although designed primarily as fixed-voltage regulators, these devices can be used with external components for adjustable voltages and currents.



Ordering Information⁽¹⁾

Product Number	Output Voltage Tolerance	Package	Operating Temperature	Packing Method	
LM7805CT	$\pm 4\%$	TO-220 (Single Gauge)	-40°C to $+125^{\circ}\text{C}$	Rail	
LM7806CT					
LM7808CT					
LM7809CT					
LM7810CT					
LM7812CT					
LM7815CT					
LM7818CT					
LM7824CT					
LM7805ACT			0°C to $+125^{\circ}\text{C}$		
LM7809ACT					
LM7810ACT					
LM7812ACT					
LM7815ACT					

Note:

1. Above output voltage tolerance is available at 25°C .

Block Diagram

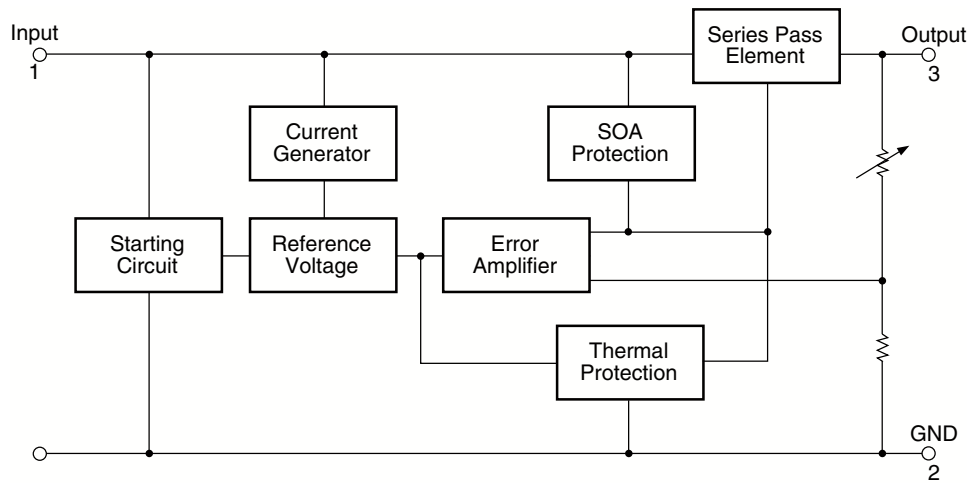


Figure 1. Block Diagram

Absolute Maximum Ratings

Stresses exceeding the absolute maximum ratings may damage the device. The device may not function or be operable above the recommended operating conditions and stressing the parts to these levels is not recommended. In addition, extended exposure to stresses above the recommended operating conditions may affect device reliability. The absolute maximum ratings are stress ratings only. Values are at $T_A = 25^\circ\text{C}$ unless otherwise noted.

Symbol	Parameter	Value	Unit
V_I	Input Voltage	$V_O = 5 \text{ V to } 18 \text{ V}$	35
		$V_O = 24 \text{ V}$	40
$R_{\theta\text{JC}}$	Thermal Resistance, Junction-Case (TO-220)	5	$^\circ\text{C/W}$
$R_{\theta\text{JA}}$	Thermal Resistance, Junction-Air (TO-220)	65	$^\circ\text{C/W}$
T_{OPR}	Operating Temperature Range	LM78xx	-40 to +125
		LM78xxA	0 to +125
T_{STG}	Storage Temperature Range	-65 to +150	$^\circ\text{C}$

Electrical Characteristics (LM7805)

Refer to the test circuit, $-40^{\circ}\text{C} < T_J < 125^{\circ}\text{C}$, $I_O = 500 \text{ mA}$, $V_I = 10 \text{ V}$, $C_I = 0.1 \mu\text{F}$, unless otherwise specified.

Symbol	Parameter	Conditions		Min.	Typ.	Max.	Unit
V_O	Output Voltage	$T_J = +25^{\circ}\text{C}$		4.80	5.00	5.20	V
		$I_O = 5 \text{ mA to } 1 \text{ A}$, $P_O \leq 15 \text{ W}$, $V_I = 7 \text{ V to } 20 \text{ V}$		4.75	5.00	5.25	
Regline	Line Regulation ⁽²⁾	$T_J = +25^{\circ}\text{C}$	$V_I = 7 \text{ V to } 25 \text{ V}$		4.0	100.0	mV
			$V_I = 8 \text{ V to } 12 \text{ V}$		1.6	50.0	
Regload	Load Regulation ⁽²⁾	$T_J = +25^{\circ}\text{C}$	$I_O = 5 \text{ mA to } 1.5 \text{ A}$		9.0	100.0	mV
			$I_O = 250 \text{ mA to } 750 \text{ mA}$		4.0	50.0	
I_Q	Quiescent Current	$T_J = +25^{\circ}\text{C}$			5.0	8.0	mA
ΔI_Q	Quiescent Current Change	$I_O = 5 \text{ mA to } 1 \text{ A}$			0.03	0.50	mA
		$V_I = 7 \text{ V to } 25 \text{ V}$			0.30	1.30	
$\Delta V_O/\Delta T$	Output Voltage Drift ⁽³⁾	$I_O = 5 \text{ mA}$			-0.8		mV/ $^{\circ}\text{C}$
V_N	Output Noise Voltage	$f = 10 \text{ Hz to } 100 \text{ kHz}$, $T_A = +25^{\circ}\text{C}$			42.0		$\mu\text{V}/V_O$
RR	Ripple Rejection ⁽³⁾	$f = 120 \text{ Hz}$, $V_I = 8 \text{ V to } 18 \text{ V}$		62.0	73.0		dB
V_{DROP}	Dropout Voltage	$T_J = +25^{\circ}\text{C}$, $I_O = 1 \text{ A}$			2.0		V
R_O	Output Resistance ⁽³⁾	$f = 1 \text{ kHz}$			15.0		$\text{m}\Omega$
I_{SC}	Short-Circuit Current	$T_J = +25^{\circ}\text{C}$, $V_I = 35 \text{ V}$			230		mA
I_{PK}	Peak Current ⁽³⁾	$T_J = +25^{\circ}\text{C}$			2.2		A

Notes:

2. Load and line regulation are specified at constant junction temperature. Changes in V_O due to heating effects must be taken into account separately. Pulse testing with low duty is used.
3. These parameters, although guaranteed, are not 100% tested in production.

Electrical Characteristics (LM7812)

Refer to the test circuit, $-40^{\circ}\text{C} < T_J < 125^{\circ}\text{C}$, $I_O = 500 \text{ mA}$, $V_I = 19 \text{ V}$, $C_I = 0.33 \mu\text{F}$, $C_O = 0.1 \mu\text{F}$, unless otherwise specified.

Symbol	Parameter	Conditions		Min.	Typ.	Max.	Unit
V_O	Output Voltage	$T_J = +25^{\circ}\text{C}$		11.5	12.0	12.5	V
		$I_O = 5 \text{ mA to } 1 \text{ A}$, $P_O \leq 15 \text{ W}$, $V_I = 14.5 \text{ V to } 27 \text{ V}$		11.4	12.0	12.6	
Regline	Line Regulation ⁽¹²⁾	$T_J = +25^{\circ}\text{C}$	$V_I = 14.5 \text{ V to } 30 \text{ V}$		10	240	mV
			$V_I = 16 \text{ V to } 22 \text{ V}$		3	120	
Regload	Load Regulation ⁽¹²⁾	$T_J = +25^{\circ}\text{C}$	$I_O = 5 \text{ mA to } 1.5 \text{ A}$		11	240	mV
			$I_O = 250 \text{ mA to } 750 \text{ mA}$		5	120	
I_Q	Quiescent Current	$T_J = +25^{\circ}\text{C}$			5.1	8.0	mA
ΔI_Q	Quiescent Current Change	$I_O = 5 \text{ mA to } 1 \text{ A}$			0.1	0.5	mA
		$V_I = 14.5 \text{ V to } 30 \text{ V}$			0.5	1.0	
$\Delta V_O/\Delta T$	Output Voltage Drift ⁽¹³⁾	$I_O = 5 \text{ mA}$			-1.0		mV/ $^{\circ}\text{C}$
V_N	Output Noise Voltage	$f = 10 \text{ Hz to } 100 \text{ kHz}$, $T_A = +25^{\circ}\text{C}$			76.0		$\mu\text{V}/V_O$
RR	Ripple Rejection ⁽¹³⁾	$f = 120 \text{ Hz}$, $V_I = 15 \text{ V to } 25 \text{ V}$		55.0	71.0		dB
V_{DROP}	Dropout Voltage	$I_O = 1 \text{ A}$, $T_J = +25^{\circ}\text{C}$			2.0		V
R_O	Output Resistance ⁽¹³⁾	$f = 1 \text{ kHz}$			18.0		$\text{m}\Omega$
I_{SC}	Short-Circuit Current	$V_I = 35 \text{ V}$, $T_J = +25^{\circ}\text{C}$			230		mA
I_{PK}	Peak Current ⁽¹³⁾	$T_J = +25^{\circ}\text{C}$			2.2		A

Notes:

12. Load and line regulation are specified at constant junction temperature. Changes in V_O due to heating effects must be taken into account separately. Pulse testing with low duty is used.
13. These parameters, although guaranteed, are not 100% tested in production.

Bibliography

- [1] J. H. Zhu, B. B. Li, R. T. James, Y. Z. Li, and H. Q. Min, "Design of a wheel-type mobile robot for rough terrain," in *IEEE International Conference on Robotics and Biomimetics*, 2012. 15
- [2] M. F. Silva and J. A. T. Machado, "A historical perspective of legged robots," in *Journal of Vibration and Control*. SAGE, 2007. 15
- [3] Y. Zhou, C. Fu, C. Yun, Z. Yu, and K. Chen, "Control of one-legged robot hopping in place," in *IEEE International Conference on Robotics and Biomimetics*, 2013. 15
- [4] C. Chevallereau, G. Bessonnet, G. Abba, and Y. Aoustin, *Bipedal Robots: Modeling, Design and Walking Synthesis*. Wiley, 2010. 15
- [5] D. W. Hong, "Biologically inspired locomotion strategies: Novel ground mobile robots at romela," in *The 3rd International Conference on Ubiquitous Robots and Ambient Intelligence*, 2006. 15
- [6] M. Raibert, K. Blankenspoor, G. Nelson, and R. Playter, "Bigdog, the rough-terrain quadruped robot," in *Proceedings of the 17th World Congress, The International Federation of Automatic Control*, 2008. 15
- [7] K. Nonami, R. K. Barai, A. Irawan, and M. R. Daud, "Hydraulically actuated hexapod robots," *Intelligent Systems, Control and Automation: Science and Engineering*, vol. 66, pp. 19–40, 2014. 15
- [8] U. Saranli, M. Buehler, and D. E. Koditschek, "Rhex: A simple and highly mobile hexapod robot," in *The International Journal of Robotics Research*. SAGE, 2001, vol. 20, pp. 616–630. 15
- [9] T. Umedachi, V. Vikas, and B. A. Trimmer, "Highly deformable 3-d printed soft robot generating inching and crawling locomotions with variable friction legs," in *IEEE/RSJ International Conference on Intelligent Robots and Systems*, 2013. 15
- [10] B. Klaassen and K. L. Paap, "Gmd-snake2: A snake-like robot driven by wheels and a method for motion control," in *IEEE International Conference on Robotics and Automation*, 1999. 15
- [11] S. Hirai and R. Imuta, "Dynamic simulation of six-strut tensegrity robot rolling," in *IEEE International Conference on Robotics and Biomimetics*, 2012. 15
- [12] R. Armour, K. Paskins, A. Bowyer, J. Vincent, and W. Megill, "Jumping robots: a biomimetic solution to locomotion across rough terrain," in *Bioinspiration and Biomimetics*. IOP, 2007, vol. 2, pp. 65–82. 15
- [13] R. J. Dufresne, W. J. Gerace, and W. J. Leonard, "Springbok: The physics of jumping," in *The Physics Teacher*. AAPT, 2001, vol. 39, pp. 109–115. 15
- [14] M. Wang, X. zhe Zang, J. zhuang Fan, and J. Zhao, "Biological jumping mechanism analysis and modeling for frog robot," in *Journal of Bionic Engineering*. Elsevier, September 2008, vol. 5, no. 3, pp. 181–188. 15
- [15] U. Scarfogliero, C. Stefanini, and P. Dario, "Design and development of the long-jumping "grillo" mini robot," in *IEEE International Conference on Robotics and Automation*, 2007. 15, 16
- [16] "http://www.festo.com/cms/en_corp/13704.htm," *BionicKangaroo*. 15

- [17] U. of Cambridge, “<http://www.cam.ac.uk/research/news/functioning-mechanical-gears-seen-in-nature-for-the-first-time>,” *Functioning mechanical gears seen in nature for the first time*. 15
- [18] M. Burrows and G. Sutton, “Interacting gears synchronize propulsive leg movements in a jumping insect,” *Science Magazine*, vol. 341, no. 6151, pp. 1254–1256, September 2013. 15
- [19] H. Tsukagoshi, M. Sasaki, A. Kitagawa, and T. Tanaka, “Jumping robot for rescue operation with excellent traverse ability,” in *International Conference on Advanced Robotics*, 2005. 15, 16
- [20] K. Kikuchi, K. Sakaguchi, T. Sudo, N. Bushida, Y. Chiba, and Y. Asai, “A study on a wheel-based stair-climbing robot with a hopping mechanism,” in *Mechanical Systems and Signal Processing*. Elsevier, 2008, vol. 22, pp. 1316–1326. 15, 16
- [21] F. Kikuchi, Y. Ota, and S. Hirose, “Basic performance experiments for jumping quadruped,” in *IEEE/RSJ International Conference on Intelligent Robots and Systems*, 2003. 15
- [22] A. M. Johnson and D. E. Koditschek, “Toward a vocabulary of legged leaping,” in *IEEE International Conference on Robotics and Automation*, 2013. 15
- [23] J. Zhao, J. Xu, B. Gao, N. Xi, F. J. Cintrón, M. W. Mutka, and L. Xiao, “Msu jumper: A single-motor-actuated miniature steerable jumping robot,” in *IEEE Transactions on Robotics*, 2013. 15, 16
- [24] U. Scarfogliero, C. Stefanini, and P. Dario, “A bioinspired concept for high efficiency locomotion in micro robots: the jumping robot grillo,” in *IEEE International Conference on Robotics and Automation*, 2006. 15
- [25] M. Kovač, M. Fuchs, A. Guignard, J.-C. Zufferey, and D. Floreano, “A miniature 7g jumping robot,” in *IEEE International Conference on Robotics and Automation*, 2008. 15
- [26] J. Zhao, R. Yang, N. Xi, B. Gao, X. Fan, M. W. Mutka, and L. Xiao, “Development of a miniature self-stabilization jumping robot,” in *IEEE/RSJ International Conference on Intelligent Robots and Systems*, 2009. 15
- [27] M. Kovač, M. Schlegel, J.-C. Zufferey, and D. Floreano, “A miniature jumping robot with self-recovery capabilities,” in *IEEE/RSJ International Conference on Intelligent Robots and Systems*, 2009. 15, 16
- [28] ——, “Steerable miniature jumping robot,” in *Autonomous Robots*. Springer, 2010, vol. 28, pp. 295–306. 15
- [29] M. Kovač, Wassim-Hraiz, O. Fauria, J.-C. Zufferey, and D. Floreano, “The epfl jumpglider: A hybrid jumping and gliding robot with rigid or folding wings,” in *IEEE International Conference on Robotics and Biomimetics*, 2011. 15
- [30] J. Burdick and P. Fiorini, “Minimalist jumping robots for celestial exploration,” in *The International Journal of Robotics Research*. SAGE, 2003, vol. 22, pp. 653–674. 15
- [31] W. A. Churaman, A. P. Gerratt, and S. Bergbreiter, “First leaps toward jumping microrobots,” in *IEEE/RSJ International Conference on Intelligent Robots and Systems*, 2011. 15
- [32] D. H. Kim, J. H. Lee, I. Kim, S. H. Noh, and S. K. Oho, “Mechanism, control, and visual management of a jumping robot,” in *Mechatronics*. Elsevier, 2008, vol. 18, pp. 591–600. 15, 16
- [33] A. Yamada, M. Watari, H. Mochiyama, and H. Fujimoto, “An asymmetric robotic catapult based on the closed elastica for jumping robot,” in *IEEE International Conference on Robotics and Automation*, 2008. 15, 16

- [34] Y. Sugiyama and S. Hirai, "Crawling and jumping of deformable soft robot," in *IEEE/RSJ International Conference on Intelligent Robots and Systems*, 2004. 15, 16
- [35] R. Niiyama, A. Nagakubo, and Y. Kuniyoshi, "Mowgli: A bipedal jumping and landing robot with an artificial musculoskeletal system mowgli: A bipedal jumping and landing robot with an artificial musculoskeletal system," in *IEEE International Conference on Robotics and Automation*, 2007. 16
- [36] "http://gmwgroup.harvard.edu/research/index.php?page=23," *Whitesides Group Research - Soft robotics*. 16
- [37] S. Kim, C. Laschi, and B. Trimmer, "Soft robotics: a bioinspired evolution in robotics," in *Trends in Biotechnology*. Cell Press, 2013, vol. 31, no. 5, pp. 287–294. 16
- [38] C. Majidi, "Soft robotics: A perspective - current trends and prospects for the future," in *Soft Robotics*, vol. 1, 2013. 16
- [39] R. Pfeifer and G. Gómez, "Morphological computation – connecting brain, body, and environment," in *Lecture Notes in Computer Science*. Springer, 2009, vol. 5436, pp. 66–83. 16
- [40] M. Calisti, M. Giorelli, G. Levy, B. Mazzolai, B. Hochner, C. Laschi, and P. Dario, "An octopus-bioinspired solution to movement and manipulation for soft robots," in *Bioinspiration and Biomimetics*. IOP, 2011, vol. 6. 16, 17
- [41] M. W. Hannan and I. D. Walker, "Kinematics and the implementation of an elephant's trunk manipulator and other continuum style robots," in *Journal of Roboti Systems*. Wiley, 2003, vol. 20, no. 2, pp. 45–63. 16, 17
- [42] K. Suzumori, S. Endo, T. Kanda, N. Kato, and H. Suzuki, "A bending pneumatic rubber actuator realizing soft-bodied manta swimming robot," in *IEEE International Conference on Robotics and Automation*, 2007. 16
- [43] H.-T. Lin, G. G. Leisk, and B. Trimmer, "Goqbot: a caterpillar-inspired soft-bodied rolling robot," in *Bioinspiration and Biomimetics*. IOP, 2011, vol. 6, no. 2. 16, 17
- [44] F. Daerden and D. Lefeber, "Pneumatic artificial muscles: actuators for robotics and automation," *European Journal of Mechanical and Environmental Engineering*, 2002. 16, 17
- [45] B. Verrelst, R. Ham, B. Vanderborght, D. Lefeber, F. Daerden, and M. V. Damme, "Second generation pleated pneumatic artificial muscle and its robotic applications," *Advanced Robotics*, vol. 20, no. 7, pp. 783–805, 2006. 16
- [46] K. Hosoda, Y. Sakaguchi, H. Takayama, and T. Takuma, "Pneumatic-driven jumping robot with anthropomorphic muscular skeleton structure," in *Autonomous Robots*. Springer, 2010, vol. 28, no. 3, pp. 307–316. 16
- [47] I. Gaiser, S. Schulz, A. Kargov, H. Klosek, A. Bierbaum, C. Pylatiuk, R. Oberle, T. Werner, T. Asfour, G. Bretthauer, and R. Dillmann2, "A new anthropomorphic robotic hand," in *IEEE-RAS International Conference on Humanoid Robots*, 2008. 17, 19
- [48] S. Schulz, C. Pylatiuk, and G. Bretthauer, "A new class of flexible fluidic actuators and their applications in medical engineering," in *at - Automatisierungstechnik*. DeGruyter, August 1999, vol. 47, no. 8. 17
- [49] R. Deimel and O. Brock, "A compliant hand based on a novel pneumatic actuator," in *IEEE International Conference on Robotics and Automation*, 2013. 17
- [50] T. Noritsugu, "Pneumatic soft actuator for human assist technology," in *JFPS International Symposium on Fluid Power, Tsukuba*, 2005. 17

- [51] K. P. Law, M. T. Wu, H. C. Wong, K. Chan, and L. Kan, “Soft mobile robot with on-board energy generation and control,” Final Year Design Project, 2014, Hong Kong University of Science and Technology. 17, 19
- [52] R. F. Shepherd, F. Ilievski, W. Choi, S. A. Morin, A. A. Stokes, A. D. Mazzeo, X. Chen, M. Wang, and G. M. Whitesides, “Multigait soft robot,” in *Proceedings of the National Academy of Sciences of the United States of America*, 2011. 17
- [53] R. F. Shepherd, A. A. Stokes, R. M. D. Nunes, and G. M. Whitesides, “Soft machines that are resistant to puncture, and that self seal,” in *Advanced Materials*. Wiley, 2013. 17
- [54] R. Pfeifer and J. Bongard, *How the Body Shapes the Way We Think*. MIT Press, 2006, pp. 77–82. 35
- [55] P. Reiser, “<http://www.warpig.com/paintball/technical/gasses/co2dynamics.shtml>,” *Some CO2 Physics*. 44
- [56] “<http://arduino.cc/en/main/arduinoboardnano>,” *Arduino Nano - Overview and Specifications*. 44
- [57] “<http://www.nxp.com/documents/applicationnote/an10216.pdf>,” *AN10216-01 - I2C Manual*. 47
- [58] *DIN 18065: Stairs in buildings - Terminology, measuring rules, main dimensions*, 2011. 51
- [59] “http://rotations.berkeley.edu/?page_id=1906,” *Integration Drift*. 56
- [60] N. Kojimoto, *Pneumatic battery: A chemical alternative to pneumatic energy storage*. MIT, 2012. 61
- [61] R. Pfeifer and J. Bongard, *How the Body Shapes the Way We Think*. MIT Press, 2006, pp. 34–37, 221–222. 62